MAGNETIC PROPERTIES OF NITROGEN- DOPED CARBON NANOSPHERES

by

Makhosonke Berthwell Dubazane

A dissertation submitted to the Faculty of Science, University of the Witwatersrand, Johannesburg, in fulfillment of the requirements for the degree of Master of Science

Johannesburg

September 2012

DECLARATION

I declare that this dissertation is my own, unaided work. It is being submitted for the Degree of Master of Science in the University of the Witwatersrand, Johannesburg. It has not been submitted before for any degree or examination in any other University.

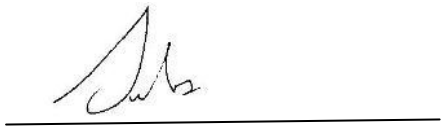

(Signature of candidate)

17th day of September 2012

ABSTRACT

Electron spin resonance (ESR) was used to characterize a suite of carbon nanospheres (CNS) samples with varying nitrogen concentrations at room temperature. The CNS were produced using two different reactors (vertical and horizontal) under different preparatory conditions. Resonance spectra of samples produced from the vertical reactor showed resonance lines- a narrow paramagnetic component, and broader component. They were attributed to nitrogen paramagnetic impurities and carrier spins, respectively. Samples produced in the horizontal reactor revealed stronger line spectra that were narrower and Dysonian in shape. The nitrogen content of the samples produced by the horizontal reactor was determined through ESR analysis which involves integration of the resonance peak, and normalizing to the mass of the sample. The relative g-shift was also measured by using a DPPH reference sample. Room temperature power saturation experiments were performed on samples produced from the horizontal reactor with the aim of estimating the spin relaxation times. Two samples from the horizontal reactor were further investigated at low temperatures (4 K- 320 K) at a constant microwave power. The resonance parameters investigated were linewidth, asymmetry ratio and amplitude, and possible spin-lattice relaxation mechanisms were investigated. The variation of the amplitude with temperature was investigated using two models: (1) a model based on lattice vibrations, and (2) a model based on nanographites assembly (considered interaction between carrier and localized spins). At low temperatures both models have amplitude that changes inversely with temperature in accordance with Curie law. At high temperatures ($T > 200$ K) a model based on nanographites assembly provide an alternative; it describes the rise in the signal amplitude in terms of thermally activated paramagnetic electrons from non-magnetic ground state to excited state at energy $\Delta \cong 0.3$eV. Analysis of linewidth and asymmetry ratio data confirmed that the spin-lattice relaxation governed by thermal activated electrons is a dominant relaxation mechanism at high temperatures.

In memory of my grand-mother

Makhosazane Dubazane

1926-2009

ACKNOWLEDGEMENTS

I would like to thank my supervisor, Dr. J. M. Keartland, for giving me the opportunity to undertake this work, and his advice and persistent support in times of difficulty. I would also like to thank Dr. Z. Chiguvare for his invaluable assistance and advice on matters related to carbon nanomaterials; Dr. D. Wamwangi for being a friend and constantly helpful on issues related to concepts in solid state physics; Prof. N. J. Coville and Ms. N. Kunjuzwa in the School of Chemistry, Wits, for providing carbon nanosphere samples and some data related to synthesis as well as structural characterization. I would also like to express my enormous gratitude to all the members of my family, colleagues and friends for their invaluable support and moral motivation.

Two conference proceedings publications resulted from the work described in this dissertation.

"Characterization of nitrogen-doped nanospheres using electron magnetic resonance" by J. M. Keartland, M. B. Dubazane, V. Marsicano, N. Kunjuzwa and N. J. Coville, Proceedings of SA Institute of Physics 2011, 127-133. Pretoria July 2011, ISBN: 978-1-86888-688-3.

"Magnetic Properties of Carbon Nanospheres at Low Temperatures" by M. B. Dubazane, J. M. Keartland and Y Mishgina, Proceedings of SA Institute of Physics 2011, 168-173. Pretoria July 2011, ISBN: 978-1-86888-688-3.

Table of Contents

LIST OF FIGURES

LIST OF TABLES

LIST OF SYMBOLS

Boltzmann constant:$k_B = 1{,}38062 \times 10^{-23}$ J/K

Electron g-factor: g

Free electron g-factor: $g = g_e = 2{,}0023$

Plank constant: $h = 6{,}62620 \times 10^{-34}$ J. s

$$\hbar = h/2 = 1{,}05459 \times 10^{-34} \text{ J. s}$$

Permeability of free space: $\mu_0 = 4\pi \times 10^{-7}$

Bohr magneton: $9{,}27410 \times 10^{-24}$ J/T

Electron rest mass: $m = 9{,}10956 \times 10^{-31}$ kg

Velocity of light: $c = 2{,}997925 \times 10^{8}$ m/s

Proton charge: $e = 1{,}60219 \times 10^{-19}$ C

Permittivity of free space: $\epsilon_0 = 10^7/4\pi c^2$

Proton rest mass: $M_p = 1{,}67261 \times 10^{-27}$ kg

GLOSSARY OF ABBREVIATIONS

ESR: electron spin resonance

NMR: nuclear magnetic resonance

EMR: electron magnetic resonance

EPR: electron paramagnetic resonance

MWNT: multi-walled carbon nanotubes

CNT: carbon nanotubes

CNS: carbon nanospheres

CNH: carbon nanohorns

ACF: activated carbon fibers

CVRH: coulomb gap variable range hopping

CESR: conduction- electron spin resonance

CHAPTER 1

Introduction

The influence of nitrogen paramagnetic defects on the magnetic properties of the carbon nanospheres (CNS) is studied by electron spin resonance (ESR) method. These defects create an impurity band and the density of states near the Fermi level; the Fermi level is an important physical quantity which is necessary for understanding charge and spin transport mechanisms in strongly localized systems [1]. For samples with low impurity concentration, the electron wave function is localized with a localization radius *b* smaller than the average nearest-neighbor distance *R*, hence electrical conductivity of such a material is governed by variable range hopping(VRH) since the activation energy for a hopping process decreases continuously with temperature [2, 3]. However, if the density of states (DOS) changes with temperature, the electrical conductivity of a material could be limited by Coulomb gap [3, 4]. One would therefore describe the charge transport as Coulomb gap variable range hopping (CVRH).

Overall, the nature of the paramagnetic defects in the carbon-based materials is still far from being clear. In graphitic carbons one could observe the σ- and π-type defects; however Robertson and O'Reilly [5] reported that π-defects are probable due to their lower creation energy. The information related to the nature of electronic states, the mutual interactions between spins and the interaction with a lattice could be achieved through careful analysis of the ESR spectrum in a range of temperature. Apart from the nature of defects, electrical transport could be probed with the ESR technique. Due to the relationship between ESR linewidths and the spin relaxation times, changes in the ESR linewidth with temperature provide a powerful tool to investigate the mobility processes of the unpaired electrons. Motional narrowing or hopping could be manifested through the linewidth decreasing with temperature.

Carbon nanospheres have large potential applications. They can improve magnetic resonance imaging (MRI) contrast; and they can be used to remove toxins or drugs from patients. In chemical industries, carbon nanospheres can be used as catalyst, fillers, rubber additives, lubricating agent owing to properties [6-8]. SnO_2-nanoparticles coated hollow carbon nanospheres are desirable functional nanocomposite in many industrial applications including gas sensors, batteries, and optics [9].

1.1 RESEARCH OUTLINE

The nitrogen- doped carbon nanospheres (CNS) were produced using two different reactors and precursors which served as sources of carbon and nitrogen atoms. The sample synthesis of CNS is discussed in details in Chapter 4 of the dissertation. The electron spin resonance (ESR) is the investigative tool that would be used to characterize the CNS containing different amount nitrogen. Further questions regarding the magnetic properties of the CNS would also be investigated with ESR at low temperatures.

The nitrogen- doped carbon nanospheres (CNS) produced from the vertical reactors exhibited pronounced electron spin resonance (ESR) and negligible conduction electron spin resonance (CESR) spectra [10]. The existence and nature of coupling between nitrogen-induced paramagnetic ions were the main objectives of the research. The coupling of paramagnetic ions could be enhanced by interaction with conduction carriers in accordance with theoretical models [11, 12, 13].

The CNS produced from horizontal reactor were very different; they produced spectra that were narrower and weakly Dysonian in shape, a characteristic of conduction electrons. Hence, the electron spin resonance (ESR) spectra of NK6, NK7, and NK9 could not be obviously considered as just paramagnetic but rather as composite spectra. The spectrum of sample labeled NK7 and NK9 are thought to result from strong overlap between resonant spectrum of nitrogen paramagnetic ions (localized

spins) and conduction carrier spins. The ESR parameters such as asymmetric ratio, amplitude and linewidth would give detailed information regarding charge and spin dynamics in a range of temperature.

The ESR linewidth was the main investigative parameter used to probe for the predicted strong interaction between localized and conducting carrier spins. The asymmetric ratio and amplitude would monitor the changes of conduction carrier density as temperature changes [14, 15]. Hence, they complement linewidth measurements, since they give fraction of conduction carriers which have the potential to strengthen the coupling of paramagnetic ions.

1.2 CHAPTER ORGANIZATION

Chapter 2 has a number of sections; the electronic properties of graphite and nitrogen doped graphite-like materials are described in section 2.1. Literature survey of nitrogen doped carbon nanospheres and evolution of CNS in nitrogen environment is discussed in section 2.2. The nature of magnetism in carbons is further investigated in section 2.3 and 2.4 and discussions focus mainly on carbon nanotubes (CNT), activated carbon fibers (ACF) and carbon nanospheres (CNS).

Chapter 3 is divided into eleven sections. Theoretical description of electron magnetic resonance is described in section 3.1, while a general spin relaxation mechanism is described in section 3.2. Spin relaxation mechanism dominated by carrier electrons coupled to lattice through spin-orbit coupling is explained in section 3.3. Possible spin relaxation mechanisms associated with localized spins or paramagnetic ions which are modulated by lattice vibrations are well represented in section 3.4. Spin coupling between host and guest electron spins is elaborated in section 3.5 for some carbonaceous materials. Section 3.6 gives possible spin relaxation due to coupling between magnetic carbon and nitrogen nuclei ^{13}C and ^{15}N with surrounding electrons. The significance of ESR parameters is discussed in section 3.7, while some implications of these parameters on resonance lineshape are

intensively probed in section 3.8. Theory related to magnetic ordering is generally explored in terms of spin susceptibility in section 3.9. Conditions and requirements associated with the existence of cyclotron or diamagnetic resonance are well elaborated in section 3.10 and 3.11.

Chapter 4 has two sections 4.1 and 4.2. Section 4.1 reports sample preparation and characterization in two subsections. The synthesis of pristine and nitrogen-doped CNS within the vertical and horizontal reactor is reported in subsection 4.1.1 and 4.1.2, respectively. The experimental details which describe the ESR measurements are well presented in section 4.2. The low and room temperature measurements are well-described in subsection 4.2.1 and 4.2.2, respectively.

Chapter 5 presents and discusses experimental results in three main sections 5.1, 5.2, and 5.3. Section 5.1 presents and discusses room temperature measurements in three subsections. Subsection 5.1.1 presents ESR characterization, while 5.1.2 and 5.1.3 present measurements of nitrogen paramagnetic centers and microwave power analysis, respectively. The parameters of the 1^{st} derivative of resonance spectrum investigated at low temperature were amplitude, lineshape, asymmetry ratio and linewidth. Section 5.3 discusses the results in terms of parameters discussed above in subsection 5.2.1, 5.2.2 and 5.2.3 for amplitude, asymmetry ratio and linewidth, respectively. Spin relaxation mechanisms are described in subsection I and II in terms of spin-orbit coupling and lattice vibrations of paramagnetic ions, respectively. This work is concluded and summarized in chapter 6.

References

1. Anderson P. W., *Phys. Rev.* **109**, 1492 (1958).
2. Mott N. F. and Davis E. A., *Electron Processes in Non-Crystalline Materials* (Clarendon Press, Oxford, 1979), 2nd Ed.
3. Shklovskii B. I. and Efros A. L., *Electronic Properties of Doped Semiconductors* (Springer-Verlag, Berlin, New York, 1984).
4. Efros A. L. and Shklovskii B. I., *J. Phys. C* **8**, L49 (1975).
5. Robertson J. and O'Reilly E. P., *Phys. Rev. B* **35**, 2946 (1987).
6. Reddy A. L. M. and Ramaprabhu S., *Nanoscale Res. Lett.* **3**, 2 (2008).
7. Dong Z. P., Yang B., Jin J., Li J., Kang H. W., Zhong X., Li R., Ma J. T., *Nanoscale Res. Lett.* **4**, 335 (2009).
8. Ajayan P. M., *Chem. Rev.* **99**, 1787 (1999).
9. Li M., Wu Q., Ming W., Jianlin S., *Nanoscale Res Lett*. **4**, 11 (2009).
10. Chipara M., Iacomi F., Zaleski J. M., Bai J. B., *Journal of Optoelectronics and Advanced Materials* **8**, 2 (2006).
11. Hasegawa H., *Prog. Theor. Phys. (Kyoto)* **21**, 483 (1959).
12. Owen J., Browne M., Knight W. D. and Kittel, C., *Phys. Rev.* **102**, 1501 (1956)
13. Taylor R. H., *Adv. Phys.* **24**, 681 (1975).
14. Enoki T., Kawatsu N., Shibayama Y., *et al.*, *Polyhedron* **20**, 1311(2001).
15. Beuneu F. and l'Huillier C., *Phys. Rev. B* **59**, 8 (1999).

CHAPTER 2

MAGNETISM IN CARBONS

This chapter is devoted to a discussion of the nature of magnetism and spin dynamics in carbons and carbon nanostructures of different geometrical shapes. In addition, it also discusses general challenges, as well as problems related to nitrogen (N) doping and stability of N paramagnetic defects. Literature related to magnetic properties of different carbon systems is limited; this chapter simply provides a comprehensive review of the literature. The properties of the materials relevant for this research are outlined with reference to a limited number of publications from the literature.

2.1 ELECTRONIC STRUCTURE OF GRAPHITIC CARBONS

Carbon nanospheres (CNS) are graphitic in structure; hence knowledge of the electronic structure of graphite is necessary to fully understand the magnetic properties of these materials. Carbon atom in graphite adopts sp^2 bonding configurations; three of the four valence electrons of carbon are in trigonally directed sp^2 hybrid orbitals (form σ-bonds), while the fourth electron occupies $p\pi$ orbital which lies orthogonal to the σ-bonds plane as shown in Figure 2.1.1. The $p\pi$ orbital forms the weak π-bonding with neighboring $p\pi$ orbitals; this weak π-bonding is called Van der Waals interactions.

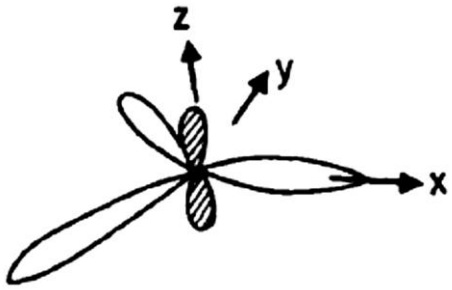

Figure 2.1.1 Schematic representation of sp^2 hybridized carbon.

This bonding anisotropy has an effect of producing high electrical conductivity and strength along basal plane of graphite but lower values along c-axis shown as z-axis in Figure 2.1.1. Nitrogen-doped CNS results from an ensemble of nanometer-sized graphitic clusters with poor packing along the c-axis and larger inter-planar spacing in comparison to pristine graphite. Since graphitic cluster dimensions determine the π-states and therefore the optical band gap; any local structure or graphitic cluster which gives an odd number of π-states produces a state (localized state) near the Fermi level which is half-filled; this localized state is commonly known as paramagnetic center.

The possibility of observing any σ-type paramagnetic defects is ruled out by the lower creation energy of π-defects. The typical nitrogen paramagnetic defect ($N\pi^*$) is shown in Figure 2.1.2 for nitrogen ($N_{3\pi}$) substitutionally embedded on the graphitic lattice. This is one of the few N configurations resulting in paramagnetic defects. Although, nitrogen can occupy substitutional sites in graphitic lattice, other N bonding configurations such as pyrrolic-like and pyridinic-like local structures (as shown in Figure 2.1.2) are not paramagnetic as their π_z^* and π_z -states are empty and paired, respectively.

Pristine graphite can be hardly considered paramagnetic although its π-bonding state is half-filled; electrons occupy extended states which are farther away from the Fermi level and can conduct electricity even at 0 K in comparison to electrons in localized states. Throughout this project the interaction between the paramagnetic electrons in extended (or band tail) and localized states are investigated in details, and they are referred to as carriers (conduction) and localized electrons, respectively. The stability of nitrogen paramagnetic defects is discussed in the following sections for different graphitic carbons.

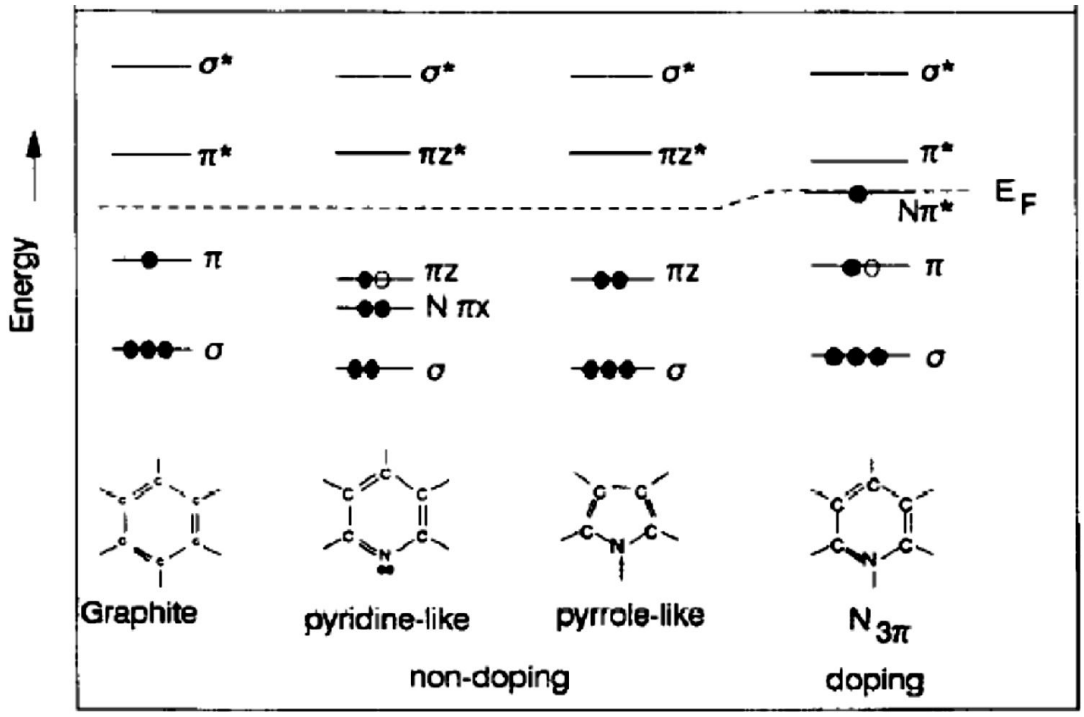

Figure 2.1.2 A schematic showing typical nitrogen induced local structures and corresponding electronic configurations. The dashed horizontal line (Fermi-level) on the top-half of the figure separates the bonding (lower half) and anti-bonding orbitals [1].

2.2 NITROGEN DOPED CARBON NANOSPHERES

Unlike in most materials whereby doping mainly influences electronic and magnetic properties; N doping of carbonaceous materials can also enhance surface properties such as basicity, polarity and heterogeneity in terms of hydrophilic sites. Moreover nitrogen functionalities strongly influence catalytic activities of carbonaceous materials [2, 3].

Uniformly sized carbon nanospheres (CNS) have been produced in large quantities via pyrolysis of different precursors and in the presence of nitrogen [4, 5, 6] as shown in Figure 2.1.1. Nieto-Marquez *et al.* [5], produced both pristine and doped CNS

using the benzene and other N containing precursors (aniline and nitrobenzene), respectively.

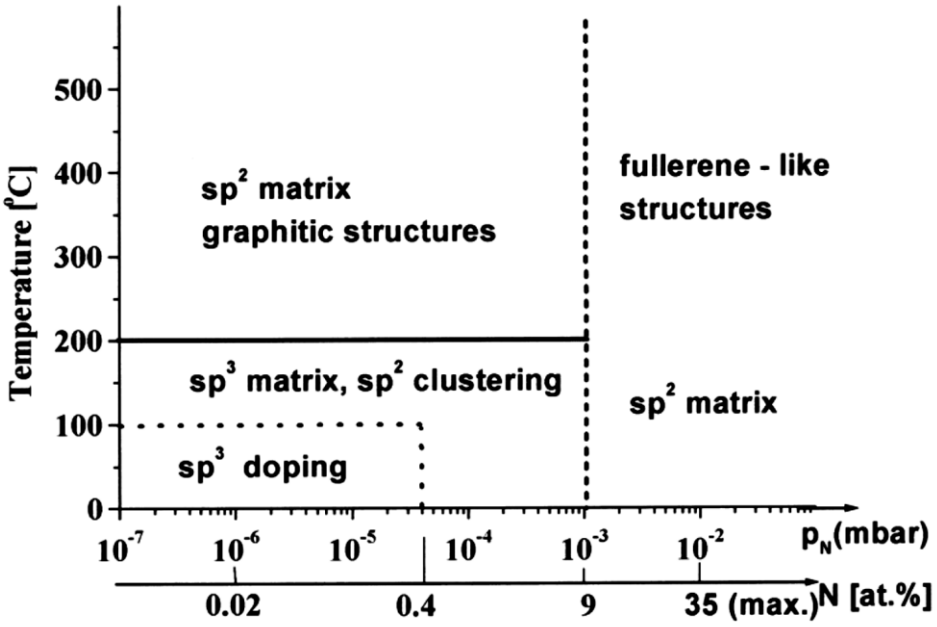

Figure 2.2.1 A schematic showing phase diagram leading to evolution of carbon nanospheres in nitrogen atmosphere [4].

XRD patterns and Raman spectrum revealed that the produced spheres comprise of small and disordered graphite crystallites. Through TEM analyses the temporal evolution of carbon spheres was shown to be controlled by nitrogen content and type of precursor being used [7, 9]. Temporal evolution has been reported elsewhere to result from unstable pentagons, hexagons, heptagons or reactive dangling bonds evolving through bond switching and migration process to form more stable structure with spherical morphology [8, 9, 10, 11].

2.3 MAGNETIC CARBON NANOSPHERES

Pristine carbon nanospheres of about 50 nm in diameter were synthesized in nitrogen atmospheres by Calderon-Moreno *et al.* [6]. The structural features of CNS investigated with synchrotron radiation X-ray diffraction (SR-XRD) revealed that the spheres were composed of small graphitic domains or clusters of width about 2 nm. The magnetic measurements with SQUID magnetometer in the range of temperature and magnetic field revealed that the spheres were paramagnetic at low temperatures ($\chi = 3.7 \times 10^{-6}$ emu/g at 2 K) and there is also a transition to orbital diamagnetism ($\chi = -4.1 \times 10^{-7}$ emu/g at room temperature) as temperature increases. At low magnetic fields, the relationship between magnetization and applied magnetic field was linear at almost all temperature investigated, confirming the presence of localized spins attributed to zigzag non-bonding π-states of nanographites comprising the CNS.

Carbon nanospheres prepared as Pb-C nanocomposites [12] showed more structural phases and notable magnetic properties. These Pb-C composites are carbon nanosphere shells encapsulating Pb nanoparticles. These carbon nanospheres had different degree of graphitization. The magnetization measurements in the range of temperature and magnetic field shows that highly oriented pyrolytic graphite (HOPG) spheres are ferromagnetic while the disordered ones are diamagnetic. The ferromagnetic carbon substance was not separated; the ferromagnetic phase is typically present in the form of inclusions in non-magnetic matrix. The ferromagnetism of HOPG spheres was attributed to mixture of sp^3 and sp^2 C resulting from ferromagnetic interaction of localized magnetic moments separated by sp^3 centers [13, 14, 15].

Nevertheless, this speculation is not quite true; ion irradiated HOPG is ferromagnetic [16] up to room temperature. In addition, some pyrolytic carbon materials prepared from triethylamine contain a mixture of sp^2 and sp^3 bonds and they are non-magnetic; more interestingly, the pyrolysis temperature seems to influence the magnetic properties of carbonaceous materials [17].

Ferromagnetism was also observed in CNS encapsulating silver (Ag) nanoparticles and they have diameter of about 10 nm- 40 nm [18]. In contrast to any other CNS, graphitic shells encapsulating Ag cores are closed or continuous; for that reason, the non-bonding zigzag edge-inherited states are not considered. The nature of ferromagnetism is attributed to spin polarization of the α-sites forming metallic 1D C-C chain along *c*-axis (see Figure 2.2.1). The localized spins (in sp^1 orbitals) perpendicular to the closed graphene layers were considered to result from large curvature of graphene and their strong stability is due to poor in-plane π-bonding.

The magnetic interactions between localized spin at β-sites is mediated by spin-polarized α-band, and hence these β spins coupled ferromagnetically. The magnetic transition, ferromagnetic-diamagnetic, at high temperatures and/or after pressing the samples confirms the co-existence of localized and conduction (carrier) electrons.

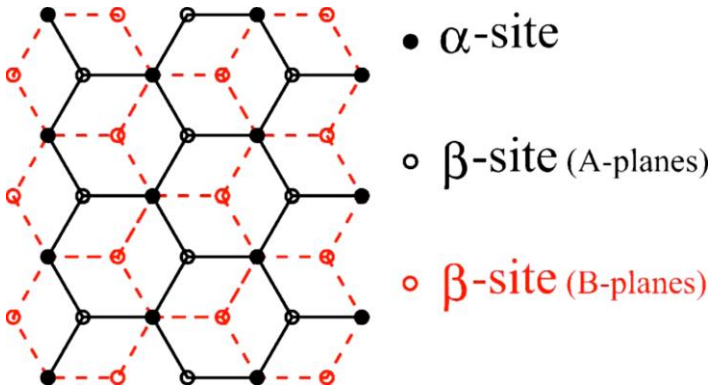

Figure 2.3.1 Schematic showing different C positions in graphite layers (A and B) having ABAB… stacking [18].

This is also in agreement with weak ferromagnetism of the CNS grown by CVD process using Kaolin supported transition metal Ni as catalyst [10]. Hysteresis curves were produced up to room temperature; total magnetic susceptibility measured was weakly dependent on temperature and was attributed to average contribution of conduction and localized electron spins with Pauli and Curie susceptibility of order 10^{-8} and 10^{-4}, respectively. Moreover, the presence of conduction electrons at room

temperatures was confirmed by Dysonian line shape of carbon nanospheres, shown in Figure 2.2.2.

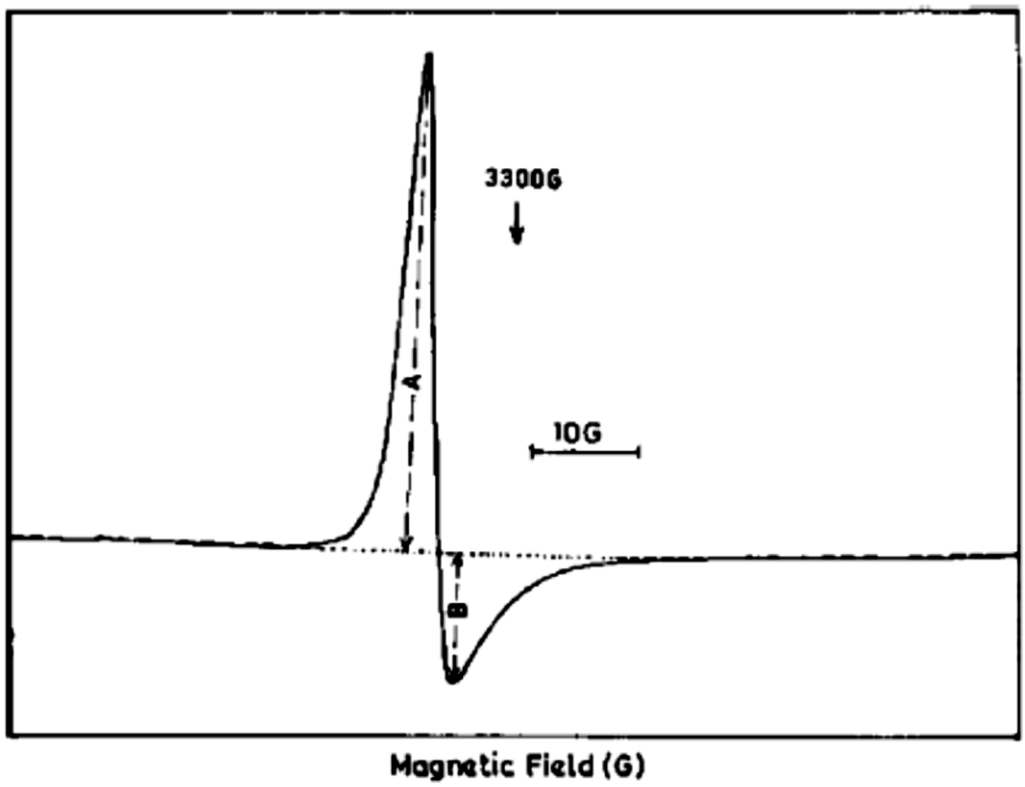

Figure 2.3.2 A room temperature resonance line of carbon nanospheres produced by Miao *et al.*[10].

Romanenko *et al.* [19] investigated the CNS, synthesized through annealing of nanodiamond particles, using resistance and magneto-resistance measurements. The resistivity measurements showed strong electron localization as manifested by VRH fit in range of temperature investigated,

$$\rho(T) = \rho_0 \exp(C/k_B T)^{1/n} \qquad (2.2.1)$$

where *n* can vary between 2 and 4 depending on the dimensionality of carrier motion and on the significance of Coulomb gap.

The large extrinsic carriers in these CNS samples (8×10^{21} cm^{-3} and 3×10^{21} cm^{-3}) are associated with defects in graphitic layers [20- 26] and these defects reduce the mean free path.

2.4 NATURE OF MAGNETISM IN CARBONS

Crystalline carbons (diamond, graphite, carbon nanotubes, and fullerenes) have been known to be diamagnetic [27] for a very long time since they are lacking the *3d* and *4f* shells. The *3d* and *4f* shells are incompletely filled in ferro-magnetic materials such as iron, manganese, and rare-earth metals.

The origin of ferromagnetism in carbon structures has resulted in some debates, and the presence and nature of defects seem to give clear logical explanations. Defects can be brought about by physical means such as particle irradiation onto pristine carbon structures [16]. Most models describe intrinsic magnetism in carbon systems in terms of under-coordinated atoms (defects) due to impurities and/or boundaries [28, 29] and special topology [30]. The presence of defects may results in quasi-localized states near the Fermi level and therefore defects can control the magnetic properties. Since magnetic metals such as cobalt or iron that are frequently used as catalysts are often experimentally excluded or of negligible concentrations, hence any magnetic properties observed were attributed to carbon.

Although carbon structures can have different geometrical shapes (carbon nanotubes, carbon nanohorns, carbon nanospheres, etc.), they are all probably made-up of nanographene layers called nanographites, hence the words nanographene and nanographite are used interchangeably in this context.

2.4.1 Magnetism in carbon nanotubes

2.4.1.1 Vacancies

As mentioned earlier, magnetism in carbon is closely associated with defects; hence defects in carbon structures can be deliberately introduced to enhance magnetism. The most challenging problems relate to conditions necessary to achieve stable magnetic defects.

Among defects, vacancies are simple defect-type resulting from missing atom or ion in a lattice, and can be either Schottky or Frenkel-type depending on whether a lattice atom (or charged atom) migrates into surface of a crystal or into interstitial position, respectively. Creation of vacancies in carbon nanotubes can either give unfavorable or beneficial effects, for instance, the presence of vacancies may enhance magnetic properties while compromising some mechanical strength.

The nature and stability of vacancies in CNT, single-walled carbon nanotubes (SWNTs) irradiated with angstrom-diameter electron beam have been investigated by Rotriguez-Manzo *et al.* [31]. The relaxation or shrinkage of the surface of carbon nanotubes was observed around the irradiated spot and no vacancy was observed. The absence of vacancies in SWNT was attributed to high mobility of single vacancies which might have been created (single vacancy is stable and leaves dangling bonds) and coalesce with other single vacancies to form unstable di-vacancy[32], which relaxes rapidly and thus enhancing lattice reconstruction through formation of non-hexagonal rings[33, 34]. This is in agreement with both theoretical [33-37], and experimental [38- 44] investigations which reported high instability of vacancies in CNTs which result in lattice reconstruction through formation of hexagonal and non-hexagonal rings.

In contrast to the SWNT, some vacancies were observed in the multi-walled carbon nanotubes (CNT) and double-walled carbon nanotubes (DWNTs) at lower temperatures [30]. However, at temperature about 480 ^{0}C and above the highly

mobile single vacancies (migration barrier of 1.4 eV) coalesce into unstable di-vacancies causing the lattice of DWNT to reconstructs resulting in shrinkage of their surface [32]. Previous work regarding electron irradiation on graphitic carbons reported that, about 300 ^{0}C and above, carbon structures remain intact [39]. This behavior was attributed to high mobility of possible defects and interstitials at higher temperatures leading to formation of very unstable defects which relax and thus causing lattice re-construction.

2.4.1.2 Graphitic-like carbons and carbon nanotubes

Among theoretical models explaining the origin of magnetism in carbons in terms of under-coordinated atoms (defects) or special topology of carbon atomic network, the inclusion of light metals which are by themselves non-magnetic cannot be ignored.

As with inclusion of hydrogen in graphite, fullerenes and CNT [17, 45, 46, 47, 48, 49]; incorporation of nitrogen in π-conjugated systems strongly influences magnetic properties of carbons [50]. Nitrogen (N) incorporated in substitutional sites shows a potential to control the electronic properties of carbon nanotubes [51-61]. Since N has one more electron compared to C, one might expect N to provide an extra electron into the lattice, thus enhancing electrical conductivity of carbon structure. Several and useful methods for incorporating N are substitution reaction [69], arc-discharge-technique [52, 62] and particle irradiation [63]. One may want to know the best technique to incorporate N in carbon structures; and best techniques strongly depend on the degree of mobility of magnetic defects and formation of intercalated nitrogen between graphitic layers.

2.4.1.3 Substitutional and adatom Nitrogen in CNTs.

Nitrogen substitutionally embedded in graphitic lattice has the most stable configuration, while three of N electrons form sp^2 bonds, the remaining two electrons participate in π-electron system of carbon. However N incorporated in sp^2 configurations probably results in non-magnetic carbon systems; pyrrolic and pyridinic N are non-magnetic. However, there is also a probability of nitrogen being adsorbed on surface of CNT [64] or intercalated between graphene layers in the form of N molecules [60] or binding two irregular sp^3 carbons [52]. The presence of N intercalated between CNT layers may help form cross-links between nearby graphene layers [59] or form interlayer bonding depending on the extent of separation between the layers as well as the local stacking type. N adatom forms a bridge-like structure on the graphene surface where two carbon atoms become sp^3 hybridized and the structure has non-zero magnetic moment of about 0.57 μ_B [65]. N adatom also form a bridge-like structure about the surface of CNT [64].

However, it is important to note that different orientations of N result in inequivalent C-C bonds and thus different magnetic strength. This difference in the effectiveness of N adatoms comes from different possible orientations of C-N-C plane relative to CNT axis; parallel orientation gives large magnetic moment compared to perpendicular one [65]. The magnetic moments in both graphene and CNT mainly originate from N adatom p-orbital perpendicular to C-N-C plane [65].

According to Ma *et al.* [49], the magnitude of magnetic moment is mainly controlled by coupling between surface π-orbitals and adatom p-orbitals. For instance, N adatom in C-N-C plane perpendicular to tube axis breaks C-C bonds in their plane, hence strong coupling between surface π-orbital of C system with p-orbital weakens the net magnetic moment.

2.4.2 Nanographite and its assembly

Graphitic clusters of arbitrary shapes and size are known as nanographites; they represent a new class of mesoscopic system intermediate between aromatic molecules and extended graphite sheets. Some carbon nanostructured materials such as activated carbon fibers (ACF), carbon nanospheres (CNS), carbon nanohorns (CNH) are made from the assemblage of nanographite fragments. ACF and CNH [67] represent a good model of nanographites assemblage system. This section serves to compare previous results regarding the magnetism and spin dynamics in ACF [67], CNH [66], and disordered network of nanographites [67]. Enoki *et al.* [67], found few nanographene sheets stacked in three dimensional (3D) random networks of nanographites with in-plane dimension of about 2-3 nm. Through electrical conductivity measurements from the as-synthesized and low heated treated, ACF are insulating at low temperatures due to strong Coulomb-gap type electron localization. Their electrical conductivity follows the relation,

$$\sigma(T) = \sigma_0 \exp\left[-(T_0/T)^{1/2}\right] \qquad (2.3.1)$$

where $T_0 = 3e^2/2\pi^2 k_B \varepsilon \alpha^{-1}$ is the characteristic temperature expressed in terms of dielectric constant ε of a material surrounding a metallic nanographite cluster and localization length α^{-1} of electronic wavefunctions. Conduction electrons confined within a cluster are thermally activated to hop between metallic nanographite clusters; this is known as Coulomb-gap variable range hopping (CVRH). At higher temperatures, the enhancement of the measured electrical conductivities was attributed to fast hopping process which probably promotes the motional narrowing of non-bonding zigzag edge state spins.

Enhancement of electrical conductivity was accompanied by negative shift in magnetic susceptibility with increasing heat treatment in ACF; this was due to reduction of inter-nanographite distance or stretching of electron wavefunction within each nanographene leading to a wavefunction overlap and coherent motion of electrons between metallic nanographite clusters [67]. The presence of magnetic

susceptibilities which obey Curie-Weiss law temperature dependence at low temperatures and negative shift of magnetic susceptibility with increasing temperature for all heat treated ACF explain the importance of both non-bonding edge inherited π-electrons and itinerant electrons in magnetic properties of ACF.

The anomalous peak seen near insulator-metallic transition on the magnetic susceptibility and ESR measurements suggests a competition between disordered magnet-like system and anti-ferromagnetic ordering of localized spins at low temperatures, and hence a deviation from a spin-glass state[68]. The appearance of spin-glass state could be closely associated to this infinite coherent electron conduction path network of the assembly of nanographites comprises ACF. The abnormal peak was also seen on the 3D disordered network of nanographenes [69], and was attributed spin-glass phase, and its occurrence was described in terms of inhomogeneous inter-cluster interactions whereby individual nanographene have different ferromagnetic ordering.

Heat treatment enhances inter-cluster coherent electron conduction path network, thus enhance the kinetic exchange interaction between localized electrons mediated by percolating conductive π-electrons, spin bottleneck. The exchange interaction between localized spins is considered long-range, naturally considered to be in the range of 2-3 nm since this interaction is extended over inter-cluster distance whose width are in the range of 2-3 nm [69].

The CVRH conductivity and Curie-Weiss-like temperature dependency of susceptibility at low temperatures suggest strong localization of itinerant electrons within weakly interacting metallic nanographites. Indeed, the ESR lines and intensity power saturation measurements on disordered network of nanographenes yielded a homogeneous and inhomogeneous spin system of the whole network at high and low temperatures, respectively [69].

References

1. Robertson J., *Prog. Solid St. Chem.* **21**, 199 (1991).
2. Shukla A. K., Ravikumar M. K., Roy A., *et al., J. Electrochem. Soc.* **141**, 517 (1994).
3. Roy S. C., Christensen P. A., Hamnett A., Thomas K. M., and Trapp V., *J. Electrochem. Soc.* **143**, 3073 (1996).
4. Kleinsorge B., Ferrari A. C., Robertson J., Milne W. I., Waidmann S., and Hearne S., *Diamond and Related Materials* **9**, 643 (2000).
5. Nieto-Márquez A., Espartero I., Lazo J. C., Romero A., and Valverde J. L., *Chemical Engineering Journal* **153**, 211 (2009).
6. Calderon-Moreno J. M.; Labarta A., Pradell T., Crespo D., and Binh V. T., *Chem. Phys. Lett.* **447**, 295 (2007).
7. Mandumpal J., Gemming S., and Seifert G., *Chem. Phys. Lett.* **447**, 115 (2007).
8. Kudashov A. G., Okotrub A. V., Bulusheva L. G., *et al., J. Phys. Chem. B* **108**, 26 (2004).
9. Renouard T., Gherghel L., Wachtler M., Bonino F., Scrosati B., Nuffer R., Mathis C., and Müllen K., *J. Power Sources* **139**, 242 (2005).
10. Miao J. -Y., Hwang D. W., Narasimhulu K. V., Lin P. -I., Chen Y. -T., Lin, S. -H., and Hwang, L. -P., *Diamond Rel. Mater*.**42**, 4 (2003).
11. Xu Z. X., Lin J. D., Roy V. A. L., Ou Y., and Liao D. W., *Mater. Sci. Eng. B* **123**, 2 (2005).
12. Li D., Han Z., Wu B., Geng D., and Zhang Z., *J. Phys. D*: *Appl. Phys.* **41**, 115005 (2008).
13. Murata K., Ueda H., and Kawaguchi K., *Synth. Met*. **44**, 357 (1991).
14. Murata K., Ushijima H., Ueda H., and Kawaguchi K., *J. Chem. Soc. Chem. Commun*. **18**, 1265 (1991).
15. Ovchinnikov A. A. and Spector V. N., *Synth. Met.* **27**, 615 (1988).

16. Esquinazi P., Spemann D., Höhne R., Setzer A., Han K. -H, and Butz T., *Phys. Rev. Lett.* **91**, 22 (2003).
17. Caudillo R., Gao X., Escudero R., Jose-Yacaman M., and Goodenough J. B., *Phys. Rev. B* **74**, 214418 (2006).
18. Romanenko A. I., Anikeeva1 O. B., Okotrub A. V., *et al*., *Physics of the Solid State* **44**, 3 (2002).
19. Kotosonov A. S., *JETP Lett*. **43**, 37 (1986).
20. Kotosonov A. S., *Sov. Phys. JETP* **66**, 1068 (1987).
21. Kotosonov A. S., *Sov. Phys. Solid State* **33**, 1477 (1991).
22. Kotosonov A. S. and Kuvshinnikov S. V., *Phys. Lett. A* **230**, 377 (1997).
23. Kotosonov A. S. and Shilo D. V., *Carbon* **36**, 1649 (1998).
24. Kotosonov A. S., *JETP Lett.* **70**, 476 (1999).
25. Kotosonov A. S. and Atrazhev V. V., *JETP Lett*. **72**, 53 (2000).
26. Heremans J., Olk C. H., and Morelli D. T., *Phys. Rev. B* **49**, 15122 (1994).
27. Yazyev O. V., and Helm L., *Phys. Rev. B* **75**, 125408 (2007).
28. Son Y. W., Cohen M. L., and Louie S. G., *Nature* **444**, 7117 (2006).
29. Park N., Yoon M., Berber S., Ihm J., Osawa E., and Tománek D., *Phys. Rev. Lett*. **91**, 237204 (2003).
30. Rodriguez-Manzo J. A. and Banhart F., *Nano Lett.* **9**, 6 (2009).
31. Krasheninnikov A. V., Lehtinen P. O., Foster A. S., and Nieminen R. M., *Chem. Phys. Lett*. **418**, 132 (2006).
32. Krasheninnikov A. V., Nordlund K., and Keinonen J., *Phys. Rev*. B **65**, 165423 (2002).
33. Kotakoski J., Krasheninnikov A. V., and Nordlund K., *Phys. Rev. B* **74**, 245420 (2006).
34. Krasheninnikov A. V., Banhart F., Li J. X., Foster A. S., Nieminen R. M., *Phys. Rev. B* **72**, 125428 (2005).
35. Lee G. -D., Wang C. Z., Yoon E., Hwang N. -M., Kim D. -Y. and Ho, K. M., *Phys. Rev. Lett.* **95**, 205501 (2005).

36. Lee G. -D., Wang C. -Z., Yu J., Yoon E., Hwang N. -M. and Ho K. -M., *Phys. Rev. B* **76**, 165413 (2007).
37. Ajayan P. M., Ravikumar V., and Charlier J. C., *Phys. Rev. Lett*. **81**, 1437 (1998).
38. Banhart F., *Rep. Prog. Phys*. **62**, 1181 (1999).
39. Smith B. W. and Luzzi D. W., *J. Appl. Phys.* **90**, 3509 (2001).
40. Li J. X., Banhart F., *Nano Lett.* **4**, 1143 (2004).
41. Banhart F., Li J. X., Krasheninnikov A. V., *Phys. Rev. B* **71**, 241408 (2005).
42. Yuzvinsky T. D., Mickelson W., Aloni S., Begtrup G. E., Kis A., Zettl A., *Nano Lett*. **6**, 2718 (2006).
43. Zobelli A., Gloter A., Ewels C. P., Colliex C., *Phys. Rev. B* **77**, 045410 (2008).
44. Han K. H., Spemann D., Esquinazi P., Höhne R., Riede V., and Butz T., *Adv. Mater. Weinheim, Ger*. **15**, 1719 (2003).
45. Lehtinen P. O., Foster A. S., Ma Y., Krasheninnikov A. V., and Nieminen R. M., *Phys. Rev. Lett*. **93**, 187202 (2004).
46. Duplock E. J., Scheffler M., and Lindan P. J. D., *Phys. Rev. Lett.* **92**, 225502 (2004).
47. Chan J. A., Montanari B., Gale J. D., Bennington S. M., Taylor J. W., and Harrison N. M., *Phys. Rev. B* **70**, 041403 R (2004).
48. Ma Y., Lehtinen P. O., Foster A. S., and Nieminen R. M., *Phys. Rev.* B **72**, 085451 (2005).
49. Hagiri I., Takahashi N., and Takeda K., *J. Phys. Chem*. A **108**, 2290 (1994).
50. Nevidomskyy A. H., Csányi G., and Payne M. C., *Phys. Rev. Lett*.**91**, 105502 (2003).
51. Droppa Jr. R., Ribeiro C. T. M., Zanatta A. R., dos Santos M. C.; and Alvarez F., *Phys. Rev*. B **69**, 045405 (2004).
52. Jang J. W., Lee C.E., Lyu S. C., Lee T. J., and Lee C. J., *Appl. Phys. Lett*. **84**, 2877 (2004).
53. Che R. C., Peng L. M., and Wang M. S., *Appl. Phys. Lett*. **85**, 4753 (2004).

54. Miyamoto Y., Cohen M. L., and Louie S. G., *Solid State Commun*. **102**, 605 (1997).
55. Czerw R., Terrones M., Charlier J. C.; *et al*., *Nano Lett.* **1**, 9 (2001).
56. Terrones M., Ajayan P. M., Banhart F., *et al.*, *Applied Physics A- Material Science and Processing* **74**, 3 (2002).
57. Srivastava D., Menon M., Daraio C., *et al., Phys*. *Rev. B* **69**, 153414 (2004).
58. Chan J. A., Montanari B., Gale J. D., Bennington S. M., Taylor J. W., and Harrison N. M., *Phys. Rev. B* **70**, 041403 R (2004).
59. Choi H. C., Bae S. Y., Park J., *et al.*, *Appl. Phys. Lett.* **85**, 5742 (2004).
60. Kang H. S. and Jeong S., *Phys. Rev.* B **70**, 233411 (2004).
61. Glerup M., Steinmetz J., Samaille D., *et al.*, *Chem. Phys. Lett*. **387**, 193(2004).
62. Kotakoski J., Krasheninnikov A. V., Ma Y., Foster A.S., Nordlund K., and Nieminen R. M, *Phys. Rev.* B **71**, 205408 (2005).
63. Zhao M. W., Xia Y. Y., Ma Y. C., *et al.*, *Phys. Rev. B* **66**, 155403 (2002).
64. Ma Y., Foster A. S., Krasheninnikov A.V., and Nieminen R. M., *Phys. Rev.* B **72**, 205416 (2005).
65. Garaj S., Thien-Nga L., Gaal R., *et al.*, *Phys. Rev. B* **62**, 24 (2000).
66. Enoki T., Kawatsu N., Shibayama Y., *et al.*, *Polyhedron* **20**, 1311(2001).
67. Joseph Joly V. L., Takahara K., Takai K., Sugihara K., and Enoki T., *Phys. Rev. B* **81**, 115408 (2010).
68. Shibayama Y., Sato H., Enoki T., and Endo M., *Phys. Rev. Lett.* **84**, 1744 (2000).
69. Fung A. W. P., Wang Z. H., Dresselhaus M. S., Dresselhaus G., Pekala R. W. Endo M., *Phys. Rev. B* **49**, 17325 (1994).

CHAPTER 3

THEORY OF ELECTRON SPIN RESONANCE

Since the discovery of electron spin resonance (ESR) by Zavoisky in 1944 it has become a widespread non-contact characterization method used in numerous field of science such medicine, chemistry and physics. Physicists often use ESR to investigate magnetic interactions or spin-transport of any unpaired electron spins, for which it was used in this research. This chapter presents the basic and pertinent magnetic resonance theory.

3.1 MAGNETIC RESONANCE CONDITIONS

ESR also known as electron paramagnetic resonance (EPR) is a spectroscopic tool to study materials containing unpaired electrons (paramagnetic ions or free radicals). It is based on the fact that some atoms possess permanent magnetic moments, and an electron is assumed free, through quantum theory treatment, generates a circulating current which in turn induces the magnetic moment,

$$\boldsymbol{\mu} = -g\mu_B \boldsymbol{s} \qquad (3.1.1)$$

where g, $\boldsymbol{s}$ and μ_B represent g-factor, intrinsic spin and Bohr magneton, respectively.

If static magnetic field B is along the z-axis, an induce magnetic moment has a component along the z-axis and one can described the corresponding energies associated with magnetic moment parallel and anti-parallel to static magnetic field as E_- and E_+, respectively,

$$E_{\pm} = \pm\frac{1}{2} g\mu_B B \qquad (3.1.2)$$

This equation describes the well-known Zeeman effect, where the static field lifts the spin degeneracy, and the spin levels are separated in energy ΔE,

$$\Delta E = E_+ - E_- = g\mu_B B \qquad (3.1.3)$$

where μ_B is the Bohr magneton and g is the g-shift and it described local chemical environments.

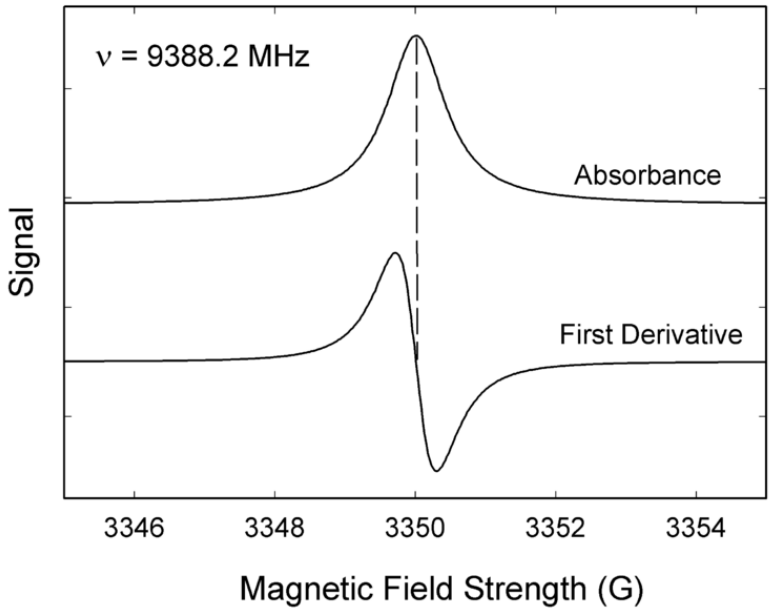

Figure 3.1.1 An ESR spectrometer displays the first derivative of the resonance absorption signal.

If electromagnetic field of energy $\hbar\omega$ is absorbed by a spin system, a transition will occur between two spin states shown in Figure 3.1.2(b). Likewise an electron would undergo resonance if the irradiated energy reaches the separation energy between spin energy levels ΔE,

$$g\mu_B B = \hbar\omega \qquad (3.1.4)$$

where $\omega = \omega_0 = \gamma B$ is the transition frequency, and the equilibrium magnetization could be expressed in the following way, $\boldsymbol{M} = \chi \boldsymbol{B}/\mu_0$ and magnetization is a function of static magnetic susceptibility χ.

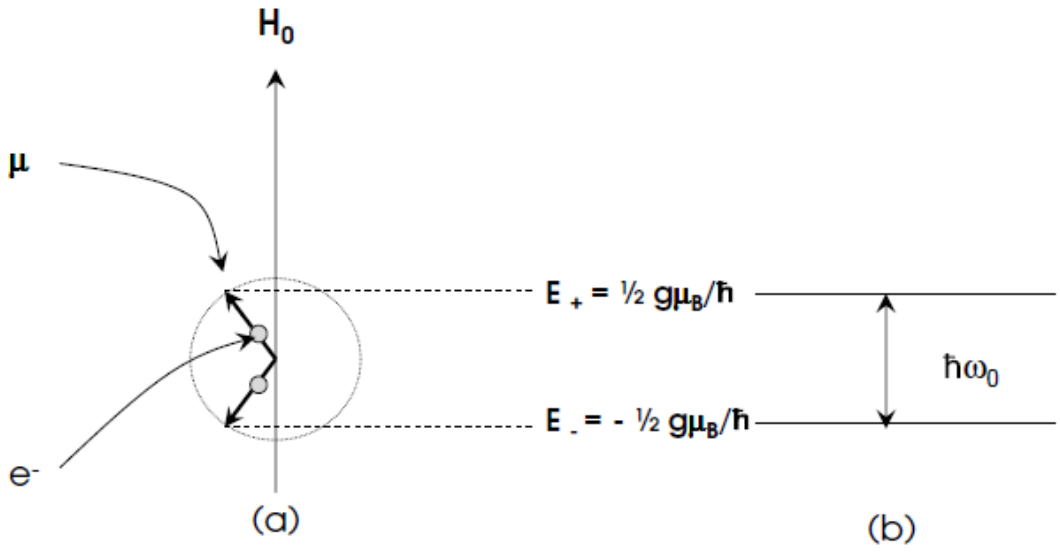

Figure 3.1.2 In the presence of static magnetic field H_0, there exist two spin states of different energies (a), and under radiation with time varying magnetic field it can undergo transition, either spin up or spin down (b).

ESR spectra are often displayed as first derivative of absorption spectrum as shown in Figure 3.1.1 as spectrometer use phase sensitive detection technique. The discussion undertaken above assumes a single free electron under static magnetic field, and one may now consider a macroscopic sample consisting of statistical ensemble of magnetic moments. Boltzmann distribution should be used in describing the relative population of two spin levels shown in Figure 3.1.2,

$$\frac{N_+}{N_-} = exp\left(-\frac{\Delta E}{k_B T}\right) \qquad (3.1.5)$$

where k_B is the Boltzmann constant and T is the absolute temperature. When there is a population difference $N_+ \neq N_-$ the spin system can absorb electromagnetic energy, since the upward and downward transition (shown in Figure 3.1.2) occurs with the same probability.

3.2 GENERAL DESCRIPTION OF SPIN RELAXATION MECHANISMS

Consider a paramagnetic material with non-homogeneous spin system in a static magnetic field *B*, and embedded in thermal bath or lattice as shown in Figure 3.2.1. In many cases the spin system consists of both an electronic and nuclear spin system.

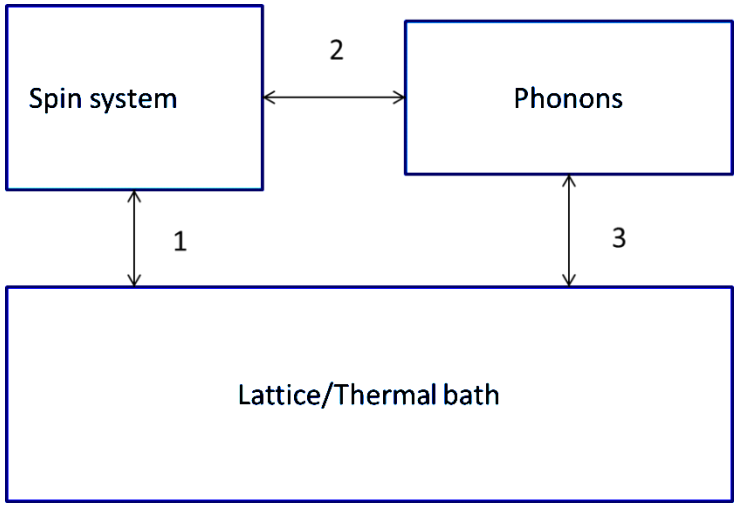

Figure 3.2.1 A schematic showing the common electron spin relaxation mechanism.

Since our interest is on electron spin resonance (ESR), the discussions should be based on excited electron spin relaxation mechanisms through interaction with other electronic spins (exchange coupling or cross-relaxation); spin-phonon scattering and electron-nuclear spin interaction (Hyperfine coupling).

Consider a situation where homogeneous electronic spin systems would have been isolated from surroundings (lattice and nuclear spins); a spin system would be in equilibrium provided the rate at which these identical spins absorbed microwave is lower than rate at which they exchange energy among themselves. This is usually given by $1/T_2$ where T_2 is the spin-spin relaxation time.

However if an electronic spin system couples to nuclear spin system, electronic spins would lose some of their magnetic energies to nuclear spin system (at a cross-relaxation rate $1/T_2^{en}$); a spin system would reach a new equilibrium at infinite temperature since they are shielded from environment.

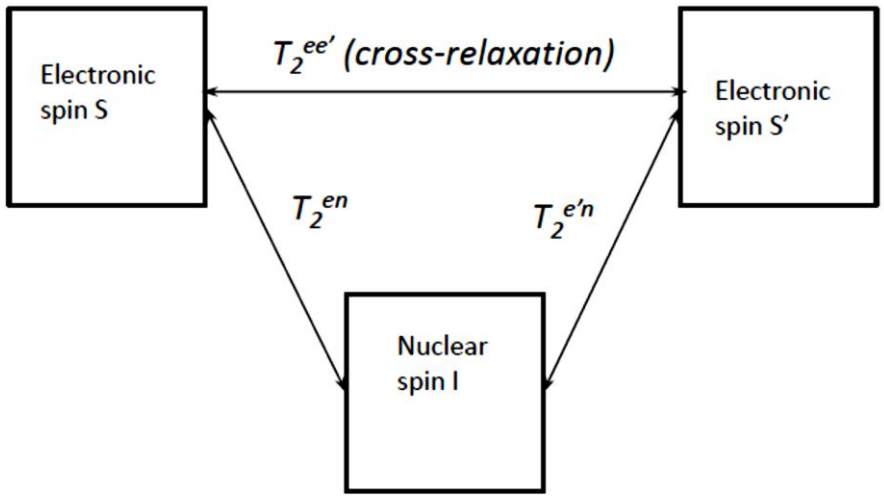

Figure 3.2.2 A schematic showing relaxations involving different spin systems; different electronic spins labeled S and S', and nuclear spins I of the same kind.

Likewise, different electronic spin systems represented as S and S' in Figure 3.2.2 could undergo relaxation via cross-relaxation or exchange coupling between the different spin species. Electronic spin system with higher magnetic energy would have lost their energy into other electronic spin system lower in energy, at a cross-relaxation time $T_2^{ee'}$ till both systems reach a new equilibrium.

A schematic of homogeneous spin system above (Figure 3.2.2) assumes relaxation mechanisms which conserve energy; isolated spin are not feasible, hence spin system that has contact with a lattice lose their energy at a rate $1/T_1^i$(where T_1^i is the spin-lattice relaxation time involving *i* electronic spin systems).

3.2.1 Bloch equations

The longitudinal relaxation time T_1 and dephasing (transverse) time T_2 of carrier spin systems in applied magnetic field

$$\boldsymbol{B}(t) = \boldsymbol{B_0} + \boldsymbol{B_1}(t) \qquad (3.2.1.1)$$

is described by Bloch equations, where $\boldsymbol{B_0}$ and $\boldsymbol{B_1(t)}$ is the uniform and fluctuating magnetic field oriented perpendicular relative to each other, respectively. Spin relaxation of charge carriers are traditionally defined using Bloch-Torrey equations,

$$\begin{aligned} {\partial S_x}/{\partial t} &= \gamma(\boldsymbol{B} \times \boldsymbol{S})_x - {S_x}/{T_2} + D\nabla^2 S_x, \\ {\partial S_y}/{\partial t} &= \gamma(\boldsymbol{B} \times \boldsymbol{S})_y - {S_y}/{T_2} + D\nabla^2 S_y\,, \\ {\partial S_x}/{\partial t} &= \gamma(\boldsymbol{B} \times \boldsymbol{S})_z - {S_z}/{T_1} + D\nabla^2 S_z \end{aligned} \qquad (3.2.1.2)$$

where D is the diffusion constant and $\gamma = 2\pi\mu_B g/h$ is the electron gyromagnetic ratio where μ_B is the Bohr magneton and g is the electronic g-factor.

3.3 SPIN-ORBIT COUPLING

In the presence of spin-orbit interaction the Bloch equations can no longer describe charge carrier spin dynamics since the intrinsic spin **S** is no longer a good quantum number. Sources of electric field could be ionic impurities and crystals lacking inversion symmetry. The nature of spin-orbit coupling λ could be explained in terms of periodic lattice potential V_{SC}, linear momentum $\boldsymbol{p}$ and Pauli spin matrix $\boldsymbol{\sigma}$ as follows

$$\lambda = \frac{\hbar}{4\pi m^2 c^2} \nabla V_{sc} \times \boldsymbol{p}.\boldsymbol{\sigma} \qquad (3.3.1)$$

Spin-orbit coupling causes mixing of spin states, and hence eigenstates corresponding to *n* orbital are described as follows,

$$|n\uparrow\rangle = \alpha_n|\uparrow\rangle + \beta_n|\downarrow\rangle \qquad (3.3.2)$$

and its time reversal partner,

$$|n'\downarrow\rangle = \alpha_n^*|\downarrow\rangle - \beta_n^*|\uparrow\rangle \qquad (3.3.3)$$

where α_n, α_n^*, β_n^* and β_n are spin state weighing coefficients. The mixing of spin states reduces the Zeeman splitting; due to Kramer's degeneracy each orbital state labelled with an index *n* is double degenerate. This phenomenon can be well understood in relation to Elliot-Yafet spin relaxation mechanisms which constitute the main spin-orbit scattering mechanism in metals [1].

3.3.1 Elliot-Yafet (EY) relaxation mechanism

Non-uniform distribution of scattering sites results in quantum levels with different effective spin-orbit matrix element manifested by quantum levels with different g-factors. Moreover, conduction electrons may flip spins after every scattering with some small probability $|\beta_n|^2$, giving rise to some mean spin scattering time. According to Elliot's findings[1], ordinary scattering (spin independent) of electrons with impurities, boundary and phonons can couple "spin up" and "spin down" electrons leading to spin relaxation T_1which is proportional to momentum relaxation time τ.

According to Yafet [1], additional spin relaxation is brought by spin-orbit coupling of impurities and phonon-modulated spin-orbit coupling of the lattice ions. The latter mechanisms should be combined with Elliot mechanism to describe spin relaxation at low temperatures where both mechanisms have dominant contribution. Hence one describes the combined effect as Elliot-Yafet in terms of T_1 and momentum scattering time τ,

$$1/T_1 = C_{EK}.\,1/\tau \qquad (3.3.4)$$

Thus spin-flip length ($\lambda_{sf} = \sqrt{DT_1}$) is proportional to mean free path since a diffusion constant *D* is proportional to momentum scattering time *τ*.

3.3.2 D'yakonov-Perel' (DP) relaxation mechanisms

In crystals lacking inversion symmetry, such as zinc-blende structure, possible spin-orbit coupling lifts spin degeneracy, and therefore the spin up and spin down state have different energies even if they have same momentum state $\boldsymbol{k}$. D'yakonov and Perel'[2] showed that the lifting of spin degeneracy leads to spin relaxation.

Consider a rapid scattering of an electron original in momentum state $\boldsymbol{k}$ and precessing about the intrinsic field $\boldsymbol{B(k)}$; an electron precesses about a new effective magnetic field $\boldsymbol{B(k')}$ in a new momentum state $\boldsymbol{k'}$ without appreciable completing a cycle. Since an effective magnetic field changes with momentum states; one expects an electron spins to precess with Larmor frequencies $\boldsymbol{\omega}(\boldsymbol{k}) = {}^{e}/_{m}\,\boldsymbol{B}(\boldsymbol{k})$ about different axes given by effective magnetic fields $\boldsymbol{B(k^i)}$ of different directions denoted by superscript *i*.

Since a precession direction and frequency change randomly after every collision, a precession angle along an axis of initial polarization diffuses so its square becomes about $(t/\tau)(\omega\tau)^2$ after time *t*. When a precession angle is an order of magnitude, one can define the characteristic time $1/T_1 \approx \omega(\omega\tau)$. It is therefore clear that spin precession in different random directions, corresponding to different effective fields $\boldsymbol{B(k^i)}$ and different frequencies causes spin-flip scattering T_1which is inversely proportional to momentum scattering *τ*.

The difference between DP and EY mechanisms lies on their different dependence on the momentum relaxation time; unlike in EY mechanisms, DP spin relaxation time $T_1$is inversely proportional to momentum relaxation time *τ*. Moreover one can experimental distinguish between these mechanisms through investigation of the dependence of electron spin diffusion length $\lambda_{sf} = \sqrt{D\tau}$ on momentum scattering time *τ*. Unlike in EY mechanisms, the spin diffusion length has no dependence on

momentum scattering time and for degenerate electron system it should be temperature independent. Strong scattering make EY mechanism more significant than DP relaxation since the loss of phase in the EY mechanism is a minimal, i.e. loss of phase in EY occurs only during collision.

3.4 PARAMAGNETIC ION RELAXATION VIA PHONONS

The above relaxation mechanisms are mainly considering a transfer of magnetic energy by charge-carriers into a lattice via spin-orbit coupling. However in the case large concentration of paramagnetic ions (electrons in localize states), spin relaxation of localized spins usually occurs through modulation of crystal field by phonons [3, 4]. Hence phonons indirectly trigger spin relaxation of localized spins, and the possible relaxation mechanisms are driven by phonons and are known as Raman, direct, and Orbach process [5, 6, 7, 8, 9]. Temperature dependence of the spin relaxation mechanisms is summarized as follows;

$$1/\tau_R = T^7/C_R\Delta^2 \tag{3.4.1}$$

$$1/\tau_D = T/C_D \tag{3.4.2}$$

$$1/\tau_O = \Delta^3/\{C_O.\exp[\Delta/k_BT] - 1\} \tag{3.4.3}$$

where expression (3.4.1), (3.4.2) and (3.4.3) represents Raman, direct, and Orbach process, respectively. The parameter Δ represents separation of ground and excited energy levels.

The effect of these relaxations should be negligible in graphitic carbons due to large fraction of charge-carriers in p_z-orbitals (associated with graphitic structures) suppressing any relaxation of localized electron spins into a lattice.

3.5 EXCHANGE SPIN COUPLING

In the presence of small spin density, localized and carrier spins embedded on lattice can exchange their energies, and thus stimulate spin relaxation of charge carrier spins through spin-orbit interaction as in traditional paramagnetic alloys such as CuMn and iron[10] shown in Figure 3.5.1. Non-bonding π-electrons are localized; hence they are analogous to the *d* spins in CuMn; likewise, charge carriers have *s* spins and can therefore relax via spin-orbit into lattice T_{s1} as shown on the right side of Figure 3.5.1.

In such an *s-d exchange* configuration that there are two competing relaxation mechanisms which are both linearly dependent on temperature, as shown on resonance linewidth relations (3.5.1) and (3.5.2), and they are the bottleneck and Korringa-type relaxation [11, 12].

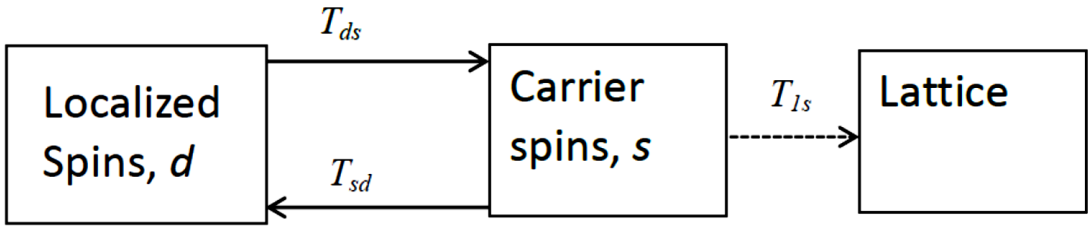

Figure 3.5.1 A schematic showings s-d exchange or spin coupling; electrons in d-states and s-states are localized and carriers (conducting), respectively.

The magnitude or strength of spin-orbit coupling is a useful measure to successfully discriminate the two relaxation mechanisms. When localized spins *d* lose their magnetic energies to carrier electrons spins *s* by Korringa-type relaxation mechanism T_{ds}; carrier electron spins *s* respond by simple relaxing back T_{sd} at either higher rate or slower rate in comparison to the rate at which charge carriers are relaxing into lattice $T_{1s.}$ When carrier electron spins relax into localized spins at higher rate than they are relaxing into a lattice, carrier electrons have bottleneck dissipation of energy into lattice and effective relaxation rate $1/T_{eff}$ which is proportional to ESR linewidth ΔB expressed as

$$\gamma \Delta B \cong \frac{1}{T_{eff}} = \{3\rho(E_F)k_B T\}/\{2S(S+1)C.T_{1s}\} \qquad (3.5.1)$$

and therefore an effective relaxation rate $1/T_{eff}$ for localized spins is directly proportional to carrier spins relaxation rate $1/T_{1s}$ and inversely proportional to concentration of localized spins *C*. From above relation (3.5.1), it is clear that resonance linewidth ΔB increases linearly with temperature and the limit in temperature is in accordance with Hasegawa's relation [13]. Quantities in relation (3.5.1) are *S, ρ (E_F)* and *C* represents localized electron spin, density of states at the Fermi level and number of localized spins, respectively.

Korringa-type relaxation mechanisms prevail if the rate at which carrier electrons relax into lattice is higher than it relax into localized spins, $T_{1s} << T_{sd}$, and is given by relation

$$\gamma \Delta B \cong \frac{1}{T_{s1}} = 4\pi J^2 N^2(0) k_B T/\hbar \qquad (3.5.2)$$

where *J* is the exchange integral.

3.6 HYPERFINE INTERACTIONS

Magnetic interaction between magnetic nuclei and electrons provides an efficient mechanism for an ensemble spin dephasing [14] and single-spin dephasing of localized electrons. The importance of this interaction is seen when there is an appreciable amount of magnetic nuclei interacting with localized electrons; localized electrons could be the ones trapped in quantum dot or bound in impurities and/or donors. Among hyperfine interactions, the Fermi contact potential energy has the effective Hamiltonian *H* given as

$$H = \frac{8\pi}{3}\frac{\mu_0}{4\pi} g_0 \mu_B \sum_i \hbar \gamma_{n,i} \boldsymbol{S}.\boldsymbol{I}_i \delta(\boldsymbol{r} - \boldsymbol{R}_i) \qquad (3.6.1)$$

in terms of free-electron g-factor ($g_e = 2.0023$), nuclear position $\boldsymbol{R_i}$, and electron and nuclear spin operators $\boldsymbol{S}$ and $\boldsymbol{I_i}$, respectively. Hyperfine interaction has negligible effects on spin relaxation of metals and bulk semiconductors since this effect are strongly narrowed dynamically by carrier electrons [15].

In graphitic and carbonaceous materials this effect should be drastically reduced due to dominating carrier π-electrons and negligible concentration of magnetic carbon and nitrogen nuclei (approximately 1 % for ^{13}C and about 0.4 % for ^{15}N). However this interaction is desirable in spintronics and quantum information where it is commonly used to couple electron and nuclear spins in a controlled manner.

3.7 THE SIGNIFICANCE OF ESR PARAMETERS

Continuous-wave ESR spectroscopic technique generally described microscopic magnetic ordering using three parameters: g-factor, first derivative peak-to-peak linewidth ΔB and amplitude ΔM.

- Peak-to-peak amplitude ΔM is related to static susceptibility and therefore to unpaired electron spins; peak-to-peak amplitude drawn against temperature tells more about the degree of localization of unpaired electron spins. When ΔM is measured as a function of microwave power, the nature of relaxation mechanism; amplitude saturates at low microwave power for relaxation governed by spin dephasing time T_2; the spin-lattice relaxation time $T_1 = 10^{-8}s$ measured for graphite nanoparticles rule out ordinary electron-phonon relaxation mechanism related to acoustic phonons in graphite [16].
- In case of scattering processes govern by charge-carriers, ΔB is proportional to relaxation rate $1/T_1$(Elliot mechanism). When plotted against temperature, ΔB describes nature of interaction among spins and other scattering mechanisms of electron spins within an environment, and thus it also determines electrical conductivity [17].

- The g-factor is inversely proportional to resonance field B_0, $g = h\nu/\mu_B B_0$, where ν represents microwave frequency which is normally in Giga-Hertz(GHz). g-factor is determined by local chemical environments.

3.8 RESONANCE LINESHAPE ANALYSIS

Dysonian shape resonance line often observed in metals and graphite is attributed to large concentration of charge carriers [18]. Dyson *et al.*[19] showed the dependence of resonance lineshape on the following parameters,

- spin-lattice relaxation T_1
- electron spin-spin relaxation timeT_2(for metals $T_1 = T_2$)
- time it take an electron to diffuse T_D through skin depth δ
- and time it takes an electron to transverse T_T a sample.

In a region of normal skin depth, the electron mean free path is small in comparison to skin depth δ, and a corresponding resonance lineshape is Lorentzian; the condition $T_T \ll T_D$ issatisfied and thus independent of diffusion.

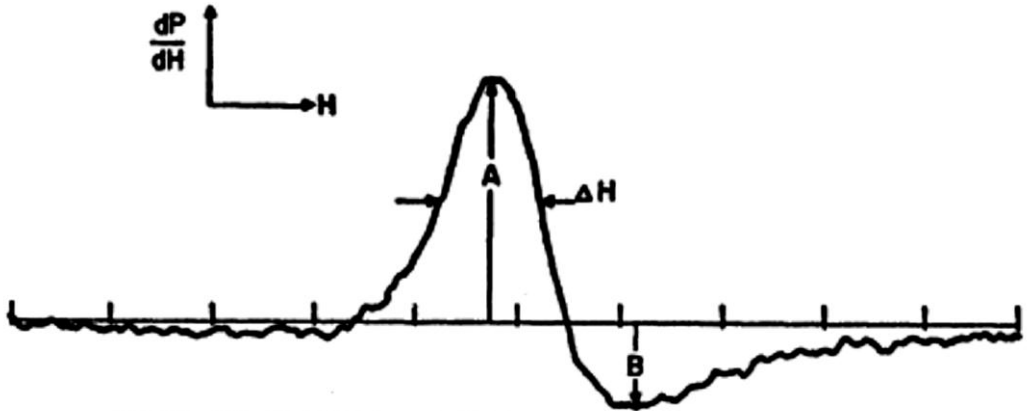

Figure 3.8.1 Typical Dysonian resonance line with positive and negative amplitude represented as A and B, respectively [22].

However, metals or highly conductive samples satisfy the condition $T_T \gg T_2 \gg T_D$ which describes rapidly diffusing electron spins through skin depth. In case metals contain some paramagnetic impurities distributed throughout a volume *V*, the condition $T_T \gg T_D \gg T_2$ is met and it described a slowly diffusing magnetic dipoles.

Diffusion of spin out the skin depth δ increases resonance line peak amplitudes ratio A/B and assumes the condition $T_D \ll T_2$. One can express T_D as, $T_D = \frac{3\delta^2}{2v\Lambda}$ (where *v* represents electronic mean velocity), when normal skin-depth $\Lambda << \delta$ is assumed. In this context, one can therefore express electrical conductivity as,

$$\sigma = \frac{Ne^2\Lambda}{m^*v} \tag{3.8.1}$$

where *N* and m^* is the number of electrons and electronic effective mass, respectively. While a value of T_2 is often set by impurity content, T_D is governed by lattice scattering hence one might expect changes of its value as temperature changes.

3.9 SPIN SUSCEPTIBILITY

The magnetic moment of an electron is determined by adding its orbital and spin magnetic moments in an appropriate way. However, the interaction of magnetic moment with surrounding fluctuating lattice field may "quench" the orbital motion of an electron resulting in g-factor solely determined by intrinsic spin. Hence, the magnetic moments can interact spontaneously (ferromagnetism) at low temperatures or randomly oriented at high temperatures (paramagnetism).

The spin polarization can be probed with ESR spectroscopy; intensity *I* of ESR signal (proportional to a square of ESR amplitude) is proportional to static spin susceptibility χ_0 of a sample being measured, as

$$I = \pi B_0 \chi_0 / 2 \tag{3.9.1}$$

Consider a material composed of non-interacting spins acting as an ensemble of independent magnetic moments. One can deduce magnetization of such a material using the statistical mechanical approach,

$$\langle M \rangle = \frac{N}{V} g_J \mu_B J B_J \left(\frac{g_J \mu_B B_0 J}{k_B T} \right) \tag{3.9.2}$$

where g_J is the Lande g-factor, J is the total angular momentum, and $B_J(x)$ is the Brilloun function,

$$B_J(x) = \frac{2J+1}{2J} \coth\left(\frac{2J+1}{2J} x \right) - \frac{1}{2J} coth\left(\frac{1}{2J} x \right) \tag{3.9.3}$$

If one assumes weak applied magnetic field ($B \to 0$), the Curie susceptibility can be expressed as,

$$\chi_C = \mu_0 \lim_{B_0 \to 0} \frac{M_0}{B_0} = \mu_0 \frac{S(S+1) g^2 \mu_B^2}{3 k_B T} . \frac{1}{V_c} \tag{3.9.4}$$

and is inversely proportional to temperature and unit cell volume $V_c = {}^{V}/_{N}$. The replacement of J by S in the above expression (3.9.4) is necessary since orbital momentum L is quenched for materials possessing the Curie susceptibility.

The same cannot be said about carrier electrons due to their indistinguishability property, and they obey Pauli principle. Occupation of states by carrier electrons is governed by Pauli principle, and furthermore it also reduces susceptibility below Curie law value by hindering spin alignment. The occupation of states can be described in terms of Fermi-Dirac distribution,

$$f(\varepsilon) = 1/(e^{\beta(\varepsilon - \mu_c)} + 1) \tag{3.9.5}$$

where μ_c is the chemical potential. The Fermi level of spin-up and spin-down configuration, in the density of states of carrier electrons, can be shifted in energy Δ in opposite direction by same amount in the presence of magnetic field B. This eventually results in excess electrons with one of the two spin configurations as shown in Figure 3.9.1.

A magnetic moment (which points in opposite direction of spin, $\boldsymbol{\mu} = -g\mu_B \boldsymbol{s}$) is generated by electron near the Fermi energy E_F, hence susceptibility can be expressed in terms of Fermi density of states $g(E_F)$ as

$$\chi_P = \frac{1}{4} g_e^2 \mu_0 \mu_B^2 g(E_F) \frac{1}{V_c} \tag{3.9.6}$$

where g_e and μ_0 is free electron g-factor and magnetic permeability, respectively.

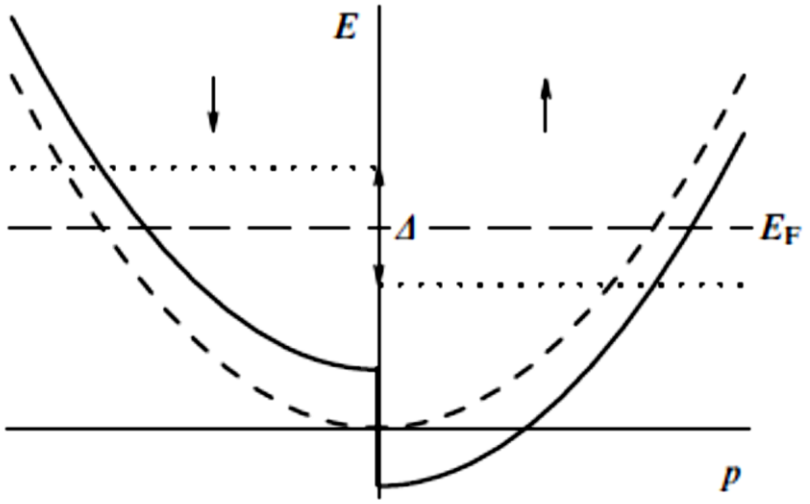

Figure 3.9.1 Spin-related shift of electronic energy in response to applied magnetic field *B*.

3.10 CYCLOTRON RESONANCE AND DIAMAGNETISM

In some materials whereby surrounding fluctuating lattice field cannot completely "quench" the orbital angular momentum, the electronic g-factor is not exactly being equals to 2. The magnetic moment will have contribution from orbital motion of an electron. Hence, electron spin resonance and cyclotron resonance can occur concurrently as in some metals and semi-conductors; the corresponding electronic

energy spectrum could then be described by Zeeman and Landau levels, respectively [20].

Cyclotron resonance can be described as selective absorption of continuous electromagnetic energy by charged-carriers in magnetic field *H*; absorption occurs at frequencies which are equal to the cyclotron frequency of charge carriers or multiples of cyclotron frequency, $\omega = n\omega_c$ (where n is an integer representing possible harmonics).

In a continuous microwave field *E* and constant magnetic field *H*, charge carriers may move along helical orbits whose axes are parallel to static magnetic field (shown in Figure 3.10.1) due to Lorentz force. In a plane perpendicular to static magnetic field *B*, charge carriers undergo periodic motion at cyclotron frequency ω_c and those electrons occupy allowable discrete states called Landau levels. The Landau levels have energies described as

$$E_n = \left(n + \frac{1}{2}\right)\frac{\hbar eH}{mc} \qquad (3.10.1)$$

where *n* is an integer and $\omega_c = eH/mc$ is the frequency of quantum transition between Landau levels.

Cyclotron resonance may be observed in various conductors. Examples include cyclotron resonance of electrons or ions in gaseous plasmas, cyclotron resonance of charge carriers in metals, cyclotron resonance of excess charge carriers generated by light or heating in semiconductors and dielectrics, and cyclotron resonance in two-dimensional systems.

The sharpness of cyclotron resonance in solids depends primarily on the broadness of energy levels $\Delta\varepsilon$; the uncertainty principle describes broadening in terms of mean time τ between collisions as follow

$$\Delta\varepsilon \cong \hbar/\tau \qquad (3.10.2)$$

In case $\hbar/\tau > \hbar\omega_c$, cyclotron resonance features are absent due to large scattering experienced by charge-carriers who could not even complete one revolution. Therefore to mitigate electron-phonon scattering, cyclotron resonance is usual done at either low temperatures or high magnetic field. However, this is in contrast to cyclotron resonance observed in semiconductors; raising the temperature results in excess charge-carriers in periodic motion over the 2D plane normal to field and they are occupying Landau levels. The maximum relaxation times τ achievable in practice place a lower limit on the frequency range (ν > 1 GHz) in which cyclotron resonance may be observed in solid conductors.

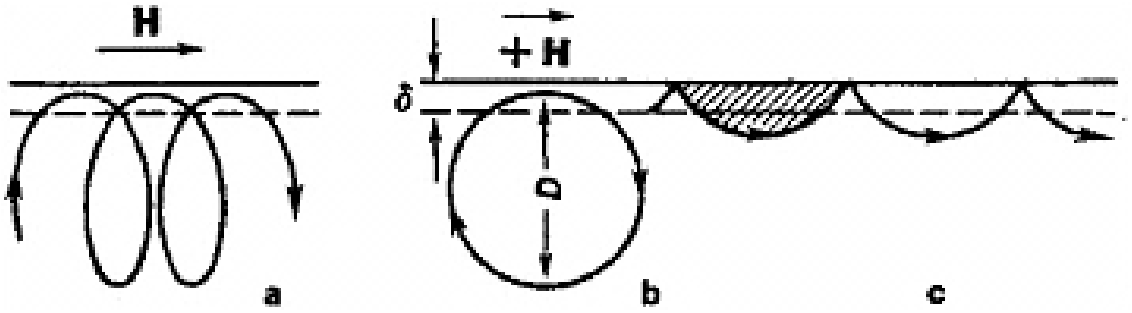

Figure 3.10.1 Electron trajectories: (a) in a uniform static field H under the action of an alternating electric field E ⊥ H, (b) in a metal in a magnetic field H parallel to the surface of the metal, and (c) in the case of specular reflection from the surface of a metal.

Cyclotron resonance of metal and semiconductors occurs at different ranges of frequencies, $\omega_c \gg \omega_p = \sqrt{4\pi Ne^2/m^*}$ and $\omega_c \ll \omega_p$ for semiconductors and metals, respectively. This difference in resonance frequencies comes from their different carrier densities ($N \approx 10^{22}\text{cm}^{-3}$ in metals and 10^{14}–10^{15}cm^{-3} in semiconductors), and therefore they have different skin-depths δ; ω_p represents the plasma frequency of charge-carriers and m^* is their effective mass. Hence skin-depth also governs the sharpness of cyclotron resonance. Since cyclotron resonance increases particle's energy E and thus leading to large diameter D of a particle's orbit and increment Δv of a mean velocity v, and thus enhanced electrical conductivity σ is observed at resonance. Electrical conductivity is proportional to Nev/E, where e is the elementary charge.

3.11 DIAMAGNETIC RESONANCE IN GRAPHITIC CARBONS

Graphite consists of parallel hexagonal layers over which clouds of delocalized electrons could be considered as good example of two-dimensional systems. Uniform electromagnetic field of frequency $\omega = eH/mc$ may also results in cyclotron resonance or diamagnetic resonance of delocalized electron clouds since circular motion of charge-carriers results in diamagnetism of electron gas, Landau diamagnetism. Landau diamagnetism is also known as orbital diamagnetism owing to orbital motion of charge-carriers in 2D plane normal to static magnetic field H.

If a constant electric field is applied perpendicular onto surface of a semiconductor, an excess concentration of charge carriers that can move freely only along a surface arises from surface layer, which has a thickness of ~1-10 nm. Temperature dependent diamagnetism, orbital diamagnetism, has been seen in graphite, multi-walled carbon nanotubes (MWNTs) and other turbo-stratic carbons. Since MWNTs and turbostatic carbon have almost perfect graphene sheets with poor alignment along the azimuthal direction, MWNTs could be thought to belong to a class of quasi-two dimensional graphites (QTDGs); hence their electronic and magnetic properties are described in terms of QTDG band model[21]. This model assumes electrical transport and

magnetic dominated by charge-carriers, however effect of localized electrons associated with defective layers cannot be ignored at low temperatures.

This model also described temperature dependent orbital diamagnetic susceptibility observed in MWNTs; it is due to component of magnetic susceptibility normal to graphene layers. ESR intensity is proportional to Pauli paramagnetic susceptibility χ_P, and therefore also proportional to one-third of orbital diamagnetic susceptibility χ_{orb} or χ_L (the condition valid at high temperatures),

$$\chi_L = -\frac{1}{3}\chi_P \qquad (3.11.1)$$

In contrast to χ_P whose spectrum is continuous (Figure 3.9.1), it should be noted that χ_L have discrete values, Landau levels. Hence ESR intensity determines the concentration of charge-carriers in carbon system which could be varying with temperature.

References

1. Elliot R. J., *Phys. Rev.***96**, 266 (1954); Y. Yafet, *Phys. Rev.* **85**, 478 (1952).
2. D'yakonov M. I., and Perel' V. I., *Sov. Phys. JETP* **33**, 1053 (1971); *Sov. Phys. Solid State* **13**, 3023 (1972).
3. Heitler W. and Teller E., *Proc. Roy. Soc.* (London) A **155**, 886(1936).
4. Van Vleck J. H., *Phys. Rev*. **57**, 426 (1940).
5. Manenkov A. A. and Orbach R. Ed, *Spin-Lattice Relaxation in Ionic Solids.* New York: Harper and Row, 1966.
6. Orbach R., *Proc. Roy. Soc.* (London) A**264**, 458 (1961a).
7. Orton J. W., *Electron Paramagnetic Resonance: An Introduction to Transition Ions.* London Illife Books, 1968.
8. Abragam A. and Bleaney B., *Electron Paramagnetic Resonance of Transition Ions.* Oxford: Clarendon Press, 1970.
9. Poole Jr. C. P. and Farach H. A., *Relaxation in Magnetic Resonance.* New York: Academic Press, 1971.
10. Nakamura A. and Kinoshita N., *Bull. Electrotech. Lab*. **30**, 19 (1966)[in Japanese].
11. Nakamura A. and Kinoshita N., *J. Phys. Soc. Jpn.***22**, 2 (1967).
12. Korringa J., *Physica*, **16**, 601 (1950).
13. Hasegawa H., *Prog. Theor. Phys. (Kyoto)* **21**, 483 (1959).
14. D'yakonov M. I. and Perel' V. I., *Sov. Phys. JETP* **38**, 177 (1973).
15. Overhauser A. W., *Phys. Rev.* **89**, 689 (1953).

16. Anderson O. E., Prasad B. L. V., Sato H. *et al.*, *Phys. Rev. B* **58**, 16387 (1998).

17. Dersch H., Stuke J. and Beichler J., *Phys. Stat. Sol. (b)* **107**, 307 (1981).

18. Feher G. and Kip A. F., *Phys. Rev.* **98**, 337 (1955).

19. Dyson F. J., *Phys. Rev*. **98**, 349 (1955).

20. Guiliani G. F. and Quinni J. J., 1986, *Magnetic instability of 2DEG*.

21. Kotosonov A. S. and Kuvshinnikov S. V., *Phys. Lett. A*, 1997, submitted.

22. Wagoner G., *Phys. Rev.* **118**, 2 (1960).

CHAPTER 4

EXPERIMENTAL SET-UP

4.1 SAMPLE PREPARATION AND CHARACTERIZATION

The carbon nanospheres of different diameters were synthesized using chemical vapor deposition (CVD) in the vertical and horizontal reactor. Synthesis and structural characterization were conducted by Kunjuzwa [1] as part of her MSc degree within the School of Chemistry at Wits University. This work is reported without any aim of alteration or reviewing the author's original idea but to familiarize the reader with the nature of the samples whose magnetic properties are investigated.

The structural features and characterization were mainly made possible using TEM/HRTEM, Raman, and XRD. Section 4.1.1describes the method used for synthesis of carbon nanospheres in the vertical reactor, as well as the summary describing their structural features. The method used for synthesis of spheres in the horizontal reactor is also described in section 4.1.2. Further details regarding these samples are given by Kunjuzwa.

4.1.1 Synthesis within the vertical reactor

A. Pristine carbon nanospheres

The pristine carbon nanospheres were synthesized without any nitrogen source; the nitrogen gas was run through the reactor just to flush out any contaminants that might be present. Prior to sample synthesis the temperature at the furnace was set to 1000 ^{0}C and the temperature was monitored using thermocouple and/or temperature gauge. The acetylene and argon gas were then fed into the reactor at different flow rates 487 ml/min and 100 ml/min, respectively. The argon gas was used to promote or favor pyrolysis of hydrocarbons. The deposition process took nearly 5 minutes and the spheres were cooled in a condenser and collected from cyclones shown in Figure 4.1.1.1. The CVD apparatus consists of swirled mixer [7]; vaporizer [6]; furnace [2]; reactor [1]; condenser [3] and two cyclones labeled [4] and [5]. At the bottom end of

the reactor, the hydrocarbons, argon and nitrogen sources are first fed into a vaporizer, mixed in the swirled mixer and then fed into the reactor. The reactor is immersed in the furnace whose temperature is monitored with sensitive temperature gauge [not shown]. The top end of the reactor leads to the condenser, which in turn leads into two cyclones labeled [4] and [5] where samples were collected.

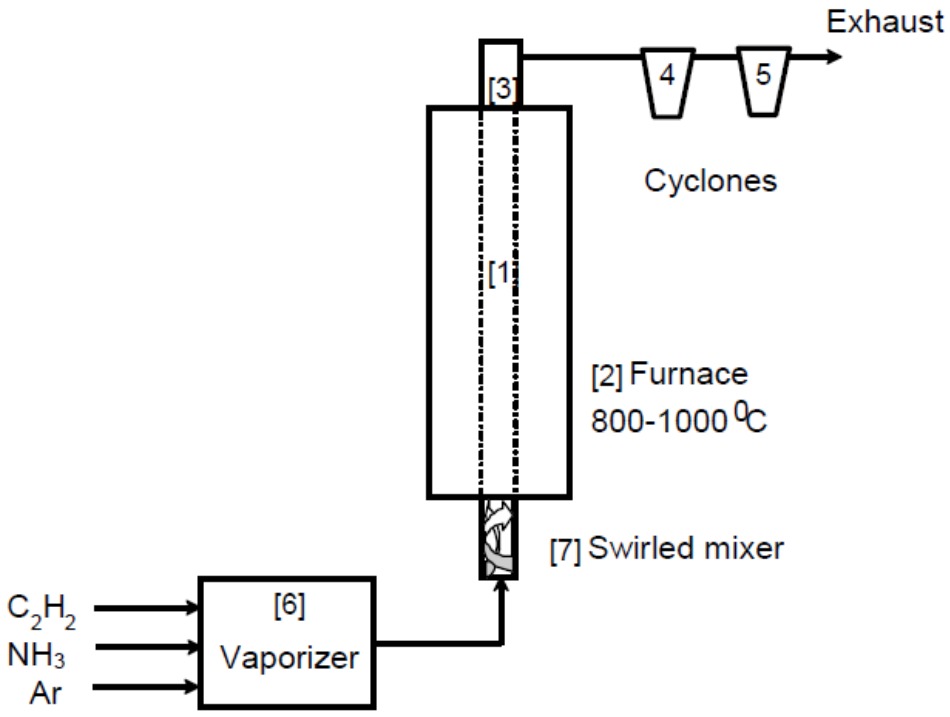

Figure 4.1.1.1 Schematic showing the catalytic CVD vertical. The CVD apparatus consists of swirled mixer [7]; vaporizer [6]; furnace [2]; reactor [1]; condenser [3] and two cyclones labeled [4] and [5].

B. The nitrogen doped carbon nanospheres

The ammonia gas was fed into the reactor together with acetylene without any Ar gas; the temperature of the furnace was kept constant at about 1000 ^{0}C. As in the case of pristine spheres, the flow rate of C_2H_2 was kept constant at 487 ml/min while that of NH_3 was kept at 100 ml/min.

The pyridine was in the liquid phase and was vaporized through heating the solution to about 125 ^{0}C. The N doping of spheres was made possible through bubbling the C_2H_2: Ar mixture in the 100 % solution of pyridine. The flow rate of Ar and C_2H_2 were kept constant as in the case of ammonia gas. The temperature of the furnace was also set at constant for the rest of deposition process.

Syntheses of the carbon spheres in the present of ammonium hydroxide solution were done through the C_2H_2: Ar mixture bubbling in ammonium hydroxide solution. The temperature of the furnace was varied between 850-1050 ^{0}C while feeding Ar and C_2H_2 into the reactor at different flow rate; Ar flow rate was constant (100mL/min) and flow rate of was C_2H_2 varied between 370-594 mL/min.

4.1.1(A) Summary of Results from vertical reactor

The elemental analysis showed (in Table 4.1.1.1) that carbon nanospheres prepared in the presence of ammonium hydroxide solution have large nitrogen content in comparisons to doped spheres prepared from ammonia or pyridine as N source. The TEM images clearly showed that the bulk carbon nanospheres consist of carbon balls link together to form a necklace of some kind. The HRTEM images, in Figure 4.1.1.2, further showed that the carbon spheres produced have signature of disordered graphitic carbon.

Table 4.1.1.1 Carbon nanospheres produced within the CVD vertical reactor and different precursors. Ammonium hydroxide was a solution while ammonia and pyridine were in gaseous and liquid (aqueous) phase, respectively.

Sample Labels	N(source) (%Volume)	Carbon (%)	Nitrogen (%)	Yield (g)
NK1	No Nitrogen	>98.00	<0.02	1.30
NK2	Ammonia gas	98.00	0.19	0.20
NK3	25%NH_4OH(aq)	92.26	3.08	0.75
NK4	Pyridine	98.42	0.15	0.20

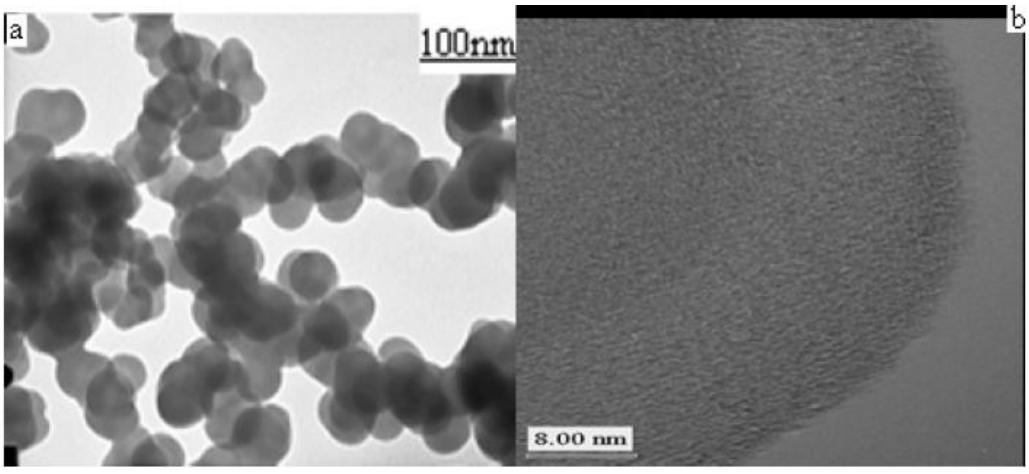

Figure 4.1.1.2 TEM (left) and HRTEM (right) images showing post heated spheres under EM.

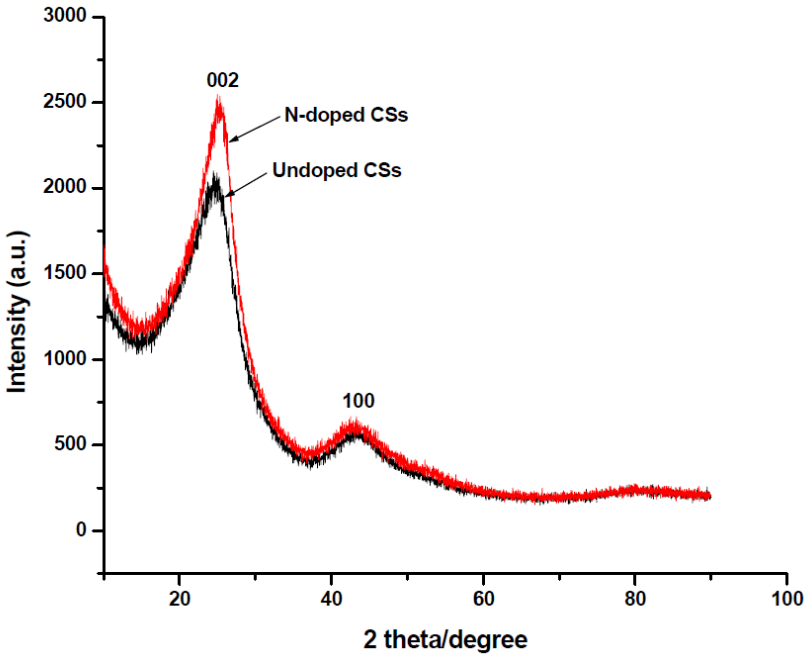

Figure 4.1.1.3 XRD patterns with different intensity (along 002 plane) for doped and pristine spheres (shown by arrows) due to poor graphene packing along c-axes.

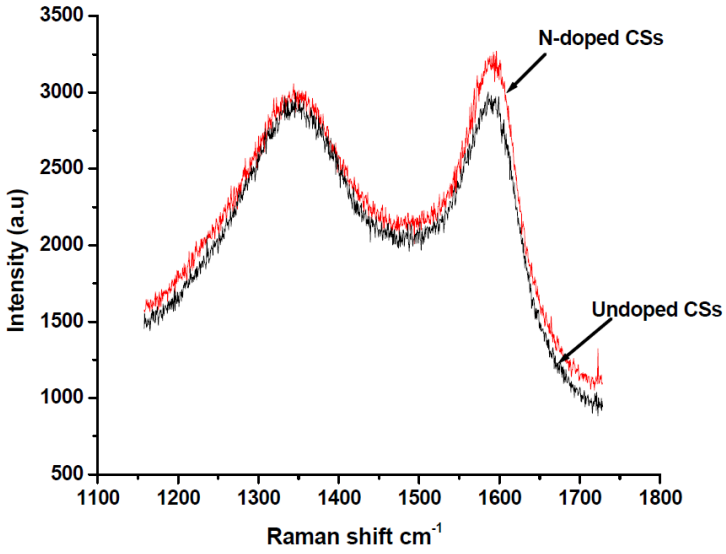

Figure 4.1.1.4 Raman confirmed more disordered graphitic structure occurs in doped spheres (shown by arrows).

The same structural features of the carbon nanospheres were further confirmed with X-ray diffraction and Raman spectroscopy, as shown in Figure 4.1.1.3 and Figure 4.1.1.4, respectively.

The Raman measurements on doped spheres (using NH_4OH as N source) prepared at 1000 ^{0}C show the G and D peak at 1591 cm^{-1} and 1348 cm^{-1} corresponding to graphite and disorder induced mode in graphite, respectively. The D and G peak intensity ratio was increasing with increasing concentration of nitrogen incorporated within the carbon spheres and that was attributed to the reduction of graphitization. The value of I_D/I_G ratio measured for the carbon nanospheres sample above is approximately 0.9.

The XRD patterns (Figure 4.1.1.3) also supported these findings; the strong and broad peak at about 25^0 at the plane (002) was measured for both pristine and doped carbon spheres. The position of the crystallographic plane (002) with large intensity and broadness implies the presence of poor alignment of small graphitic crystallites along the c-axis. The doped spheres are more disordered in comparison to pristine carbon spheres.

4.1.2 Synthesis within the horizontal reactor

The horizontal reactor comprises of furnace, quartz tube, gas bubbler, temperature gauge, water cooled injector in which a syringe in inserted as shown in Figure 4.1.2.1. The pyrolysis temperature and hydrocarbons flow rate of precursors were kept at 1000 ^{0}C and 0.8 mL/min, respectively. The hydrocarbons used were limited to toluene and pyridine which were expected to produce host atoms (carbon) and foreign atoms (nitrogen), respectively.

Different ratios of toluene to pyridine were injected separately through water cooled injector and into the reactor at same rates, respectively (shown in Table 4.1.2.1). Most carbon spheres were collected from the middle of the reactor tube after reaction which took place for nearly 2 hours. It is important to note that no catalyst was used to speed the reaction.

The elemental analyses (shown in Table 4.1.2.1) revealed that all carbon nanospheres produced contain different amount of nitrogen even in the case of sample labeled NK8, which was produced without any nitrogen containing hydrocarbons. The doped carbon spheres containing large amount of nitrogen was NK6 and was produced solely from pyridine as a source of both host and foreign atoms. The TEM and HRTEM images illustrate that spheres produced from a mixture of pyridine and toluene have diameter distribution in the range 500-1000 nm.

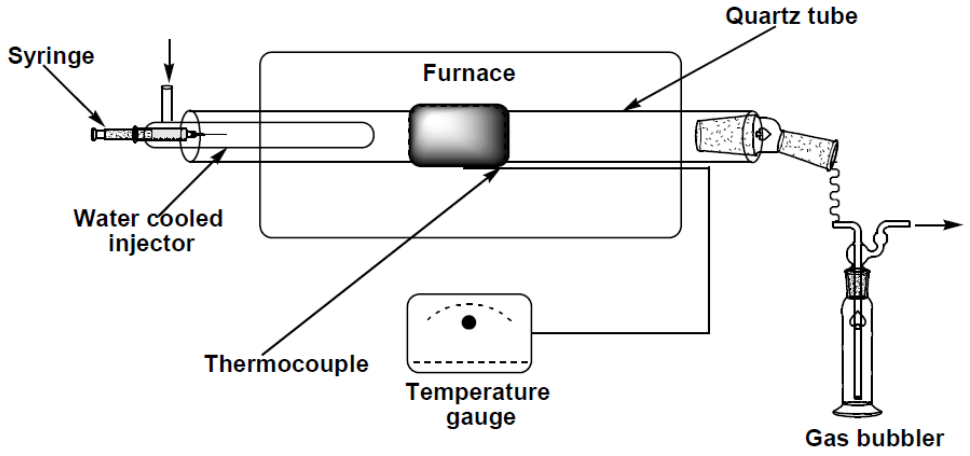

Figure 4.1.2.1 Schematic shows the configuration of the horizontal CVD reactor.

4.1.2(B) Carbon nanospheres characterization (horizontal reactor)

NK8 was produced solely from toluene and the bulk carbon spheres consisted of the large distribution of carbon balls with different diameter, in the range of 200-700 nm. The HRTEM images and electron diffraction patterns revealed that the carbon sphere (NK8) consists of carbon balls with core/shell geometry and the outer shells are crystalline and graphitic (shown as inset of Figure 4.1.2.2).

Table 4.1.2.1 Carbon nanospheres produced from horizontal reactor using different ratios of toluene to pyridine. NK6 and NK8 were synthesized solely from pyrolysis of pyridine and toluene, respectively.

Sample Label	Pyridine: Toluene %Volume	Carbon content (%)	Nitrogen Content (%)	Yield(g)
NK6	100:0	87	5.00	0.60
NK9	90:10	91.97	3.52	0.55
NK7	10:90	94.19	1.48	0.35
NK8	0:100	98.94	0.13	0.40

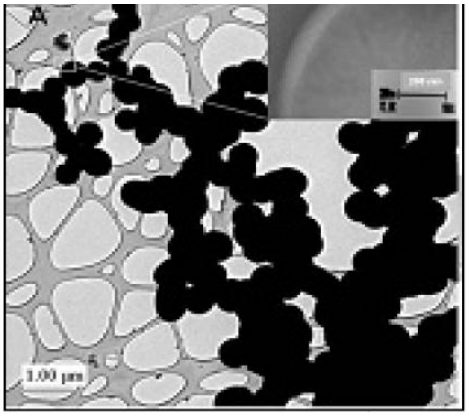

Figure 4.1.2.2 TEM images of pristine sphere (NK8) and electron diffraction patterns (inset). Distinct black and white fringes were clearly seen.

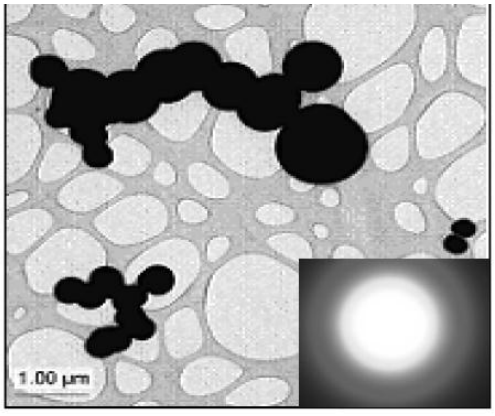

Figure 4.1.2.3 TEM images of N doped spheres and electron diffraction pattern (inset) revealed more disordered structure.

In contrast to pristine carbon nanospheres(in Figure 4.1.2.2), the nitrogen doped carbon nanospheres consisted of disordered arrays of nanographene sheets as shown on HRTEM image and poor resolved electron diffraction pattern (inset) in Figure 4.1.2.3. In addition, no core/shell configurations were observed for the agglomerated carbon balls comprising the bulk N doped carbon nanospheres.

4.2 ESR EXPERIMENT

4.2.1 Low Temperature measurements

The continuous wave (cw) ESR measurements were performed using Bruker ESP300E spectrometer operating at X-band in the frequency range 9.53- 9.57 GHz. The spectrometer was equipped with high Q cavity placed within an Oxford continuous flow cryostat, operating in conjunction with an Oxford instruments ITC 503 temperature controller. Liquid nitrogen (80- 320 K) and liquid helium (4- 80 K) were used as cryogens. Temperatures were maintained to a precision of better than 0.3 K above 80 K, and to a precision of better than 0.1 K below 80 K. All measurements on samples (NK6, NK7 and NK9) were taken with the microwave power set in the range 7.90 mW to 7.94 mW as this power range allowed for the most satisfactory tuning of the cavity for the entire temperature range. The carbon nanosphere samples were in powder form and were loaded into NMR tubes made out of Pyrex which is a type of borosilicate glass that is resistant to heat and chemicals.

Phase sensitive detection scheme was used for all measurements; modulation amplitude of 2 Gauss at 100 KHz and 15 dB of attenuation were used and kept constant. The magnetic field strength between two large and water cooled magnets were monitored by Hall probe attached on it throughout the experiment. The operation and components of Bruker ESR spectrometer are described in Appendix.

The linewidth ΔH, peak-to-peak amplitude ΔM, and asymmetry ratio A/B of first derivative of absorption line were investigated and analyzed in the temperature range 5- 320 K.

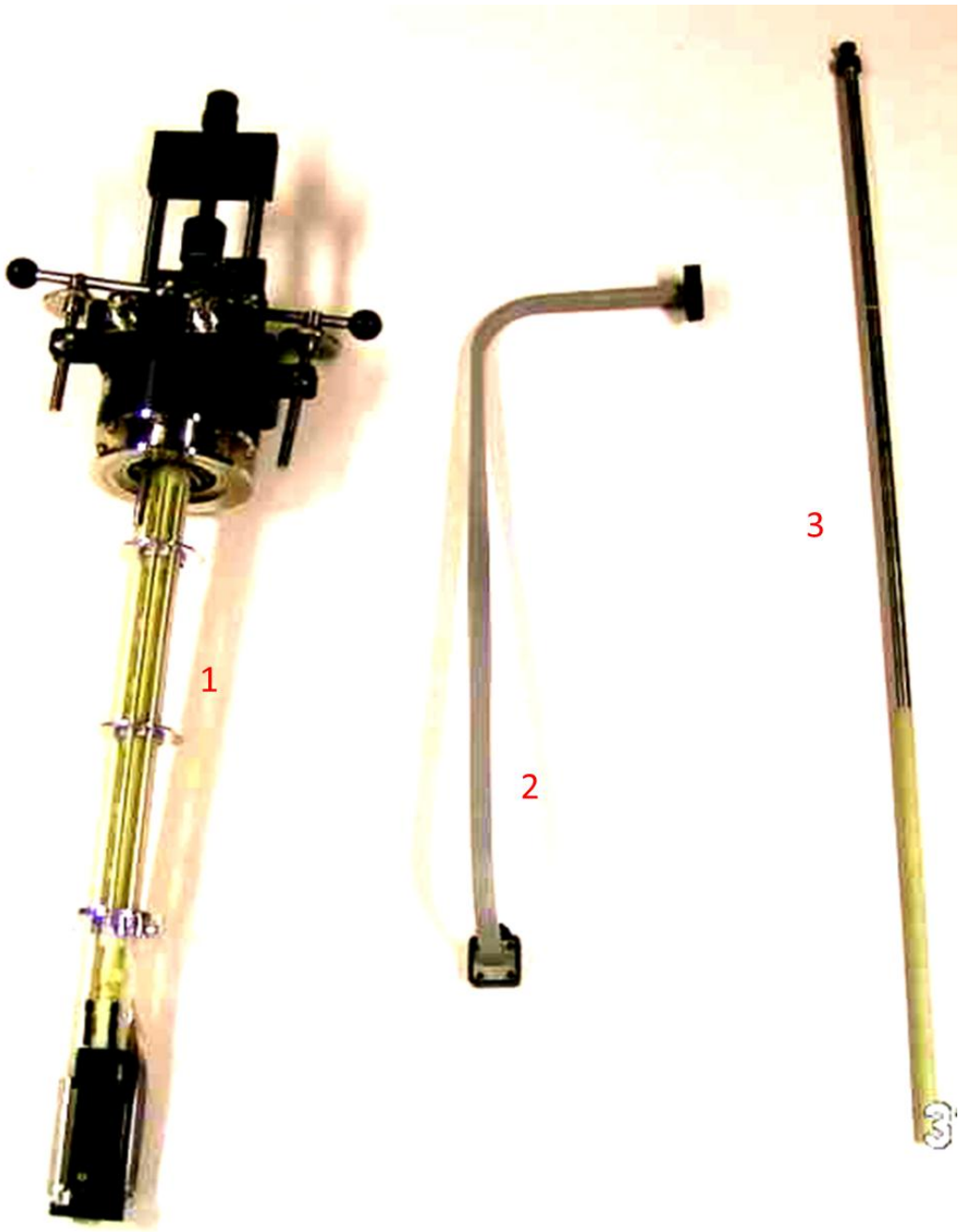

Figure 4.2.1 ER4118CF cryostat (1) has cavity mounted inside it, waveguide (2) leading connecting to a detector, and sample rod (3).

4.2.2 Room temperature measurements

ESR measurements were done at room temperature using Bruker ESP300E operating in the frequency range 9.4-9.9GHz. All the ESR measurements were performed with ESR spectrometer operating in continuous wave mode with universal standard probe in Figure 4.2.2

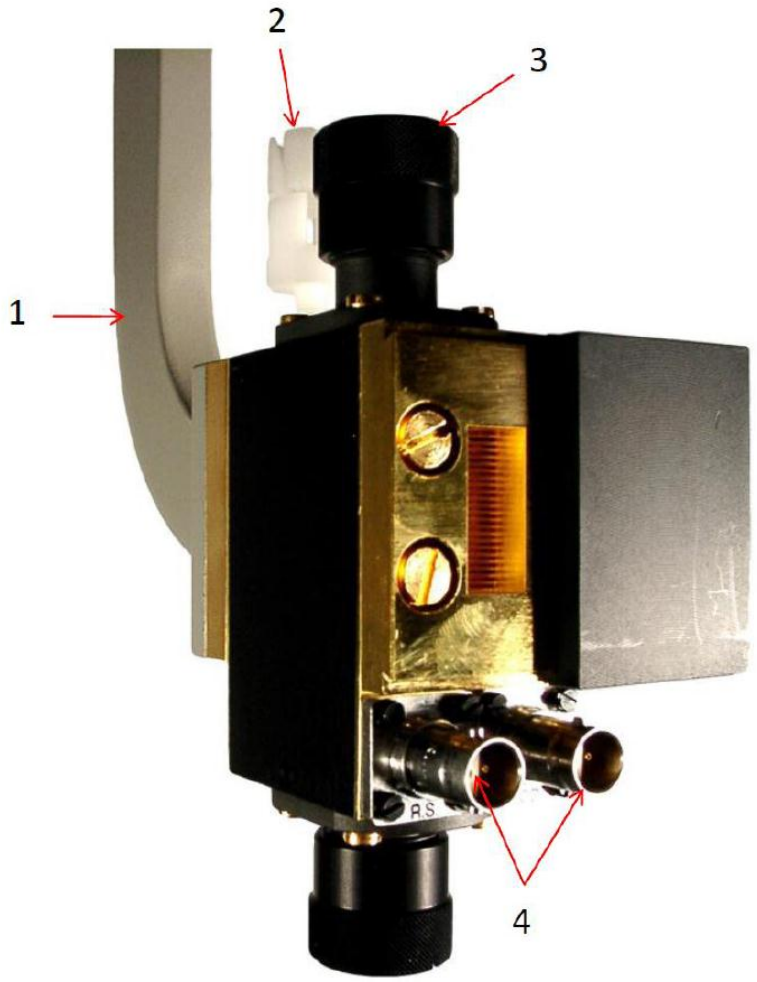

Figure 4.2.2 Universal X-band resonator has rectangular waveguide (1), iris (2), sample chamber (3), and connection sockets (4).

Polycrystalline 2,2-diphenyl-1-dicrylhydrazyl(DPPH) reference samples were employed to determine the spin concentrations of nitrogen source and the relative g-factors in the samples. The quantity of the DPPH sample used was varied depending on the magnitude of resonance spectrum produced by carbon nanospheres under investigation. All the ESR measurements were obtained using phase-sensitive detection, and the ESR spectra shown later are the first derivative of the absorption spectrum. Standard power saturation measurements were performed on all samples, in order to estimate length of relaxation times: spin-spin and spin-lattice relaxation times. Small samples are necessary for ESR measurements, as it becomes impossible to tune the microwave cavity. In addition, tuning was done for each sample investigated since changing a sample results in de-tuning of the microwave cavity.

References

1. Kunjuzwa N., *N-doping of the Carbon Spheres and the Synthesis of Polythiophene/Carbon Sphere Composites,* MSc Thesis, University of the Witwatersrand, Johannesburg, 2009.
2. Iyuke S. E., Danna A. B. M., *Micropo. Mesopo. Mater*. **84**, 338-342 (2005).

CHAPTER 5

RESULTS AND DISCUSSION

This project aim to investigate the spin dynamics and further report the properties of the carbon nanospheres investigated using continuous-wave ESR spectrometer at room [1] and low temperatures [2]. The characterization are mainly based on the analysis of resonance lineshape using theoretical models discovered by Dyson and later reviewed by Feher and Kip [3, 4]; while low temperature measurements investigate the magnetic properties through variation of resonance parameters such as peak-to-peak linewidth, asymmetry ratio and amplitude.

Paramagnetic centres

According to Joseph Joly *et al.* [5], an arbitrary shaped graphite cluster could be ferromagnetic or anti-ferromagnetic if their non-bonding π-electron spins at the zigzag edges are aligned parallel or anti-parallel to each other as shown in Figure 5.1. These paramagnetic centres usually result from structural disorder and can be described as quasi-localized spins, since they can obey Curie-type and Pauli-type paramagnetism at low and high temperature, respectively [6]. Whereas localized paramagnetic electrons induced by nitrogen addition exhibit narrow ESR spectra, quasi-localized spins exhibit broader ESR spectra. Since localized spins were induced through addition of small amount of nitrogen onto graphitic lattice, the concentration of localized spins should be low in comparison with quasi-localized spins and even lower than carriers (delocalized π-electrons of the host material). Carriers produce very broad ESR spectra known as conduction electron spin resonance (CESR). Although ESR signals of these paramagnetic centers are different in width, the properties of resulting ESR spectrum could be quantify through relative magnetic susceptibility [7,8] of localized χ_d and carrier spins χ_s as follows,

$$\chi_r = \frac{\chi_d}{\chi_s}.$$

For the case $\chi_r \ll 1$ the properties of conduction electrons (carriers) will dominate the ESR spectrum and therefore signal of localized paramagnetic electrons will behave in the same manner as CESR, i.e. their intensity will demonstrate the Pauli-type paramagnetism. In the case $\chi_r > 1$ the ESR spectrum will be determined by the properties of localized paramagnetic centres, i.e. Curie-type paramagnetism.

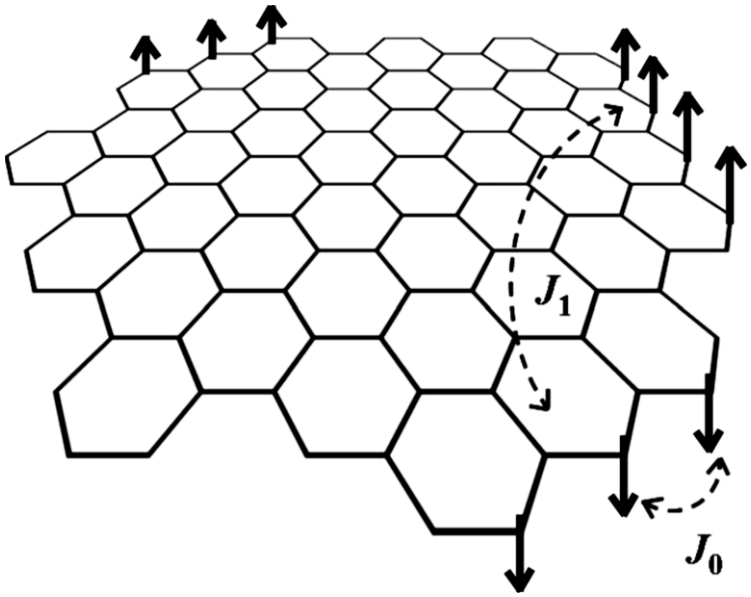

Figure 5.1 Joseph Joly V. L. *et al.* [5] described a model structure of an arbitrary- shaped of graphene cluster above. The zigzag localized spins oriented parallel or anti-parallel to each other, and thus resulting in ferromagnetically or anti-ferromagnetically ordering, respectively. When the coupling involves an opposite localized spins separated by a number of hexagonal rings, the ferromagnetic or anti-ferromagnetic ordering is represented by $\boldsymbol{J_1}$, and the ferromagnetic ordering of nearby spins is represented by $\boldsymbol{J_0}$.

In addition, different nitrogen paramagnetic centers can occur anywhere around an arbitrary shaped cluster. Quasi-localized spins or non-bonding zigzag edge states are theoretical considered to lie close to the Fermi level[9,10,11], whereas some N paramagnetic centers such as graphitic-like nitrogen($N_{3\pi}$) could be located just below conduction band (π^*-states)as a donor level[12]. Hence, the intrinsic and nitrogen

paramagnetic centers could be thought to have different creation energy and resonance frequency. Moreover, it is important that one investigate the interactions of these paramagnetic electrons which have different behavior and origins as well as their interaction with the lattice.

5.1 ROOM TEMPERATURE RESULTS

5.1.1 Sample characterization

The carbon nanospheres (CNS) used for this research are produced from the vertical and horizontal reactor. Since the CNS were also produced from different precursors which were used as nitrogen and carbon source, the search of CNS with larger fraction of nitrogen occupying the substitutional sites were undertaken. The carbon nanospheres produced contained different concentration of nitrogen and have different magnitude of linewidth, amplitude and g-shift as shown in Table 5.1.1.1 and Figure 5.1.1.1[2]. Hence, the different resonant parameters could be closely associated with different structural features and nature of paramagnetic electrons.

NK3 has very large amplitude in comparisons to NK2 and NK4, while NK1 has intermediate amplitude. The nitrogen addition in carbon nanospheres produced from horizontal reactor have linewidth and Dysonian line-shape that are increasing with nitrogen content as shown in Figure 5.1.2.1. Moreover, the horizontal reactor produced CNS are many orders of magnitude narrower than the CNS produced from vertical reactor (see Table 5.1.1.1).

Table 5.1.1.1 Different values of resonance linewidth (ΔB) and relative g-shift (Δg) represent different N-doped carbon nanospheres. The (Δg) of carbon nanospheres was measured through noting the resonance field difference between DPPH and carbon nanosphere spectrum shown in Figure 5.1.2.2.

	NK1	NK2	NK3	NK4	NK5
ΔB (G)	9.5 ± 0.5	5.0 ± 0.2	3.2 ± 0.1	1.8 ± 0.1	2.4 ± 0.2
Δg (%)	1.5 ± 0.5	$- 3.4 \pm 0.1$	$- 1.4 \pm 0.1$	$- 1.4 \pm 0.1$	$- 1.1 \pm 0.1$
	NK6	NK7	NK8	NK9	
ΔB (G)	1.36 ± 0.01	0.57 ± 0.01	12.5 ± 0.5	1.14 ± 0.01	
Δg (%)	$- 5.09 \pm 0.02$	$- 1.5 \pm 0.02$	$- 8 \pm 1$	$- 5.24 \pm 0.02$	

The resonance line of NK2 clearly revealed the broad spectral components (shown in Figure 5.1.1.1) which are buried by the narrow spectra in other samples produced from same reactor. The broad component of the spectrum was attributed to delocalized electrons which are intrinsic in graphitic carbons, while narrow component confirms the presence of nitrogen paramagnetic centres. The ESR parameters compared in Table 5.1.1.1 are for paramagnetic signals and are: relative g-shifts, amplitude and linewidth for spectra shown in Figure 5.1.1.1 and Figure 5.1.1.2.

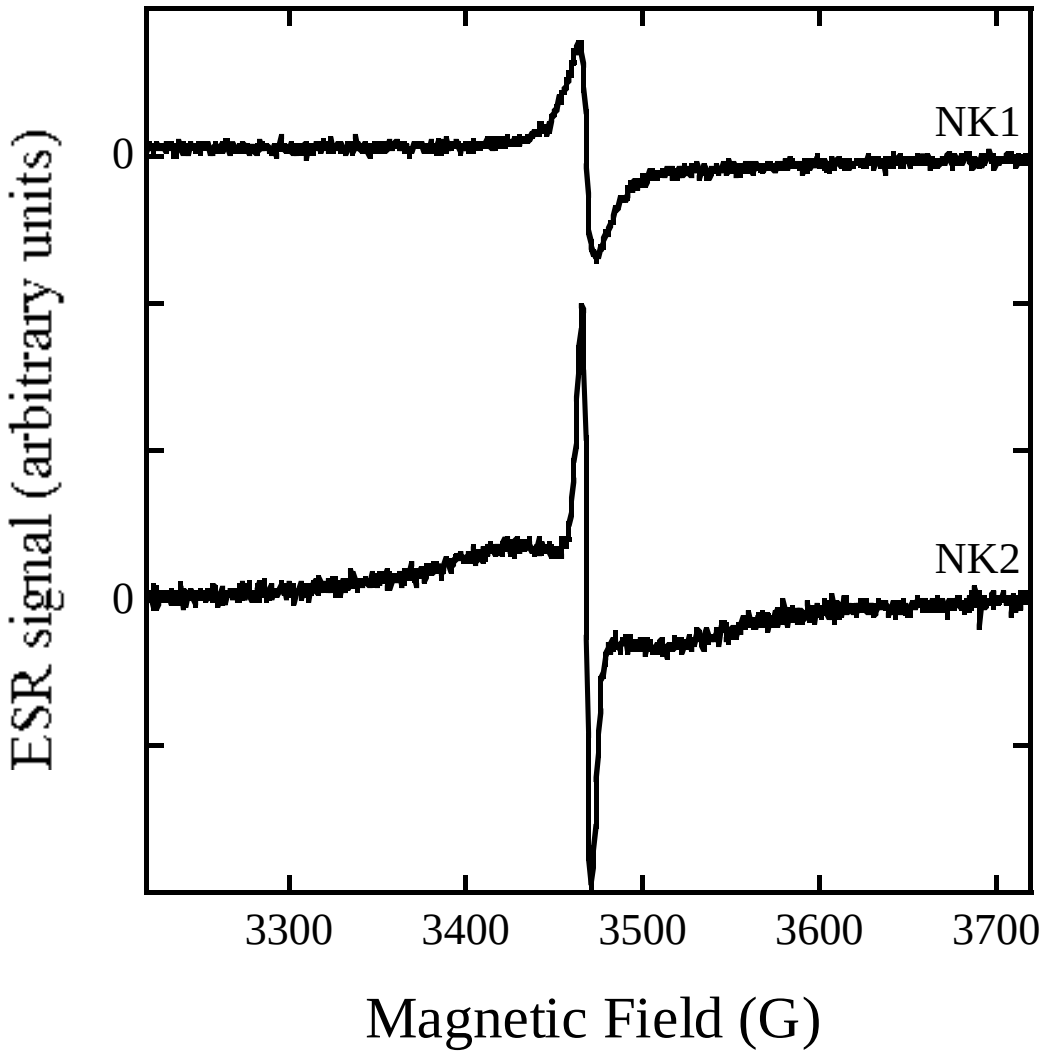

Figure 5.1.1.1 A comparison of spectra corresponding to pristine (NK1) and N-doped (NK2) carbon nanospheres. NK2 consists of two spectra, broad and narrow, assigned to carriers and localized electrons (nitrogen paramagnetic ions), respectively. These samples were prepared in the vertical reactor (see Table 5.1.1.1).

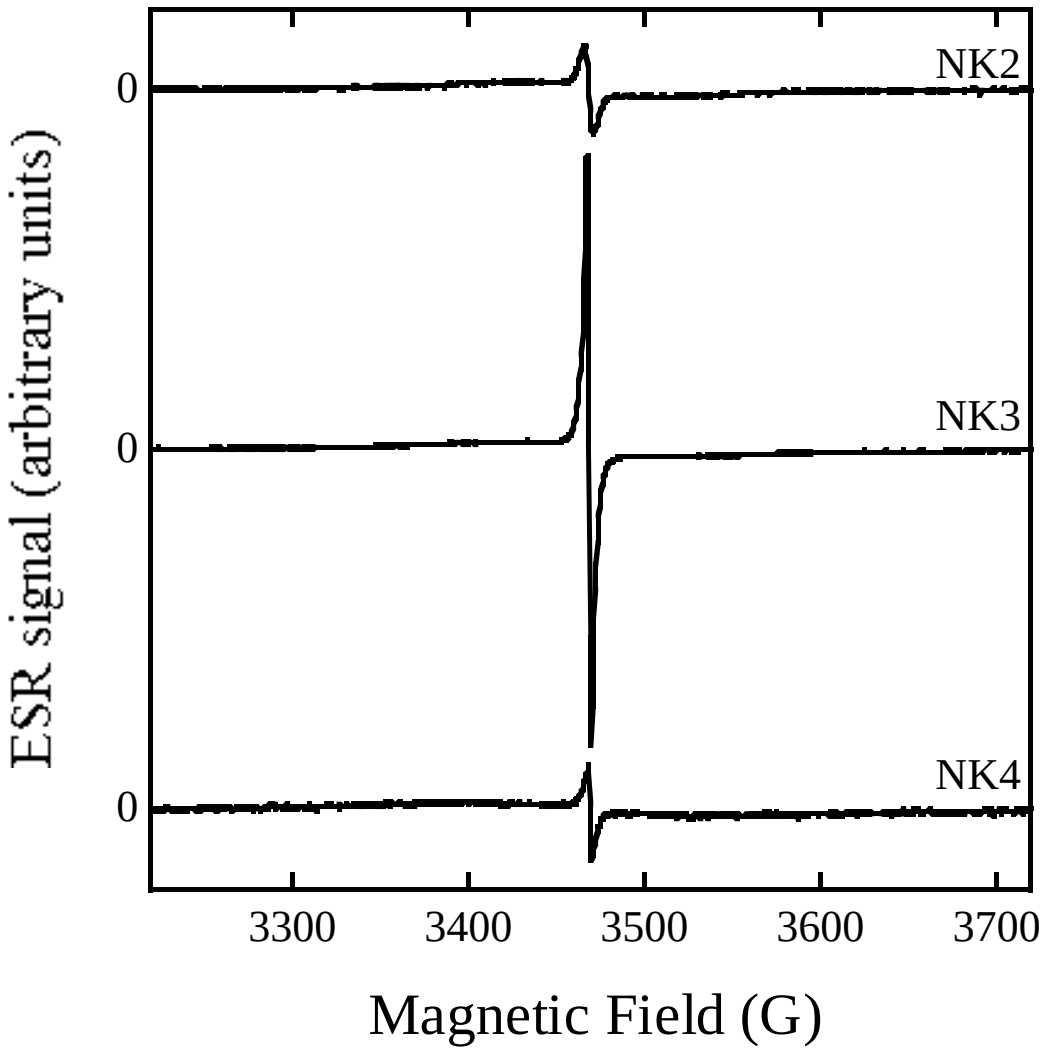

Figure 5.1.1.2 A comparison of the carbon nanospheres with different N concentration using resonance spectra. These samples were prepared in the vertical reactor (see Table 5.1.1.1).

5.1.2 Concentration of N Paramagnetic centres

The nitrogen content was obtained from elemental analysis measurements conducted by the Institute for Soil, Climate and Water, Pretoria, South Africa. Keartland *et al*. [1], estimated the relative and absolute concentration of nitrogen through comparison with respect to NK6 and polycrystalline DPPH sample, respectively. Detailed investigation of N paramagnetic centres was done on samples from the horizontal reactor as shown in Table 5.1.2.1.

Table 5.1.2.1 A comparison of the concentration of N paramagnetic centers in carbon nanospheres produced from horizontal reactors. The estimations of paramagnetic centres were done using different techniques explained above. Error estimates are not included in these measurements.

Sample	Elemental analysis (%)	Relative concentration (%)	Absolute concentration(%)
NK6	5.00	100	3.2
NK9	3.52	16.2	0.55
NK7	1.48	8.4	0.3

An attempt was made to determine the relative nitrogen concentration, and the spin concentration relative to a reference sample (DPPH) for NK6, NK7 and NK9. The mass of each of the samples (NK6, NK7 and NK9) was carefully measured with digital mass balance. Due to small masses involved (<10 mg) in resonance measurements, the mass determination has large inherent errors (~20 %).The double integral of the resonant spectrum obtain for each sample was normalized to the mass and compared. The results are tabulated in Table 5.1.2.1, together with the results of elemental analysis for these samples. The resonance measurements are in qualitative agreement with the elemental analysis for all samples. However, samples NK6, NK7 and NK9 have spectra hinting carrier spins, the measurements should be able to discriminate between the carrier and localized spins. On the other hand the CNS are in powder form, hence one cannot easily discriminate between the two spectra by

simply changing the applied magnetic field direction. The paramagnetic ions could be accurately estimated by subtraction of carrier spins measured using electrical transport techniques. The carrier spins concentration could be then subtracted from an overall spectrum, and the net results could be paramagnetic ions concentration.

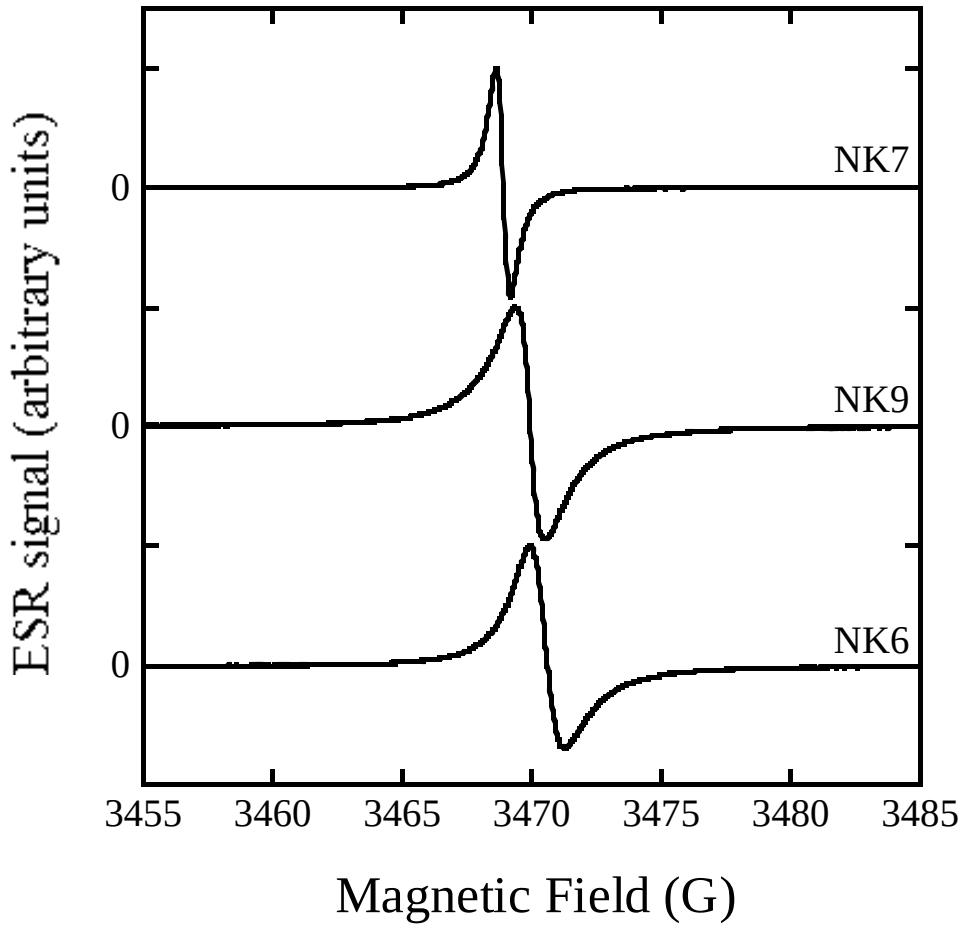

Figure 5.1.2.1 A comparison of the resonance spectra (ESR) for the nitrogen-doped carbon nanospheres produced in horizontal reactor. As the nitrogen content increases the spectrum of CNS becomes broader and progressively more Dysonian in character. However, these CNS are more than two orders of magnitude smaller than the sample labelled NK3. Shifts in the resonance field from sample to sample are due to retuning of the microwave cavity, rather than true g–shifts.

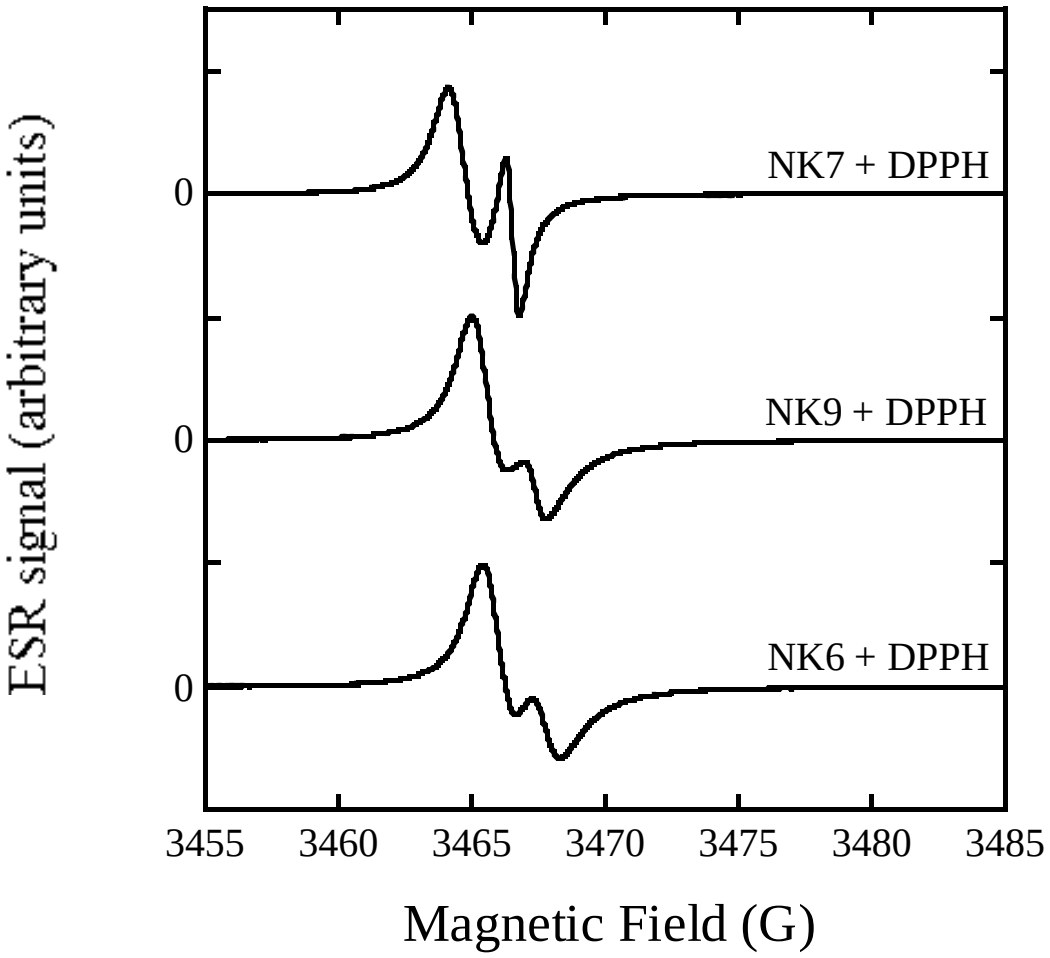

Figure 5.1.2.2 A comparison of the ESR spectra for the composite samples of the DPPH reference and the three nitrogen-doped samples produced in the horizontal reactor. Shifts from the resonant fields in comparison with Figure 5.1.2.1 are due to re-tuning of the microwave cavity following changing the sample. The relative g-shifts given in Table 5.1.1.1 were deduced from composite spectra such as these.

5.1.3 Microwave Power measurements

Since the low temperature ESR measurements were all taken at constant microwave power, it is important to carefully look at the implications of microwave power. The amplitude of the ESR spectrum depends on the gyromagnetic ratio γ, the amplitude of the perturbing microwave magnetic field B_1, the spin-spin relaxation time T_2 and spin-lattice relaxation time T_1[13].

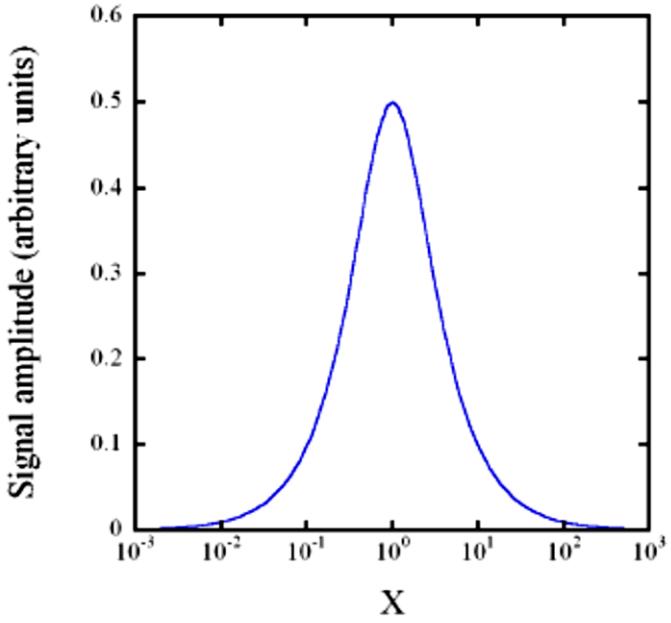

Figure 5.1.3.1 A schematic of theoretical power saturation curve for a homogeneously broadened resonance line [13]. The parameter X depends on the microwave power and the relaxation times of the spin system as defined in (5.1.3.1).

For homogeneously broadened resonance spectra the resonance amplitude ΔM may be written in the form

$$\Delta M(T) \propto \frac{X}{1+X^2}, \qquad (5.1.3.1)$$

where $X = \gamma B_1 \sqrt{T_1 T_2}$. A plot of the resonance line amplitude as a function of X is shown in Figure 5.1.3.1 and Figure 5.3.2.2 in log and linear scale, respectively. For resonance measurements where microwave power B_1 is kept constant we can two scenarios:

Cases I: **Homogeneous broadening**

In this case changes in temperature causes negligible spin-spin interactions and therefore changes in signal amplitude are associated with spin-lattice relaxation time T_1 as follows,

$$\Delta M(T) = M_0 \frac{A\sqrt{T_1}}{1+A^2 T_1}, \qquad (5.1.3.2)$$

where M_0 and A are parameters that depend on the experimental arrangement. Spin-lattice relaxation T_1 is temperature dependent. The homogeneous broadening is probably due to dipolar interaction between like spins, spin-lattice relaxation time, carrier electrons in a microwave power, diffusion of excitation throughout the sample and motionally narrowed fluctuations in the local field.

Case II: **Inhomogeneous broadening**

Inhomogeneously broadened line consists of a spectral distribution of overlapping resonant spectra merged into a single resonant line. Sources of inhomogeneous broadening could include hyperfine coupling, unresolved fine structure and dipolar interaction between spins with different Larmor frequencies. Castner *at al*. [13] expressed the resonant amplitude of an inhomogeneous broadening line as follows:

$$\Delta M(T) \cong \frac{X}{(1+X^2)^{1/2}} . \qquad (5.1.3.3)$$

Power saturation results to a constant resonant amplitude which occurs when X>>1.

Changes of Amplitude with Power

Both samples have amplitudes that change with microwave power in qualitatively the same fashion; their amplitudes are almost linear at low power as shown in Figure 5.1.3.3. However, the amplitudes of these samples behave differently at high microwave power; the amplitude of NK7 shows a hint of saturation as one approaches high power, while the amplitude of NK9 diverges. Both samples do not follow the theoretical curve (shown in Figure 5.1.3.2) which describes the changes of amplitude with microwave power when homogeneous spin system is assumed; NK7 and NK9 do not saturate at high powers. However, the theoretical curve fit [relation (5.1.3.3)] assuming inhomogeneous broadening of a line approximates the experimental results of NK7 and NK9 closely, as shown with fits in Figure 5.1.3.3. The inhomogeneity of the spin system is apparent for both samples; they could consists of different paramagnetic ions (nitrogen induced and intrinsic paramagnetic ions could have different chemical environments), as well as extrinsic and intrinsic carriers which may be precessing about different axes.

The delayed saturation of the ESR amplitude of both samples with power suggests a very short spin-lattice relaxation time, shorter than 10^{-6} s [14], due to curvature enhanced spin-orbit coupling. The relative concentration of nitrogen in NK7 is almost half the concentration of NK9 as shown in Table 5.1.2.1, hence the larger delay of NK9 amplitude from saturation could be attributed to larger spin-orbit coupling associated with larger content of nitrogen [15]. Obviously, the spin relaxation times of these two samples are different; following Pines and Slichter [15] one can get an estimated spin lattice relaxation time as follows:

$$1/T_1 \sim (\lambda^2/\hbar^2)(a/v)f, \qquad (5.1.3.4)$$

where λ is the spin-orbit coupling, *f* the concentration of impurity atoms, *v* the speed of electron and *the* unit cell dimension. Spin-lattice relaxation time T_1 equals T_2 for

conduction electrons; T_2 is the inverse of resonance linewidth [16, 17]. The lack of amplitude power saturation made estimation of relaxation times impossible and could be measured with pulse mode ESR.

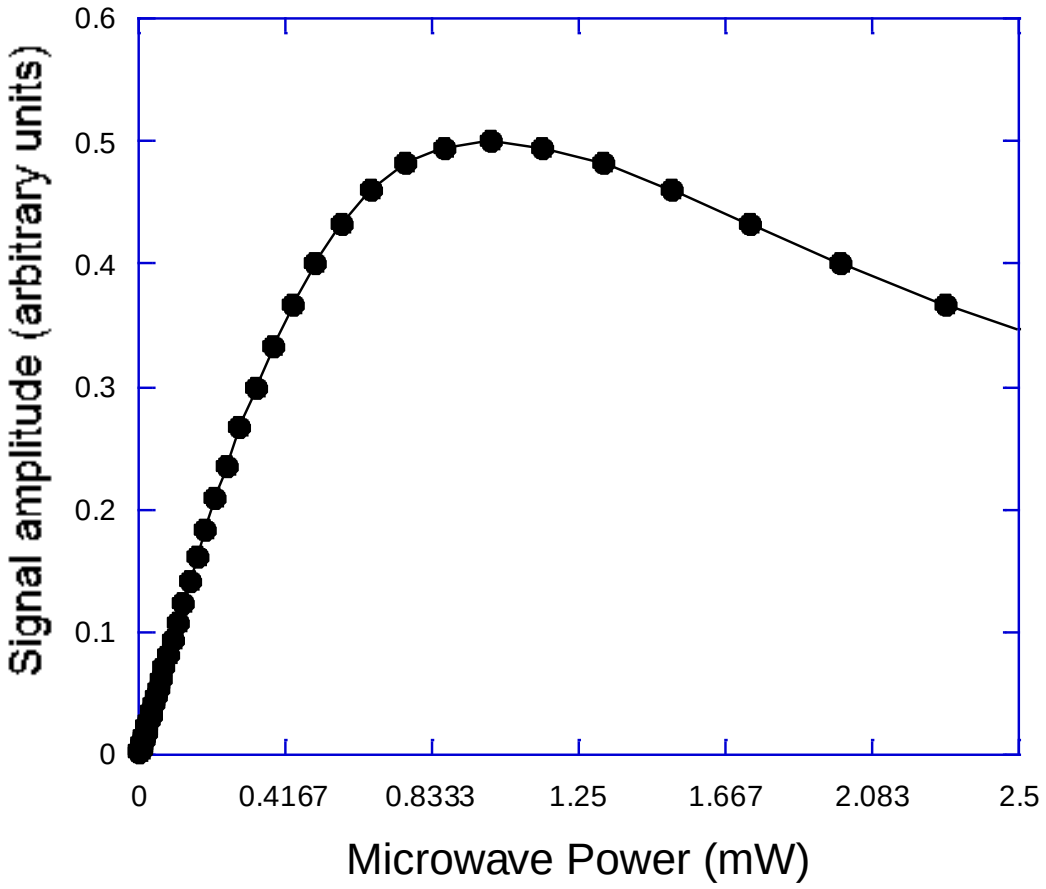

Figure 5.1.3.2 A best fit (solid line) to experimental (solid dots) data of polycrystalline pellet of ammonium tartrate irradiated with a dose of 1 kGy. The amplitude saturates at high microwave power for this homogeneous spin system [13].

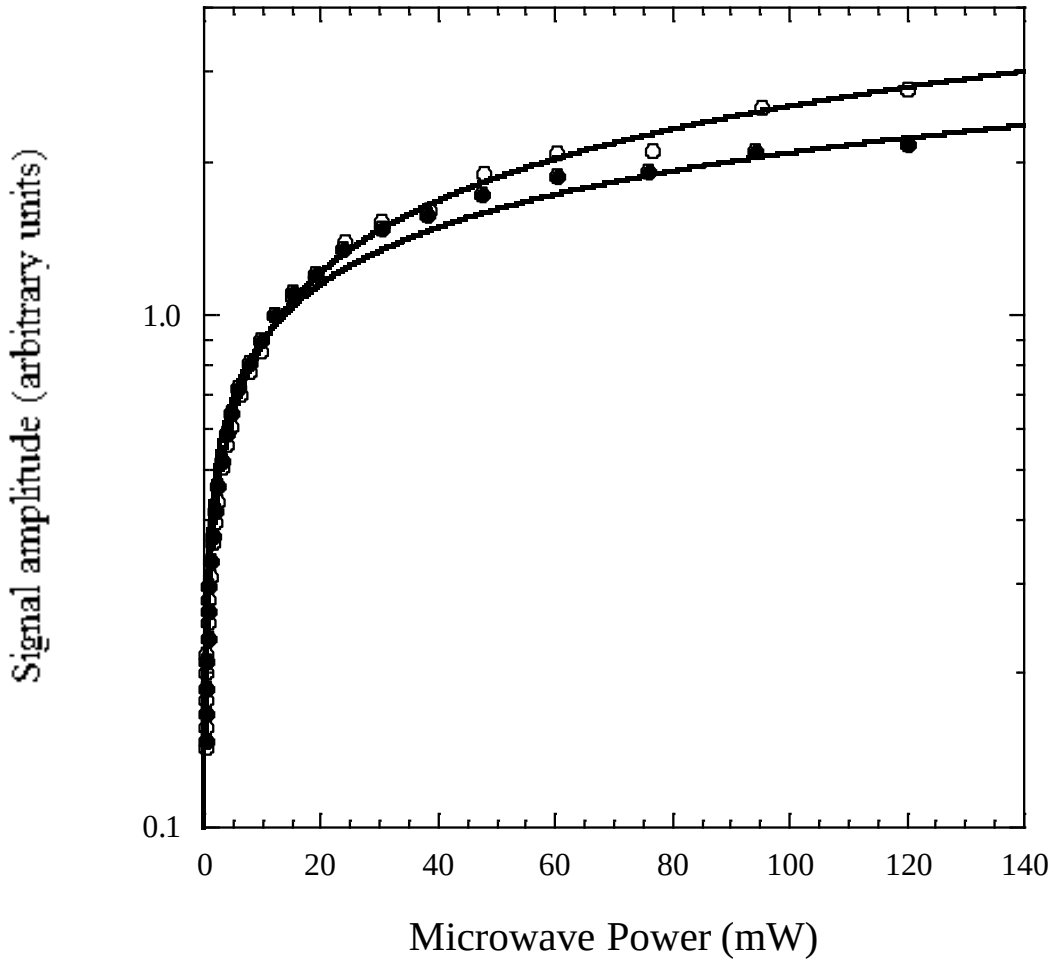

Figure 5.1.3.3 A variation of amplitude with microwave power for two samples NK7 (solid dots) and NK9 (open dots). Solid lines are theoretical curve fit [relation (5.1.3.3)] for resonant lines that are inhomogeneously broadened [13].The curve fit on NK9 approximates the experimental data points quite well than it does on NK7. Experimental data point of NK7 suggests a very slow approach to saturation while amplitude of NK9 diverges.

Resonance lineshape Analysis at Room temperature

Spectra of samples labeled NK1, NK2, NK3 and NK4 are shown in Figure 5.1.1.1 and Figure 5.1.1.2; NK3 has larger paramagnetic signal in comparison to NK2 and NK4 samples. This is in agreement with the concentration of nitrogen (% N) estimated with elemental analysis; NK3 has the highest %N in comparison to concentration of % N in NK2 and NK4 as shown in Table 5.1.1.1. In addition, these samples have very broad resonant lines as background in common. Since the broad signals (CESR spectrum) were many orders of magnitude smaller than paramagnetic signals, the spectra measured were mainly originates from localized paramagnetic electrons.

The very poor detection, except on the spectrum of NK2, of broad spectral components could be attributed to carriers experiencing the non-negligible spin-orbit coupling which is enhanced by curvature of nanographite layer [18]. The coexistence of decoupled carrier and localized spectrum in NK2 suggests a spin relaxation mechanism dominated by Korringa- like relation [16]. Therefore NK2 can be hardly considered magnetic due to weak exchange interaction between carrier and localized spins. The narrow linewidth of NK4 suggest long spin relaxation time (spin dephasing time T_2 or spin-lattice relaxation time T_1) since linewidth narrows with increasing spin relaxation time. Unfortunately, the nature of spin relaxation can only be deduced over a range of temperature; resonance linewidth drawn as a function of temperature describes the nature of spin interactions and spin dynamics.

Samples NK7 and NK9 were further investigated over the temperature range 5- 320 K. The spectra of the samples get more Dysonian in shape as their nitrogen content increases as shown in Figure 5.1.2.1; hence their spin relaxation is governed by spin diffusion time T_D if the condition, $T_D \ll T_2$ is satisfied[3, 4]. The increasing Dysonian lineshape of spectra suggests an increasing electrical conductivity σ due to increasing carrier density associated with N induced defects [20], and thus a reduction of the

skin depth δ. One can express the relationship between diffusion time and electrical conductivity as follows:

$$T_D = 3/4\pi f\sigma v_F \Lambda, \qquad (5.1.3.5)$$

where f is the frequency of the oscillating magnetic field, Λ the mean free path, and v_F the Fermi velocity.

5.2 LOW TEMPERATURE RESULTS

5.2.1 Amplitude

The peak-to-peak amplitude for the derivative curves of the ESR lines was obtained for each spectrum. The results for the entire temperature range studied for NK7 and NK9 are given in Figure 5.2.1.1 and Figure 5.2.1.2 respectively. The samples show similar behavior as the temperature decreases. Between 320 K and approximately 200 K the size of the signal decreases markedly (by a factor of approximately 4 in both samples). Between 200 K and lower temperatures approximately 120 K and 25 K (for NK9 and NK9, respectively) the signal amplitude of both sample is essentially constant. The signal amplitude increasing markedly as the samples were further cooled down to lowest temperature around 5 K (a factor of approximately 6 for NK7, and a factor of approximately 12 for NK9). At low temperatures (between 5 K and approximately 60 K) the changes in signal amplitude follows the Curie law (1/T), which is identical to the predicted Boltzmann factor dependence and the fit, is given as

$$\Delta M(T) = A + B_z/T \qquad (5.2.1.1)$$

where the data in this temperature regime, and the results of the fit are given in Table 5.2.1.1. The ratio of B_Z for the two samples should provide reasonable estimates of the concentration of the paramagnetic ions in each of these samples.

Table 5.2.1.1 A comparison of fitting parameters resulted from Boltzmann prediction model corresponding to NK7 and NK9 [2].

Sample	A	B_z
NK7	0.34 ± 0.09	28 ± 1
NK9	0.67 ± 0.21	54 ± 1

The concentration of nitrogen in NK7 were found to be approximately half that of the concentration in NK9. This is in excellent agreement with careful ESR measurements made at room temperature for both samples.

At high temperature limit, the rise in amplitude could be attributed to Orbach process as described by relation (5.2.1.2),

$$M(T) = \frac{1}{A_O[\exp(\Delta/k_B T)-1]}\,. \qquad (5.2.1.2)$$

In addition, other phonon- driven spin relaxation mechanisms such as direct and Raman process could also contribute in the range of temperature investigated as shown below,

$$1/T_1 = T/A_D + T^7/A_R + 1/\{A_O[\exp(\Delta/k_B T) - 1]\}, \qquad (5.2.1.3)$$

where A_D, A_R, A_O and Δ are determined from fits to the experimental data as shown in Table 5.2.1.2.

The changes of the amplitude with temperature were deduced from relation (5.1.3.3) taken at constant power and constant spin-spin relaxation time. The relation (5.2.1.2) and (5.2.1.4) were substituted in (5.1.3.3) to describe the changes in amplitude at low and high temperatures. However, if the first two terms in (5.2.1.3) are negligible, the

spin relaxation would be governed by Orbach process at high temperatures. Since the Orbach relaxation rate has an exponential term in the denominator, for the activation energy Δ that is required the -1 in the denominator can be ignored, and the Arrhenius expression is obtained.

Table 5.2.1.2 Parameters for the lattice vibration contributions to the spin-lattice relaxation times whose contribution were deduced from simulations of the experiment. The model changes strongly with values of Δ, but changes due to other parameters are negligible.

A_D (s.K^{-1})	A_R (s.K^{-7})	A_O (s)	Δ (eV)
3	10^{10}	10^{-7}	0.301

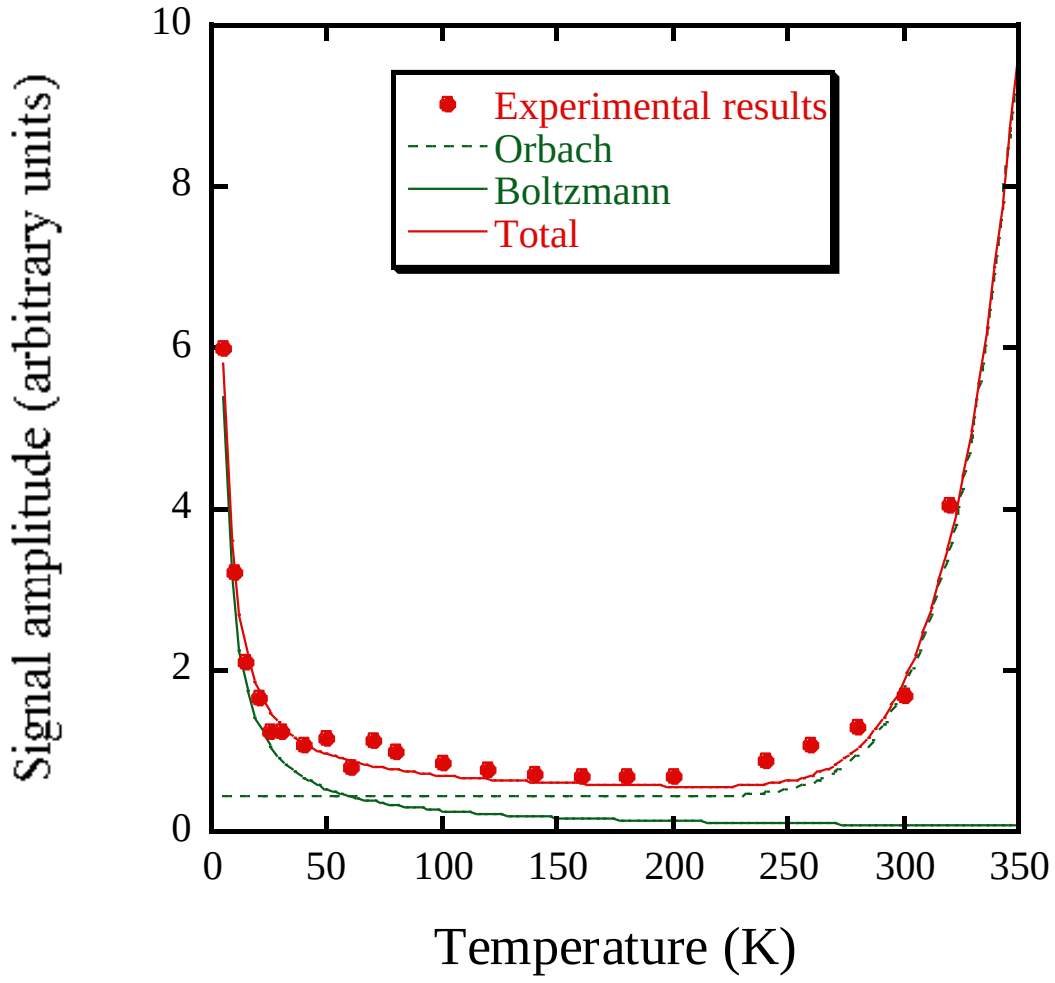

Figure 5.2.1.1 Temperature dependence of the signal amplitude for sample NK7. The observed variation of the signal amplitude with temperature is described by lattice vibration model. Boltzmann prediction and Orbach process describe changes at low and high temperatures, respectively. However, a model based on nanographites network seem to provide an alternative to the changes in amplitude.

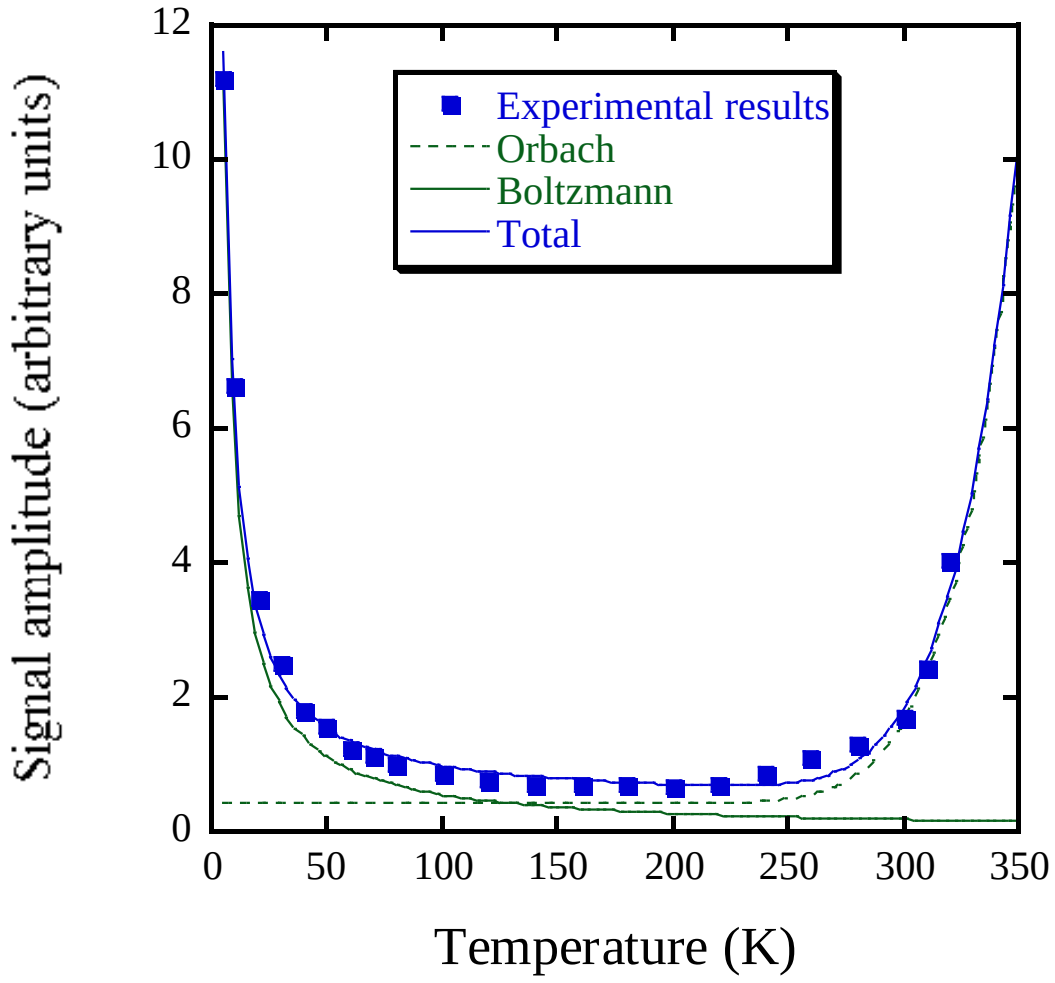

Figure 5.2.1.2 Temperature dependence of the signal amplitude for sample NK9. The observed variation of the signal amplitude with temperature is described by lattice vibration model. Boltzmann prediction and Orbach process describe changes in amplitude at low and high temperatures, respectively. However, a model based on nanographite assembly seems to provide an alternative approach.

The rise in amplitude due to phonon driven relaxation process is however debatable below 250K. Hence, other relaxation mechanism with the nearly the same mathematical expression as Orbach could be responsible. An alternative to Orbach

process could be thermal activation of carrier electrons to an energy level $\Delta = 0.30$ eV above the Fermi level, this results in relaxation of the paramagnetic ions via interaction with carriers. This energy level could be associated with energy gap in the conduction band; however detailed knowledge of the electronic structure is required to support this conjecture.

5.2.2 Lineshape and Asymmetry ratio

The asymmetry ratio A/B of ESR spectra changes with temperature in a manner shown in Figure 5.2.2.1 and Figure 5.2.2.2 for NK9 and NK7, respectively. Dyson *et al.* [3], in the course of studying the resonance spectra with different shape parameters (the ratio of the peak amplitudes A/B and the peak-to-peak linewidth ΔB) had analyzed the relations between the time required for a carrier spin to diffuse across the skin depth T_D and time T_2, which is proportional to the inverse linewidth (and equal to T_1 – the spin–lattice relaxation time).

At low temperatures, the ratio of NK9 has values between about 1.2 and 1.4 (marked by solid horizontal line in Figure 5.2.2.1) and this hints larger concentration of localized spins (paramagnetic electrons in localized region) in comparison to carrier spins. Asymmetry ratios between 3 and 9 are associated with highly conductive materials, while a ratio close to 1 is associated with localized electrons, and thus corresponds to poor electrical conductivity [3, 4]. However above 1.4, which is just above 240 K, the ratio of NK9 increases at higher rate to higher values; a value of about 2.3 is reached at 320 K. Therefore the electrical conductivity of the carbon nanospheres could be thermally enhanced as temperature increases and is evidence by Dysonian lineshape of NK9 spectrum high temperatures investigated. Thermal enhanced paramagnetic electrons could be localized and conduct by hopping in localized region although further work would be needed to explore this point in details.

The NK7 has asymmetry ratio far below 1.4 for almost in the whole range of temperature investigated; this ratio is increasing slowly and almost linearly with temperature (shown with straight line in a figure). Hence, NK7 contain larger percentage of paramagnetic electrons in localized regions. Resonance amplitude ΔM used for this work is basically peak-to-peak amplitude (A+B); where A is positive and B negative lobe of the amplitude (shown in Figure 3.8.1), respectively.

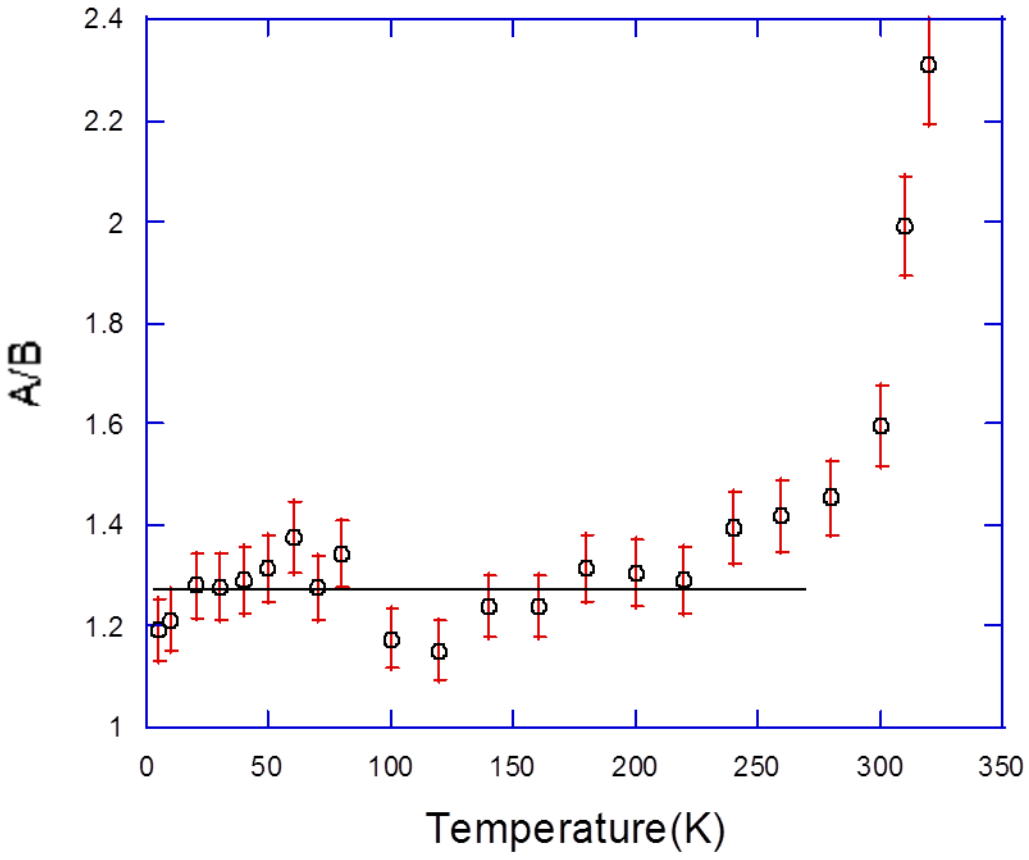

Figure 5.2.2.1 Asymmetry ratio A/B of NK9 increases with temperature. An obvious increase of the ratio is seen above 220 K, while below 220 K the ratio is almost constant. The increase of A/B parameter is closely associated with thermal enhanced conduction carrier density.

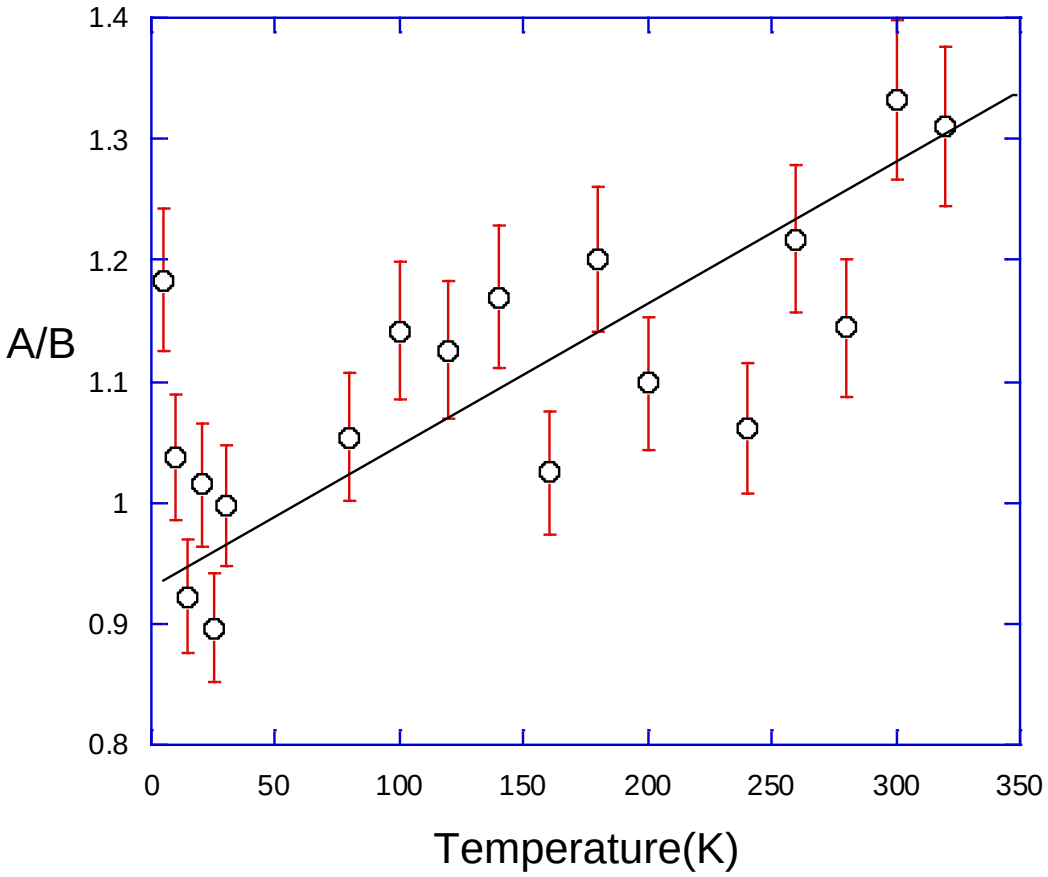

Figure 5.2.2.2 Asymmetry ratio A/B of NK7 varies randomly with temperature. Solid straight line shows a slowly increase of the ratio with changing temperature. The random fluctuation of A/B parameter could be thought to come from different nitrogen paramagnetic ions (that could include intrinsic paramagnetic ions) which could be exchanging energy with a smaller fraction of conducting carrier spins.

5.2.3 The resonance linewidth and relaxation

The linewidth of NK9 changes with temperature in a rather strange manner (Figure 5.2.3.1); it has plateaus in different ranges of temperatures (temperature independent linewidth with discrete values: 0.70 G, 0.85 G, 1.0 G and 1.37 G) and also increases with temperature above 140 K. This strange behaviour of the changes of linewidth needs thoroughly investigation before one could simply assign this to experimental errors. Above 140 K, the linewidth changes almost periodically with temperatures about an equilibrium line (long horizontal line at high temperature data points). The linewidth has a value of about 1.73 G and 1.67 G at 300 K and 320 K, respectively.

In Figure 5.2.3.2 the linewidth of NK7 hints a dome-shaped anomaly centered around 15 K (pointed by arrow). The signal amplitude measurements did not reveal any irregularities around this temperature range, and thus could be attributed to experimental error. The confirmation of this anomaly could be perhaps justified by magnetic susceptibility measurements. Above 30 K the linewidth of NK7 increases almost linearly with temperature up to about 180 K and this could be associated with lifetime broadening. Further than this temperature, the linewidth narrows from a maximum value of about 1.48 G to a value close to 1.12 G at 240 K and confirms thermally added electron spins. The linewidth above 240 K is temperature independent up to 320 K, and the linewidth has a constant value of approximately 1.2 G. This constant linewidth in the temperature range 240 – 320 K forbids any dipole-dipole or exchange interaction between electrons.

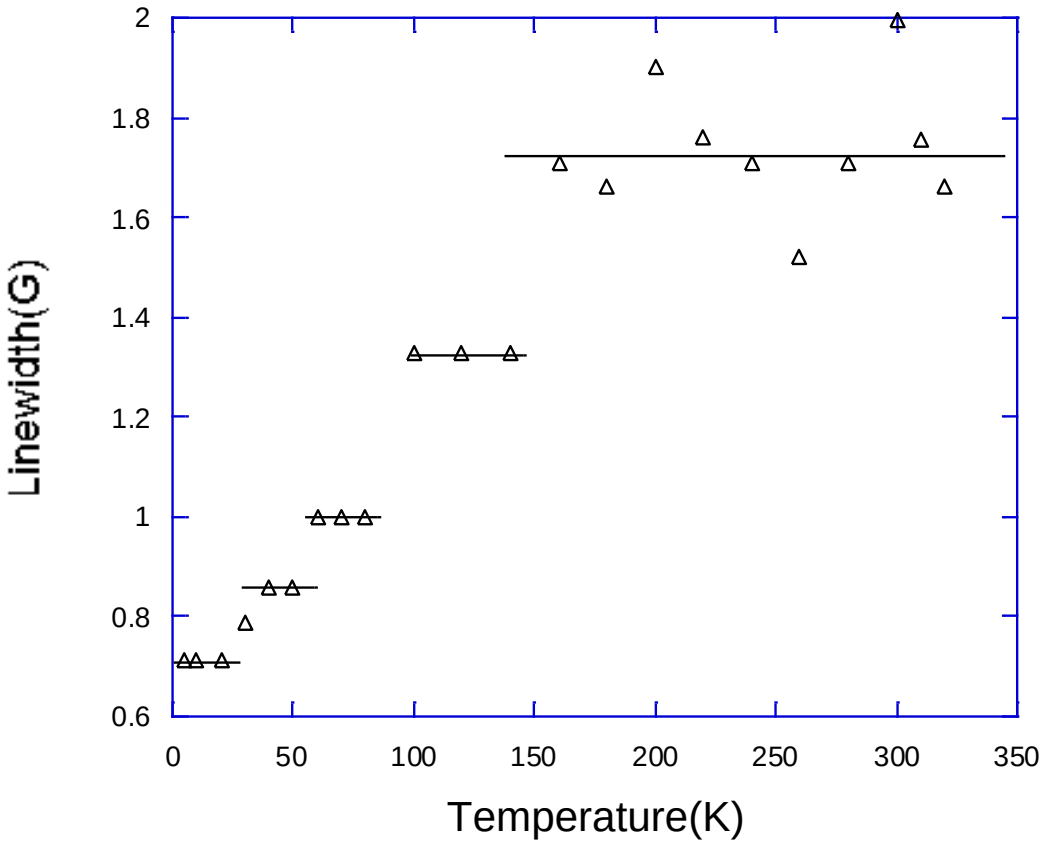

Figure 5.2.3.1 Temperature dependence of resonance linewidth of NK9. Changes include discrete distribution of linewidth (shown as plateaus or horizontal lines). Spin-lattice relaxation is considered to be governed by ordinary scattering (Elliot mechanism) at low temperatures, below about 140 K. The linewidth changes almost periodically about the horizontally drawn line at high temperatures.

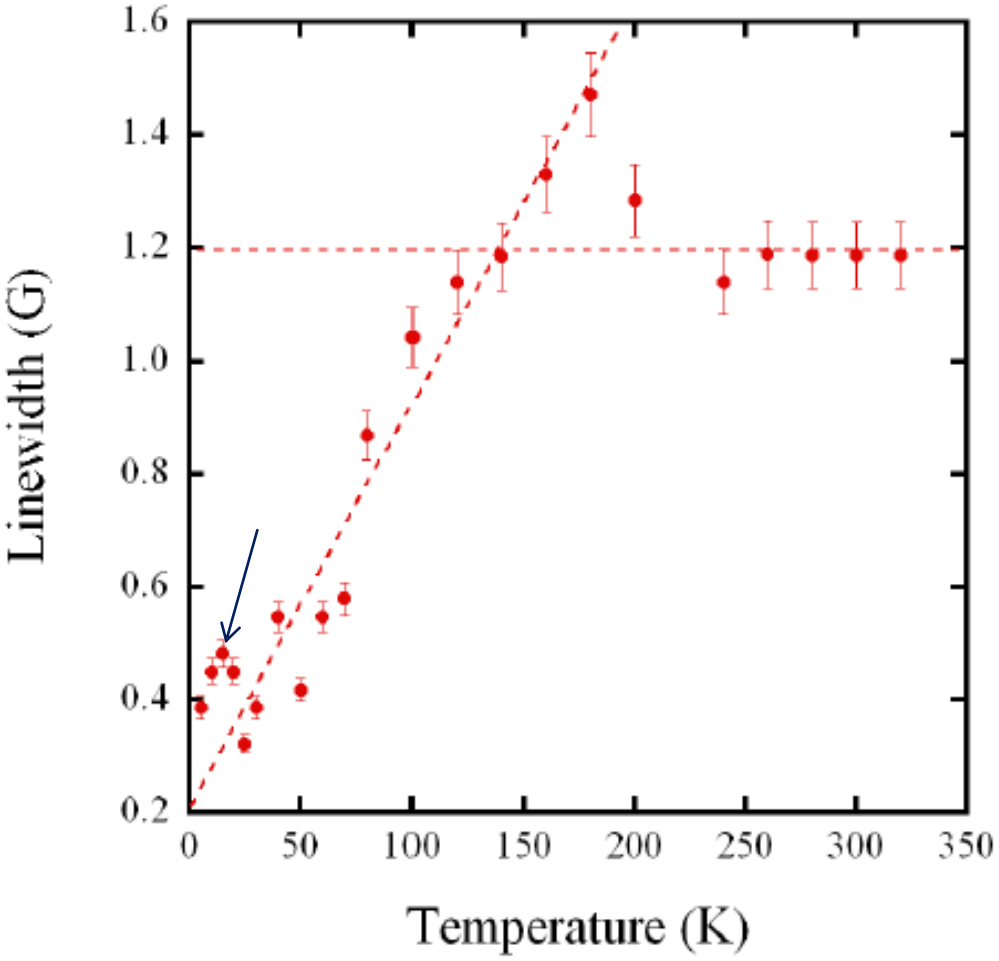

Figure 5.2.3.2 Temperature dependence of resonance linewidth of NK7. The arrow at low temperature hints the presence of anomaly centered about 15 K. A linear fit is just a guide to an eye, however the changes of linewidth above 30 K is in accordance with Korringa-like relaxation of paramagnetic centers. The hinted anomaly could be associated with spin relaxation mechanisms governed by phonons below about 25 K.

5.3 DISCUSSION

SPIN- LATTICE RELAXATION

The spin dependent electron-phonon scattering may result in the dissipation of magnetic energy by spins into a lattice through different relaxation paths mentioned above. In some ionic crystals or insulators containing paramagnetic ions (localized spins) the spin-lattice relaxation is governed by thermal modulation of the crystal field [21]. Ordinary scattering mechanism (Elliot mechanism) may also lead spin-lattice relaxation if conduction carrier system exists [16, 17]. In some materials and carbon nanomaterials containing the strongly interacting carrier spins and paramagnetic ions, the dissipation of energy into a lattice could be mediated by spin-orbit coupling [22, 23, 24].

I. *Spin-lattice relaxation via spin-orbit coupling*

The carbon nanospheres are mainly made from large network of the nanographite clusters shown in Figure 5.1.2.3; the magnetic properties of the carbon nanospheres should depend on the overall effect of these clusters whose individual magnetic moments differ with cluster. It is important to understand the influence of N paramagnetic ions (localized spins) in the magnetic properties carbon nanospheres; the efficient of N paramagnetic ions could be probe through following the nature of their interaction with conduction carriers.

Bottleneck effect

Our hypothesis that the properties of ESR signal is large determined by carrier electrons is fulfilled by assuming a strong exchange interaction between carrier and localized spins (spins responsible for quasi-localized and localized spins ESR signal with $g = 2$). This strong exchange interaction was shown to cause a shift in resonance field of localized spins due to the effective hyperfine field set-up by conduction electrons. This may explain large deviation or g-shift of samples from g-factor of reference sample (DPPH) in Table 5.1.1.1.

The coupling of localized spins is considered to be controlled by the exchange interaction between nitrogen paramagnetic ions and conducting carrier spins. Hence, individual nanographite cluster containing a number of nitrogen paramagnetic ions could be considered as magnetic if the exchange spins with conducting carriers result in magnetic ordering of localized spins. The spin-orbit coupling opens a path of spin-lattice relaxation as localized and carrier spins strongly interact. This is analogous to traditional s-d exchange as in iron or CuMn as shown in Figure 3.5.1.

Each nanographite cluster could be considered to consist of localized spins denoted by *d* and carrier spins denoted by *s* as shown in Figure 3.5.1. The relaxation rate is often expressed in term of resonant linewidth as follows:

$$\gamma\Delta B \cong \frac{1}{T_{eff}} = \{3\rho(E_F)k_BT\}/\{2S(S+1)C.T_{1s}\}, \qquad (3.5.1)$$

where $\rho\ (E_F)$, C, T_{1s} and S=1/2 is the spin density at the Fermi level, the localized spins concentration, the spin-lattice relaxation of carrier spins and intrinsic spin, respectively.

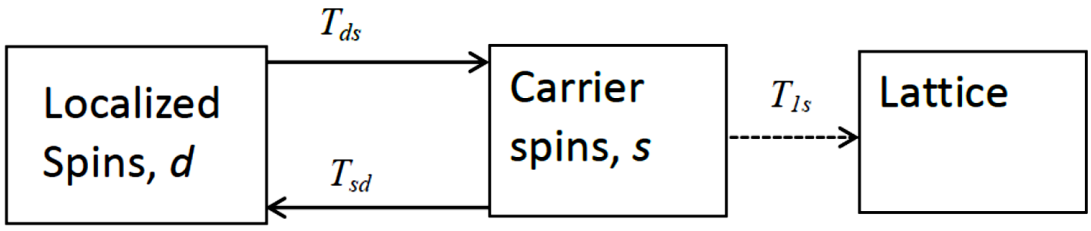

Figure 3.5.1 A schematic showings *s*-*d* exchange; electrons in *d*-states and *s*-states are localized and carriers (conducting electrons), respectively.

The linear temperature dependence of spin relaxation time and therefore linewidth is given by Korringa-like relaxation mechanism. The Korringa effect was original seen in NMR analysis where a nucleus with non-zero magnetic moment interacts with surrounding carrier electrons, Knight shift. In this case, the Korringa relaxation

occurs when localized spins relax to carrier spins, which in turn dissipate magnetic energies to a lattice through spin-orbit coupling T_{1s}.

Paramagnetic-ion spin relaxation via lattice vibrations

The narrow or Lorentzian ESR spectra measured at low temperatures in both samples reject any spin-spin relaxation mechanism; hence the spin-lattice relaxation mechanisms could dominate at low temperatures. The paramagnetic ions that are relaxing via lattice vibrations have been proposed and discussed under the Boltzmann prediction model [2]. For temperatures well below the Debye temperature there are generally three contributions - the direct process, the Raman process and the Orbach process respectively. The relaxation of a paramagnetic ion may be written in the form:

$$1/T_1 = T/A_D + T^7/A_R + 1/\{A_O[\exp(\Delta/k_BT) - 1]\}\,, \qquad (5.2.1.3)$$

where A_D, A_R, A_O and Δ are determined from fits to the experimental data. Since carbon nanospheres are graphitic in structure, one can always refer to electron-phonon scattering in graphite and nanographite as a basis when investigating the spin-lattice relaxation of these materials. Under the proposed model based on a network of nanographites (described in section I), the Curie- like changes in the amplitude of both samples at low temperatures could be mainly governed by paramagnetic electrons confined in clusters due to random potential fluctuations [25, 26]. Therefore, one has to discriminate between the paramagnetic electrons under cluster confinement from those bound to impurity atoms such as nitrogen. Nitrogen paramagnetic ions would be referred to as localized spins, while electrons confined in clusters are referred to as quasi-localized spins since they are thermally modulated.

Graphite has two types of phonon modes contributing in electron-phonon scattering; longitudinal acoustic in-plane and out-of-plane modes. The energy of the in-plane mode (Debye temperature ~ 2480 K) is about an order of magnitude larger than out-

of-plane mode (Debye temperature ~ 180 K); since the former is related to strong σ-bonds between planar carbons while the latter is related to weak van der Waals forces between the planes.

Phonon dynamics have been shown on nanographite particles; a carrier confined in a cluster is scattered by local phonons induced by a peripheral carbon paramagnetic ions [27, 28, 29]. The corresponding spin-lattice relaxation time associated with the interaction is

$$\frac{1}{T_1} \approx \frac{2t_d}{\pi}\left(\frac{|H_{so}|}{\hbar}\right)^2, \qquad (5.1)$$

where t_d is the scattering time between carriers in localized band and local phonons and H_{so} is the Hamiltonian for the spin-orbit coupling of the paramagnetic ion. The spin-lattice relaxation time estimated with equation (5.1) was about 10^{-8} s for carbon paramagnetic ion and spin-orbit coupling of carbon $\lambda \approx 14\ \mathrm{cm}^{-1}$[30].

Resonance Amplitude

The changes in normalized amplitude ΔM of both CNS with temperature are the same; they are Curie-like at low temperature and non-Curie at high temperature, hence this can be thought as some sort of electrical or magnetic transition.

The amplitude normalization was done through dividing the peak-to-peak amplitude at any temperature *T* with peak-to-peak amplitude at 80 K. The Curie type behaviour at low temperature may include nitrogen-induced paramagnetic electrons and electrons at zigzag edges of some clusters. The non-bonding π- electrons localized in clusters by structural disorder can only conduct via Coulomb gap variable range hopping (CVRH) in the localized band sitting around the Fermi level. Monte Carlo simulations showed that, thermal excitations could enhance electrical conductivity by successfully filling-up the Coulomb gap, and therefore a reduction of a potential barrier [31, 32, 33]. Charge transport at elevated temperatures could then result from

carriers hopping in at least conduction band tails states and/or extended states [34]; thus carriers are delocalized over a network of nanographite clusters. The thermal enhanced electrical conductivity of NK9 is complemented by pronounced Dysonian lineshape spectrum, larger asymmetry ratio and amplitude at high temperatures. Hence, the carbon nanospheres behave like insulators; paramagnetic electrons populate the localized band and conduction band at low and high temperatures, respectively. Since N paramagnetic ions concentration is assumed constant at all temperature, the thermal activated population of paramagnetic electrons could be attributed to the existence of non-bonding π-electrons at zigzag edges of nanographite clusters whose paramagnetism changes with temperature, i.e. Curie-type and enhanced Pauli-type at low and high temperature, respectively. The non-bonding π-electrons are said to be quasi-localized.

The experimental fit at high temperatures, relation (5.2.1.3), is mathematically analogous to relation describing the spin-lattice relaxation governed by phonons dynamics, Orbach process. However, the extrinsic defects such as cluster boundaries and poor packing of curved nanographite sheets in carbon nanospheres may soften phonon modes [35]. Hence, heating might preferable enhance electron-temperature rather than lattice-temperature [36]. The fit is somehow analogous to spin susceptibility fit observed at high temperature for carbon nanohorns; it was also attributed to thermal activation of carrier electrons [37]. Hence, the fit labelled as Orbach in the plot of amplitude of NK9 and NK7 undoubtedly results from thermal activation of carrier electrons from a nonmagnetic ground state to an excited state at energy 0.3 eV from ground state.

The larger amplitude measured from the resonance spectrum of NK9 suggests a significant contribution of additional paramagnetic electrons such as intrinsic and perhaps extrinsic electrons in spin and charge transport. The magnetic properties of the carbon nanospheres are determined by an overall effect of the clusters forming walls of the CNS. The Curie behaviour presented as Boltzmann factor at low temperatures (below about 25 K and 120 K for NK7 and NK9, respectively) could be

associated with localized paramagnetic electrons (quasi-localized π- electrons spins and N paramagnetic ions). Since quasi-localized spins are highly unstable; they can have Curie-type and enhanced Pauli-type paramagnetism at low and high temperatures, respectively. Therefore quasi-localized spins can be thermally excited and in this way allowing percolative path between nanographite network at high temperatures. At some instances, depending on the geometry and size of a material, the thermal excited paramagnetic electrons might undergo a circular motion resulting in orbital diamagnetism. At some intermediate temperatures there might exist a strong exchange between localized spins and conduction carrier spins as would be described by linewidth in details. Consequently, ferromagnetically coupling between localized paramagnetic electrons would be mediated by conduction electron spins. Hence, the carbon nanospheres could be thought to have undergone a magnetic transition from paramagnetic state to some spontaneous magnetism.

Direct measurement of the spin-lattice relaxation times using pulsed ESR may be useful in discriminating between the possible relaxation mechanisms. Moreover, the static magnetic susceptibility would also complement these measurements; it would elucidate magnetic transition and ordering.

Asymmetry ratio

Asymmetry ratio could explicitly discriminate between the electronic states governing the charge and spin transport in different ranges of temperature; asymmetry ratio between 3 and 9 are mainly associated with conducting materials, while asymmetry ratio around 1 describe an insulator. Hence, the asymmetry ratio could compare the concentration of electrons in localized and conduction band (carriers) as a function of thermal activation. The Dyson's theory shows that changes in the A/B parameter (asymmetry ratio) of the ESR line of the conducting sample is a consequence of changes in the ratio of T_D and T_2 relaxation times. This change is expected due to increase of spin–lattice relaxation time T_1 at low temperatures,

whereas T_D is set by the lattice scattering and can be considered as the characteristic parameter of the material [3, 4].

The thermal enhance asymmetry ratio (A/B) of NK9 in Figure 5.2.3.1 also confirm that large carriers dominate at high temperatures; the ratio of NK9 approaches a value of 2.3 around 320 K. The rising asymmetry ratio confirms that there is a growing population of paramagnetic electrons at temperatures above 250 K. This would also enhances the electrical conductivity, since the conductivity can be related to thermally reduced electrical resistivity ρ provided by Coulomb gap, and therefore shorten diffusion time

$$T_D = 3/4\pi f \sigma v_F \Lambda, \tag{5.2}$$

where $\rho = 1/\sigma$ and other quantities are well described in (5.1.3.5). The asymmetry ratios centered about 1.4 was observed for NK9 at low temperatures (below about 120 K); the resonance spectrum and therefore charge transport is therefore governed by electrons hopping in localized bands at low temperatures.

The A/B ratio of NK7 does not obviously increases with temperature (shown in Figure 5.2.3.2); it slowly increases with temperature in an unpredictable manner. Furthermore, the A/B ratios in NK7 were all below a value of 1.4 confirming a charge and spin transport mainly governed by the paramagnetic electrons in localized region. The random variation of the asymmetry ratio can be thought to come from N paramagnetic ions in different chemical environments and whose interaction with carriers result in exchange spin interactions of different strengths. One can therefore conclude that NK7 contain large amount of localized spins and few carrier spins that are interacting strongly, in such a way that their resonance spectra are overlapping strongly to give the observed single ESR spectrum [38]. Consequently, the strong coupling between paramagnetic ions could result in spontaneous magnetization mediated by carrier spins. In addition, the reduction of localized spins concentrations through thermal activation in favour of carriers was also confirmed by a weak approach to Dysonian lineshape of NK7 spectrum.

Linewidth and relaxation mechanisms

Resonance linewidth is proportional to electron spin-spin (spin dephasing) relaxation times T_2 or spin-lattice relaxation times T_1, when an interaction is conserving or dissipating energy, respectively. Generally, spin-lattice relaxation time is long at low temperatures due to low phonon density, hence relaxations is mainly governed by spin-spin interactions T_2. The effective spin relaxation time and therefore linewidth of strongly interacting localized and carrier spins in nanographite clusters can be expressed as follows,

$$\Delta B \cong 1/T_{eff} = 1/T_{ds}(T_{sd}/T_{s1}), \tag{5.3}$$

where T_{ds}, T_{sd} and T_{s1} is the relaxation of localized spins to carrier spins, the relaxation of carrier spins to localized spins and spin-lattice relaxation time of carrier electrons, respectively. The temperature dependence of resonance linewidth is governed by Korringa relation,

$$\Delta B \cong 1/T_{eff} \sim 1/T_{ds} \sim T \tag{5.4}$$

since T_{sd} is independent of temperature and T_{1s} is weakly dependent on temperature, and T_{1s} is governed by boundary scattering in graphitic clusters [14].

Indeed, NK7 has the linewidth which is changing linearly with temperature in the range 30-180 K; hence strong interaction between localized and carrier spins is in accordance with Korringa relation [see relation (3.5.3) above]. Slight deviation around the linearly increasing linewidth could be attributed to different paramagnetic centers (edge-inherited and nitrogen induced paramagnetic ions) interacting with carrier spins. Hence, the interaction of different localized spins with conducting carrier spins (Korringa relation) might be of different strengths.

As temperature rises above 180 K the linewidth is narrowed by (T_{sd}/T_{1s}) due to the rapid increase of thermal excited states; hence rapid rising in the population of Pauli-type paramagnetic electron spins which would be gradually burying any localized

spins effects. Hence, at bottleneck the spin relaxing rate $1/T_{1s}$ decreases with temperature since large carrier spins are no longer being triggered by localized spins to relax to the lattice. So above 180 K, the narrowing of linewidth could be associated with either exchange interaction of rather identical paramagnetic electrons which are considered weakly delocalized. The weak delocalization of these thermally excited paramagnetic electrons is confirmed by measurement of low asymmetric ratio whose magnitude is below 1.4 for NK7. Comparison of magnetic susceptibilities which could be either Curie –type or Pauli –type depending on whether the properties of ESR spectrum is determined by localized or delocalized paramagnetic electrons, respectively[6, 7].

This argument further answers the occurrence of temperature independent linewidth (1.2 G) above 240 K; the effect of localized spins is almost completely obscured, while conducting electrons might be experiencing an ordinary scattering mechanism, Elliot type mechanism [16, 17]. The spin-lattice relaxation time and the corresponding linewidth ΔB defined by ordinary scattering mechanism contain contribution from scattering of conduction carrier with defects and phonons as follows,

$$\Delta B \approx \frac{\hbar}{2\sqrt{3}g\mu_B T_{1s}}, \tag{5.5}$$

$$\frac{1}{T_{1s}} \approx \alpha(\Delta g)^2 \left(\frac{1}{\tau_b} + \frac{1}{\tau_p}\right), \tag{5.6}$$

where α is a numerical factor whose magnitude is of the order of 1, Δg is the deviation from free- electron g-factor value (2.0023). Scattering time τ_b and τ_p defines scattering of conduction electrons by defects (boundaries and impurity atoms) and phonons, respectively. The constant linewidth above 240 K hints a negligible contribution of phonons to the spin-lattice relaxation. Hence, the constant linewidth of NK7 at high temperature could be at least governed by boundary scattering in nanographite clusters and is weakly dependent on temperature [14]. The change of linewidth below about 25 K is not quite clear; it hints a peak centered about 15 K as

shown by an arrow in Figure 5.2.4.2. Electrical transport and magnetic susceptibility measurements could be invoke to support this conjecture.

At low temperatures the resonance linewidth of NK9 increases with temperature in steps, hence discrete values of linewidth corresponding to different ranges of temperature (as shown in Figure 5.2.4.1). This pattern could be hardly associated with dipolar interactions between localized spins, since paramagnetic ions or localized spins are weakly interacting particles. Boundaries between nanographites network results in carriers being confined within clusters or bound in nitrogen atoms at low temperatures. Hence, at low temperatures the carrier electrons can be thought being conducting within individual clusters, and therefore are subjected to ordinary scattering mechanism defined by relation (5.5) and (5.6) above. Therefore, carriers are probably scattered by defects associated with clusters (boundaries and nitrogen atom) and phonons at low temperatures.

The electron-phonon scattering event is in-elastic, hence it can induce spin transition. The broadening of linewidth is delayed in temperature as it form plateaus within different ranges of temperature. The elastic scattering described by plateaus is considered to dominate when phonon energies are not comparable to energy between spin levels. Since poor packing of nanographite sheets along the c-axis result in elongated inter-planar spacing, this could probably results in softening of out-of-plane acoustic phonon mode [35]. The fewer layers of nanographites (3-6) can result in phonon energy spectrum with discrete energy levels [14, 35]. Hence, the nature of phonon interaction which triggers the spin transition of confined carriers could be associated with the low-energy out-of-plane mode. The observed plateaus in linewidth could have broad distribution of g-values due to changes of electronic energy distribution associated with changing temperature [36]. This strange change in linewidth could be further investigated with different spectrometer settings.

The observed narrow linewidth of about 0.7 G and far below 0.4 G for NK9 and NK7 strongly reject any spin-spin relaxation mechanism at low temperatures. Taking into

account the power saturation of amplitude for NK7 and NK9; NK9 suggests a shorter T_1 and therefore NK9 and NK7 could be described by different spin-lattice relaxation mechanisms mentioned above. Indeed, the linewidth of both samples are very different in the whole range of temperature investigated. At temperatures higher than about 140 K most of electrons are weakly delocalized over nanographites network as confirmed by rising values of asymmetry ratio and ESR amplitude above. Since the spin-lattice T_{1s} of carriers is weakly dependent on temperature when bottleneck effect is assumed [14], hence the thermal changes observed in linewidth of NK9 could be closely associated with thermally modulated dipolar and exchange interaction between large conducting carriers. Under bottleneck assumption, the effect of localized spins is highly suppressed at high temperatures as more electrons are thermal activated into extended states or at least conduction band tails. Therefore, the dipolar or exchange interaction could be associated with conduction carrier spins, and this is in accordance with Dysonian lineshape of NK9 observed at room temperature. The temperature range which have a potential to give the strong coupling between localized spins should be observed from resonance spectrum of strongly interacting carrier and localized spins giving rise to single asymmetric Lorentzian lineshape[38]. This intermediate temperature could exist in a range of temperature where the resonance amplitude is almost flat between Curie (Boltzmann factor) and thermal activated amplitude (Orbach-like changes). This amplitude was denoted by parameter *A* in the fitting expression deduced from Boltzmann factor prediction [2], and NK9 has parameter *A* that almost doubles that of NK7 as shown in Table 5.2.1.1. If one assumes that most confined carriers are dominant around 80 K, the fraction of conducting carriers that could be interacting with fixed N paramagnetic ions could be deduced from Table 5.2.1.1, and is about 34 % and 67 % for NK7 and NK9, respectively. The lower percentage of conduction carriers (estimated in sample labelled NK7) in comparison to localized spins suggests strong coupling of paramagnetic ions at intermediate temperatures [38]. At high temperatures the spin relaxation of NK9 is governed by conducting carriers, manifested by the observed Dysonian lineshape and thermally enhanced asymmetry ratio.

The resonance linewidth of NK9 varies almost periodically with temperature in the range of about 140- 240 K and 240- 320 K, respectively. The carrier-carrier spin interaction, however does not change the total magnetic moment, and in that sense it does not change the spin-lattice relaxation time T_{1s} but rather causes spin decoherence (changes transverse relaxation time T_2). Hence, the observed changes in linewidth could not be associated with lattice vibrations. This almost periodically variations of linewidth are credited to interactions of non-identical carrier spins precessing about different axes distance θ_i apart [39].

References

1. Keartland J. M., Dubazane M. B., Marsicano V., Kunjuzwa N. and Coville N. J., Characterization of nitrogen-doped carbon nanospheres using electron magnetic resonance, *Proceedings of the SA Institute of Physics 2011,127-133. Pretoria July 2011, ISBN: 978-1-86888-688-3.*

2. Dubazane M. B., Keartland J. M., Mishgina Y., Magnetic properties of carbon nanospheres at low temperatures, *Proceedings of the SA Institute of Physics 2011,168-173.Pretoria July 2011, ISBN: 978-1-86888-688-3.*

3. Dyson F., *Phys. Rev.* **98**, 2 (1955).

4. Feher G. and Kip A. F., *Phys. Rev.* **98**, 2 (1955).

5. Joseph Joly V. L., Takahara K., Takai K., Sugihara K. and Enoki T., *Phys. Rev. B* **81**, 115408 (2010).

6. Osipov V.Yu., Enoki T., Takai K., Takahara K., Endo M., Hayashi T., Hishiyama Y., Kaburagi Y., Vul' A.Ya., Carbon **44**, 1225 (2006).

7. Pifer J.H. and Longo R.T., Phys. Rev. B **4**, 3797 (1971).

8. Winter J., Magnetic resonance in metals, Clarendon Press, Oxford, 1971, Chapter 10.

9. Yoshizawa K., Okahara K., Sato T., Tanaka K. and Yamabe T., *Carbon* **32**, 1517 (1994).

10. Fujita M., Wakabayashi K., Nakada K. and Kusakabe K., *J. Phys. Soc. Jpn.* **65**, 1920 (1996).

11. Fujita M., Igami M. and Nakada K., *J. Phys. Soc. Jpn.* **66**, 1864 (1997).

12. Robertson J., *Prog. Solid St. Chem.* **21**, 199 (1991).

13. Castner T. G., *Phys. Rev* **115**, 1506 (1959).

14. Andersson O. E., Prasad B. L. V., Sato H. *et al., Phys. Rev. B***58**, 16387 (1998).

15. Pines D. and Slichter C. P., *Phys. Rev.* **100**, 1014 (1955).

16. Elliot R. J., *Phys. Rev.* **96**, 2 (1954).

17. Kubo R., *Phys. Soc. Jpn.*, **17**, 975 (1962)**.**

18. Huertas-Hernando D., Guinea F., and Brataas A., *Phys. Rev.* B **74**, 155426 (2006).

19. Korringa J., *Physica*, **16**, 601 (1950).

20. Kotosonov A. S., *JETP Lett*. **43**, 37 (1986).

21. Orbach R., *Proc. Roy. Soc. London Ser. A* **264** 485, 1961.

22. Hasegawa, H., *Prog. Theor. Phys*. (Kyoto) **21**, 483 (1959).

23. Owen J., Browne M., Knight W. D. and Kittel C., *Phys. Rev.***102**, 1501(1956).

24. Taylor R. H., *Adv. Phys.* **24**, 681(1975).

25. Joseph Joly V. L., Takahara K., Takai K., Sugihara K. and Enoki T., *Phys. Rev. B* **81**, 115408 (2010).

26. Romanenko A. I., Anikeeva O. B, Okotrub A. V., *et al*., *Physics of the Solid State* **44**, 3 (2002).

27. Wallis F., *Phys. Rev.* **116**, 302 (1959).

28. Igami M., *Master's thesis*, University of Tsukuba, 1998.

29. Igami M., Fujita M. and Mizuno S., *Appl. Surf. Sci.* **130**, 870 (1998).

30. Muller K. A. and Kleiner R., *Phys. Lett.* **1**, 98 (1962).

31. Sarvestani M., Schreiber M., and Vojta T., *Phys. Rev. B***52**, R3820 (1995).

32. Grannan E. R. and Yu C. C., *Phys. Rev. Lett*. **71**, 3335(1993).

33. Shlimak I., Kaveh M., Ussyshkin R., *et al., Hopping and Related Phenomena,* edited by Millo O. and Ovadyahu Z., (Racah Institute of Physics, The Hebrew University of Jerusalem, Israel, 1995), *Phys. Rev. Lett.* **75**, 4764 (1995).

34. Fahim N. F., Kojima N., Yamaguchi M., *et al*., *J. Appl. Phys.* **93**, 5 (2003).

35. Nagayoshi H., *Phd. Thesis*, University of Tokyo, 1975.

36. Chen Z., Carter S. G., Bratschitschi R., Dawson P. and Cundiff S. T., *Nature Physics* **3**, 265 (2007).

37. Garaj S., Thien-Nga L., Gaal R., *et al., Phys. Rev B* **62**, 24 (2000).

38. Yang X. -M., He Z. -T, Li W. -F. *et al*., *Journal of Applied Physics* **109**, 083933 (2011).

Pryce M. H. L. and Stevens K. W. H., *Proc. Phys. Soc.* A**63**, 36 (1950).

CHAPTER 6

CONCLUSION

The carbon nanospheres prepared from vertical and horizontal reactors have different microstructural features as demonstrated by Raman and X-ray diffraction spectroscopy. The electron spin resonance (ESR) measurements have been used to qualitative investigate the electronic charge and spin transport in the range of temperature. Very broad signal was beyond detection in most samples produced the vertical reactor; the signal is assigned to carrier spins and therefore conduction electron spin resonance (CESR) spectrum form a background signal of most localized paramagnetic electrons. This broad spectrum was attributed to the low sensitivity of carrier spins due to larger spin-orbit coupling which could have enhanced by a network of highly curved nanographite sheets. The variation of ESR amplitude with temperature was initially described using a lattice vibration model; an obvious relationship exists between the spin-lattice relaxation time and resonant amplitude. However, the increase of the amplitude above 250 K is most likely due to spin-carrier interaction. Hence, heating may preferential increase carrier electron-temperature rather than lattice-temperature. Consequently, the paramagnetic ions relax via interaction with thermal activated carrier electrons, which is supported by changes in the resonance linewidth.

Large population of thermal excited paramagnetic electrons was further evidenced by thermal enhanced asymmetry ratio and large resonance amplitude at high temperatures. The larger asymmetry ratio was around 2.3 and 1.4 for NK9 and NK7, respectively. The lower ratio measured in sample NK7 could suggest larger population of localized paramagnetic electrons at zigzag edges than in sample labeled NK9. Hence, NK7 has smaller nanographite cluster than NK9 and therefore larger optical band gap. Therefore, the changes of resonance parameters (such as amplitude, asymmetry ratio, and linewidth) with temperature would be largely described by behavior of quasi-localized spins in the range of temperature.

The behavior of quasi-localized spins changes with temperature; they have Curie-type and Pauli-type paramagnetism at low and high temperatures, respectively. Hence, the quasi-localized spins have a tendency of opening a percolative path of carriers at high temperatures. The stronger Curie-type paramagnetism (as described by Boltzmann model) of sample NK7 demonstrated by resonance amplitude (below about 25 K) also include traces of N paramagnetic ions.

Single ESR signals of carbon nanospheres produced from horizontal reactor were asymmetric and Dysonian; they suggest the presence of strong exchange interaction between conducting carriers and localized paramagnetic electrons. However, the coupling of localized spins seemed likely when mediated by lower concentration of conducting carrier spins.

The linewidth of NK7 suggested spin-spin interactions between localized paramagnetic spins over the temperature range 30-180 K. The thermal modulated concentration of conduction carriers (deduced from normalized resonant amplitude) necessary to enhance the coupling of localized spins is approximately 34 %; thus most electrons are in the localized states. In comparison, the sample labelled NK9, conduction carriers were approximately 67 % and the sample showed no sign of coupling between localized spins.

The temperature dependence of the asymmetry ratio confirms that conduction carrier concentration is thermally modulated and can weaken spin-spin interactions of paramagnetic ions. Indeed, NK7 was shown to contain lower fraction of localized spins as observed in the weaker Dysonian spectrum at high temperatures and lower asymmetry ratio. Thermal enhanced population of paramagnetic electrons was also manifested through narrowing of the resonant linewidth of NK7 in the range 180- 240 K. The narrowing could be attributed to thermally excited electrons which might be undergoing exchange interaction. The constant resonant linewidth above 240 K features ESR spectra originating from uncoupled electron spins delocalized over walls of carbon nanospheres.

Electrical transport and magnetic susceptibility measurements would be of great interest in these materials. Measurements of spin-lattice relaxation time over a wide range of temperature performed using an ESR spectrometer operating in a pulse mode would also of great interest.

APPENDIX A

THE SPECTROMETER

A.1 Instrumentation and operation

http://www.bruker-biospin.com/brukerepr/continuouswavepractice.html

The ESR spectrometer can be described using four main components, shown in Figure A1.

- Monochromatic microwave source or Gun
- Waveguide(WG)
- Microwave cavity
- Detector/Microwave Bridge

It is important to know the role of each of these components to fully understand how the ESR spectrometers work.

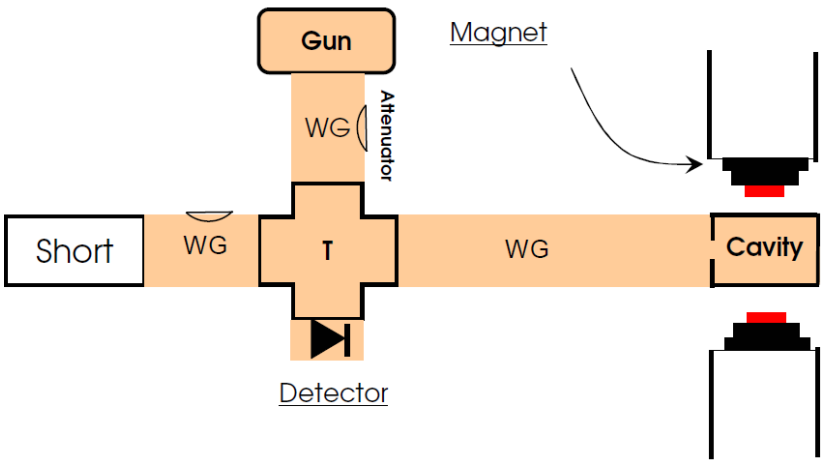

Figure A.1 Layout of typical reflective ESR spectrometer.

Microwave source and waveguide

A klystron is commonly used as microwave generator; the microwaves move across a cylindrical or rectangular pipe known as waveguide into a cavity, moveable short (reference arm), and detector as shown in Figure A.1.

Cavity

Microwave cavities amplify weak signals from samples. The microwave cavity is simply a metal box with a rectangular shape which resonates with microwaves much like an organ pipe resonates with sound waves. Resonance means that the cavity stores the microwave energy; at the resonance frequency there is no reflection of microwaves, but will remain inside the cavity.

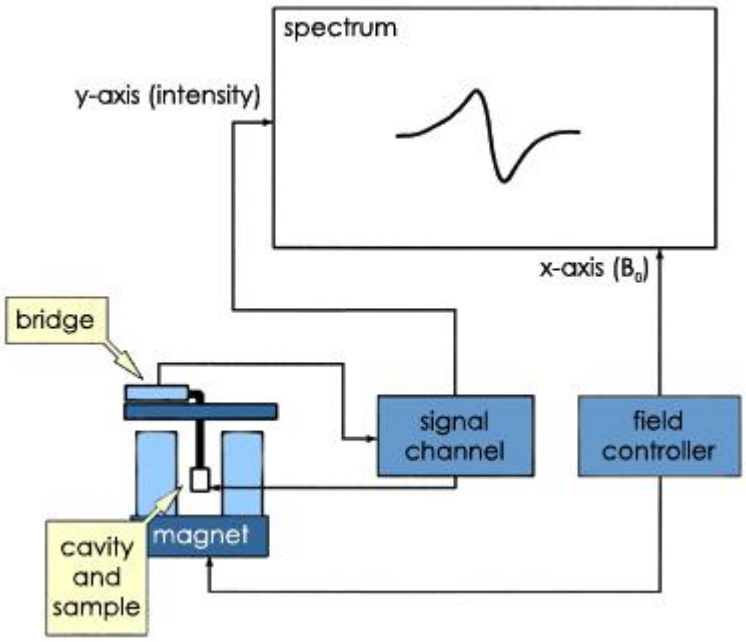

Figure A.2 Block diagram of the Bruker ESR spectrometer.

Cavities are characterized by their quality factor Q, which indicates how efficiently the cavity stores microwave energy. As Q increases, the sensitivity of the

spectrometer increases. The Q factor is given as

$$Q = 2\pi . \frac{\text{energy stored}}{\text{energy dissipated per cycle}} \qquad \text{(A.1.1)}$$

where the energy dissipated per cycle refer to the amount of energy lost during one microwave period.

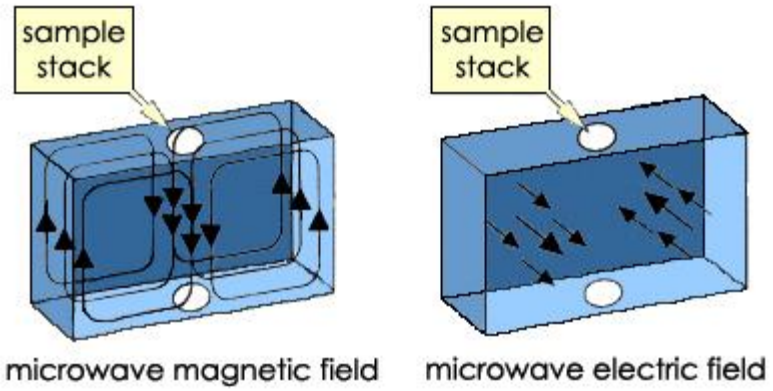

Figure A.3 Magnetic and electric field patterns in ESR cavity.

At resonance the standing waves are formed inside the microwave cavity. Standing electromagnetic waves have their electric and magnetic field components exactly out of phase, i.e. where the magnetic field is maximum, the electric field is minimum and vice versa. The spatial distribution of the amplitudes of the electric and magnetic fields in ESR cavities is shown in Figure A.3. Most samples have non-resonant absorption of the microwaves via the electric field and thus they reduce Q due to increase in the dissipated energy. It is the magnetic field that drives the resonance absorption, therefore if one place a sample in the electric field minimum and the magnetic field maximum, an enhanced ESR signal and highest sensitivity is achieved.

The microwaves are couple into the cavity via a hole called an iris. The iris has an adjustment screw which controls the amount of microwaves reflected back and/or entering the cavity. The iris accomplishes this by carefully matching or transforming the impedances of the cavity and the waveguide.

Detector and Microwave Bridge

The Schottky barrier diode detects the reflected microwaves and converts the microwave power into electrical current. At low microwave power levels, less than 1 mW, the diode current is proportional to the microwave power and the detector is called a square law detector. At higher power levels, (greater than 1 mW) the diode current is proportional to the square root of the microwave power and the detector is called a linear detector. The transition between the two regions is very gradual.

For quantitative signal intensity measurements and optimal sensitivity the diode should operate in linear region. The best results are attained with a detector current of approximately 200 mA. A reference arm (moveable short) ensures that the detector operates at that level; reference arm supplies the detector with some extra microwave power or bias. Some of the source power is tapped off into the reference arm, where a second attenuator controls the power level for optimal performance. There is also a phase shifter which ensures that the reference arm microwaves are in phase with the reflected signal microwaves when the two signals combine at the detector diode.

The detector diodes are very sensitive to damage from excessive microwave power and will slowly lose their sensitivity. There is therefore a protection circuitry in the bridge which protect by monitoring the current and thus the microwave power level. Hence any risk which might be associated with improper operating procedures or purely accident could be significantly minimize.

A.2 Signal acquisition

When a sample absorbs the microwave energy, the *Q* factor is lowered because of the increased losses and the coupling changes because an absorbing sample changes the impedance of the cavity. A cavity is therefore no longer critically coupled and microwaves will be reflected back to the bridge resulting in an ESR signal.

Detection scheme

When the static magnetic field is scanned through a region of resonance, unpaired electrons in a sample absorbed small part of incoming microwave field $\boldsymbol{H_1}$, and thus causing a change in resonance frequency of the microwave cavity. This is the direct detection scheme known as DC detection. Unfortunately the DC detection schemes are susceptible to signal distortions which are attributed to drift of the DC amplifier and *1/f* noise. To overcome these shortcomings, the Bruker ESR spectrometer incorporates magnetic field modulation as part of the detection scheme.

(a) Magnetic Field modulation

Electron spin resonance spectrometer uses field modulation as part of detection scheme. The static magnetic field $(\mathrm{H_0} + \mathrm{H_\delta})$ strength in the vicinity of a sample and is modulated with alternating field $\frac{1}{2}\mathrm{H_m}\sin\omega_\mathrm{m}\mathrm{t}$ at the modulation frequency ω_m. The "static" magnetic field is

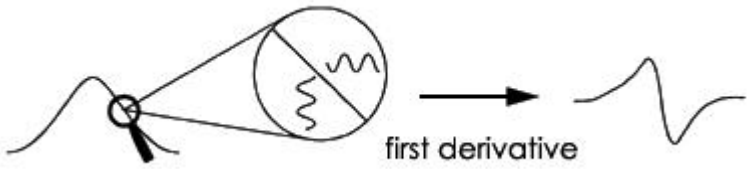

Figure A.4 Field modulation and phase sensitive detection.

slowly swept over the range ΔH_0 between $(H_0 - \frac{1}{2}\Delta H_0)$ to $(H_0 + \frac{1}{2}\Delta H_0)$ over the time t_0, where H_0 is the center field of scan. The instantaneous magnetic field strength at any time t is given by

$$H = H_0 + \Delta H_0\left(\frac{t}{t_0} - \frac{1}{2}\right) + \frac{1}{2}H_m sin\omega_m t \qquad \text{(A.2.1)}$$

where

$$H_\delta = \Delta H_0\left(\frac{t}{t_0} - \frac{1}{2}\right). \qquad \text{(A.2.2)}$$

If there is an ESR signal, the field modulation quickly sweeps through part of the signal and the microwaves reflected from the cavity are amplitude modulated at the same frequency ω_m. For an ESR signal (DC) which is approximately linear over an interval as wide as the modulation amplitude, the ESR signal is modulated into AC signal. The amplitude of modulated signal is proportional to the slope of the ESR signal (Figure A.4) and is fed into the input of the detector.

(b) Issues related to poor spectrometer setting

Applying more magnetic field modulation increases the intensity of an ESR signal; however, if the modulation amplitude is too large (larger than the line widths of the ESR signal), the detected ESR signal broadens and becomes distorted (as shown in Figure A.5). A good compromise between signal intensity and signal distortion occurs when the amplitude of the magnetic field modulation is equal to the width of the ESR signal. It is also useful to set the modulation amplitude greater than the splitting between two ESR signals; one can no longer resolve the two signals.

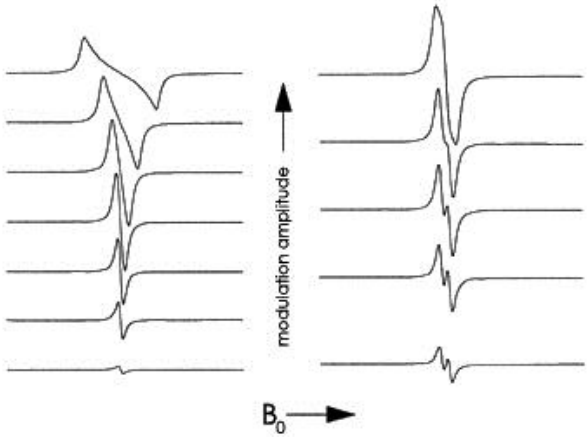

Figure A.5 Signal distortions due to excessive field modulation.

Time constants filter out noise by slowing down the response time of the spectrometer. As the time constant is increased, the noise levels drop. However choosing a time constant which is very long in comparison to the rate at which one scan the magnetic field can easily distort or filter out the very same signal one is

trying to recover from noisy environment (Figure A.6). As a rule of thumb, one has to make sure that the time needed to scan through a single ESR signal should be ten times greater than the length of the time constant.

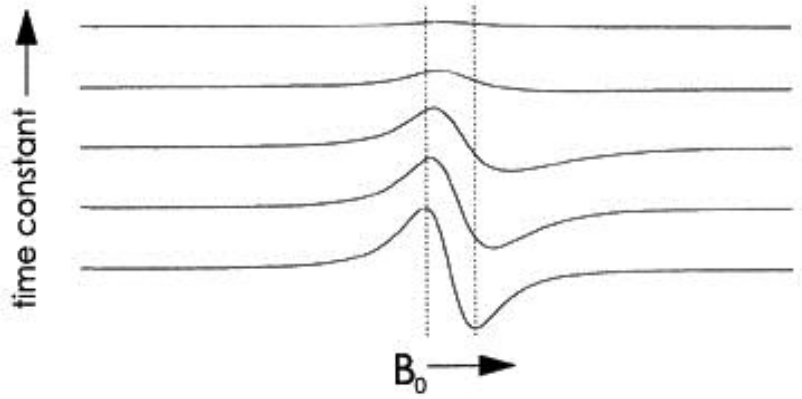

Figure A.6 Signal distortion and shift due to excessive time constants.

(c) Magnetic field controller and its operation

The magnetic field controller allows one to sweep the static magnetic field in a controlled and precise manner during resonance measurements (Figure A.7). The field controller consists of two parts; the first part sets the field values and time the field sweeps while the second part regulates the current in the windings of the magnet to successfully attain the requested magnetic field value.

The magnetic field values and the timing of the magnetic field sweep are controlled by a microprocessor in the controller. A field sweep is divided into a maximum of 4096 discrete steps called sweep addresses. At each step, a reference voltage corresponding to the magnetic field value is sent to the part of the controller that regulates the magnetic field. The sweep rate is controlled by varying the waiting time between the individual steps.

The magnetic field regulation occurs via the Hall probe placed between the magnets. It produces a voltage which is dependent on the magnetic field perpendicular to the

probe. The relationship is not linear and the voltage changes with temperature; however, this is easily compensated for by keeping the probe at a constant temperature slightly above room temperature and characterizing the nonlinearities so that the microprocessor in the controller can make the appropriate corrections.

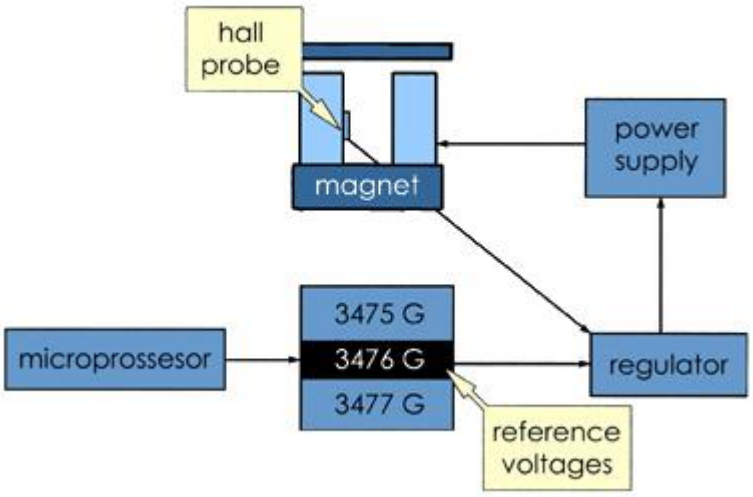

Figure A.7 A block diagram showing the field controller and associated components.

Regulation is accomplished by comparing the voltage from the Hall probe with the reference voltage given by the other part of the controller. When there is a difference between the two voltages, a correction voltage is sent to the magnet power supply which changes the amount of current flowing through the magnet windings and hence the magnetic field. Eventually the error in voltage drops to zero and the field is stable. This occurs at each discrete step of a magnetic field scan.